Gas Dynamics in the Galactic Center

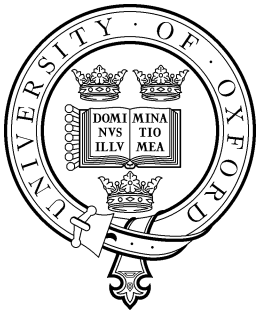

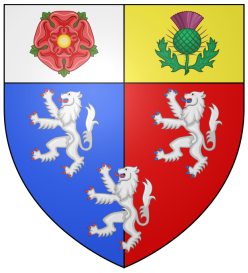

Matthew G. L. Ridley

Pembroke College

University of Oxford

A thesis submitted for the degree of

Doctor of Philosophy

Michaelmas 2018

Abstract

In this thesis we examine several aspects of the dynamics of the interstellar medium at the centre of the Milky Way. The gas is an excellent dynamical tracer: models of the gas response to an externally imposed barred potential place unique constraints on the Galaxy's matter distribution.

We show how a simple two-dimensional model of gas flow in a rigidly rotating barred potential provides a convincing explanation of many of the features observed in the (l, b, v) distribution of molecular emission lines at Galactic longitudes $|l| < 5°$, within the so-called "central molecular zone" (CMZ). In particular, we show that the central gas disc develops a two-armed spiral, which, in projection, naturally explains two of the dominant elongated emission features. We compare our model against competing explanations for these features in the CMZ and make predictions for future observations.

We investigate the general behaviour of gas flow in realistic self-consistent barred N-body models and find that, in contrast to previous work, the potential is sufficiently smooth and regular that the gas quickly settles into an equilibrium configuration. We show that simple rigid-potential models can be constructed that give good qualitative matches to the gas flow in the live, self-consistent potential. We provide guidance on how best to apply methods that attempt to constrain the Galaxy's potential by fitting features in the (l, v) distribution semi-automatically.

Finally we discuss the vertical dynamics of the central gas disc in our simulations. We find that the central gas disc in our models almost exactly follows ballistic orbits. If tilted out of the plane of the galaxy the normal vector to the gas precesses in the opposite sense to the circulation of the gas as a simple consequence of epicyclic theory. Our simulations do not reproduce the observed magnitude of the tilt of the CMZ, suggesting that something other than gravitational forces are responsible for tilting the gas out of the Galactic plane.

Acknowledgements

I would firstly like to thank my supervisor Dr. John Magorrian. During this DPhil I have had the privilege of being supervised by one of the most eminent dynamicists in the field of astrophysics. Over the last three years he has been an invaluable advisor and mentor. I am in awe of his programming ability and fundamental grasp of physics. His guidance has been central to all of the work in this thesis.

Secondly I would like to thank Dr. Mattia Sormani, who has been like a second supervisor to me during this degree. Much of this work has built on his ideas, and his advice and support during my time in astrophysics has been indispensable.

As a part the Galactic Dynamics group I have come to know some amazing people, including Payel Das, Ralph Schönrich, James Binney, Eugene Vasiliev, David Cole and Michael Aumer. I have enjoyed many stimulating discussions and conversations with all of them, and I am lucky to have been part of such a vibrant and strong research group.

I thank the STFC and ERC for providing the funding for me to undertake this DPhil.

Outside of physics, the last three years has been hugely enriched by my friends and housemates, Valentin Sulzer, Matt Kerin, James Saraidaridis, Eddie Rolls and Rowan Arthur. The friendships I have built here have been a source of innumerable good times, constant humour and good natured competition, and I know they will last for the rest of my life.

Endurance sport is a big part of my life, and I thank the many members of OUCC and OUTriC for providing a highly motivating and competitive environment for me to develop as an athlete during my studies.

I would like to thank my family, both close and extended, for providing unwavering love and support at all times. A special thanks goes to my siblings, Ben, Amy and Emily, and my stepmother Nicky, for the laughter and happiness they bring to my life.

I dearly thank my father David, who I wish was here to share this moment with me. For his unconditional love, lessons and advice during my childhood I will always be indebted to him. I thank my mother Sue for making me everything that I am today, and for the many sacrifices she has made to give me the best possible start in life.

Finally, I thank Fennel, for making me the happiest I have ever been, and for her never-ending love, support, affection and friendship over the last five years. She is my best friend and the cornerstone of my life, and none of this would have been possible without her.

Declaration

The work in this thesis is based on research I carried out at the University of Oxford between Michaelmas Term 2015 and Michaelmas Term 2018.

Matthew Ridley

First-author Peer Reviewed Publications

1. Ridley, M. G. L., Sormani, M. C., Tress, R. G., Magorrian, J. & Klessen, R. S., 2017. Nuclear spirals in the inner Milky Way. *MNRAS*, **469**, 2251–2262

Chapter 3 is adapted from this work. I performed the simulations and analysis presented in the paper, and wrote the majority of the text. Dr. Mattia Sormani contributed heavily to the original direction and style of the paper. The other coauthors provided additional feedback and suggested relevant literature.

Other Publications

2. Sormani, M. C., Tress, R. G., Ridley, M., Glover, S. C. O., Klessen, R. S., Binney, J., Magorrian, J. & Smith, R., 2018b. A theoretical explanation for the Central Molecular Zone asymmetry. *MNRAS*, **475**, 2383–2402

1. Sormani, M. C., Sobacchi, E., Fragkoudi, F., Ridley, M., Tress, R. G., Glover, S. C. O. & Klessen, R. S., 2018a. A dynamical mechanism for the origin of nuclear rings. *MNRAS*, **481**, 2–19

The work of these two papers grew out of the ideas presented in Ridley et al. (2017). I contributed to the discussions of each and gave editorial feedback to the main author. My contributions were limited, so I have not reproduced any of the content here, except to mention where relevant the results for context.

Chapters 4 and 5 are purely my own work, as yet unpublished.

To Mum and Dad.

Contents

1 Introduction **1**

1.1 The ISM in the Milky Way 3

1.2 Epicycles, resonances, and orbits in barred potentials 9

1.3 The ISM in the Galactic center 14

1.4 An Overview of this thesis 16

2 Numerical Methods **18**

2.1 Introduction 18

2.2 Hydrodynamic codes 19

2.2.1 Shocks 20

2.2.2 The second-order flux splitting method (FS2) 21

2.2.3 PLUTO 24

2.3 Rigid bar models 25

2.4 N-body modelling 26

2.4.1 GROMMET 27

2.5 Generating N-body models of barred galaxies 29

2.5.1 The bulge and halo 29

2.5.2 The disc 32

2.5.3 Gas 34

3 A Dynamical Model of the CMZ **36**

3.1 Introduction 36

3.2 Data 38

3.3 Methods 40

3.3.1 The potential 40

3.3.2 Numerical scheme 47

3.4 Gas dynamics 48

3.4.1 Large-scale gas flow 48

3.4.2 Nuclear spirals 49

3.5 Discussion 52

3.5.1 Interpretation of (l, v) features and face-on map of the CMZ . 52

3.5.1.1 Arms I and II 52

3.5.1.2 1.3° cloud complexes 53

3.5.1.3 Placement of prominent molecular clouds 54

3.5.1.4 Summary 56

3.5.2 Unsteady flow in the CMZ 56

3.5.3 Comparison with previous work 62

3.5.4 Follow-up work 64

3.6 Conclusion 65

4 Gas Flow in Live N-body Potentials **68**

4.1 Introduction 68

4.2 Our reference N-body model 70

4.2.1 Initial conditions 71

4.2.2 Characteristics of the N-body model 74

4.3 Gas flow in the live N-body potential 83

4.3.1 How stationary is the gas flow? 86

4.3.2 Mock observations 91

4.4 How do rigid models compare? . . . 92
4.4.1 A frozen N-body model . . . 92
4.4.2 The frozen N-body monopole and quadrupole . . . 94
4.4.2.1 The influence of the off-centering . . . 96
4.4.3 An analytic bar model . . . 98
4.5 Observational consequences . . . 101
4.5.1 Varying the pattern speed . . . 102
4.5.2 Varying the quadrupole . . . 105
4.5.3 Quantitatively comparing (l, v) diagrams . . . 109
4.6 Discussion . . . 117
4.7 Conclusions . . . 120

5 The Tilted Inner Gas Disc 122

5.1 Introduction . . . 122
5.2 The vertical distribution of gas in the inner Galaxy . . . 123
5.2.1 A tilted disc model of the CMZ . . . 125
5.3 Nuclear discs in N-body potentials . . . 128
5.3.1 Quantifying the orientation of the central gas disc . . . 128
5.3.2 The central disc in our reference model . . . 130
5.3.3 The gas disc in a noisy N-body potential . . . 132
5.3.4 Is the gas following ballistic trajectories? . . . 134
5.4 Discussion . . . 138
5.5 Conclusions . . . 140

6 Conclusions 142

6.1 Future Work . . . 143

Appendix A A Resolution Test 145

A.1 A higher resolution N-body model . . . 145

Bibliography **I**

List of Figures

1.1 An ideal (l, v) plot. 4

1.2 Brightness temperature of the HI 21 cm line emission for $|b| < 4°$ from Kalberla et al. (2005). 4

1.3 Brightness temperature of the ^{12}CO $J = 1 \rightarrow 0$ emission line for $|b| < 4°$ from Dame et al. (2001). 5

1.4 The outer x_1 family of closed orbits in a barred toy potential 11

1.5 The x_2 family of closed orbits in a barred toy potential 11

1.6 The inner x_1 family of closed orbits in a barred toy potential 12

1.7 A sequence of x_1 and x_2 orbits projected into the (l, v) plane. 13

1.8 Brightness temperature of the ^{12}CO $J = 1 \rightarrow 0$ emission line from the Galactic center (Dame et al., 2001). 14

3.1 NH_3 $(1 - 1)$ data from the HOPS survey (Purcell et al., 2012) 40

3.2 The data of Fig. 3.1, with features of interest highlighted in various colors. 41

3.3 The circular velocity curve for the potential used in this chapter. . . . 43

3.4 The quadrupole Φ_2 and octupole Φ_4 of the potential used in this chapter. The non-axisymmetric components of the potential are all entirely generated by the bar, given by Equation 3.5. 44

3.5 Enclosed mass within spheres of radius R for our model. 46

3.6 The fluid density of the simulation at 280Myr. 51

3.7 Features of the gas flow in the simulation highlighted in various colours. 57
3.8 A face-on schematic view of the model of the CMZ. 58
3.9 The fluid density of the simulation with characteristic features of the wiggle instability highlighted in the flow. 59
3.10 The same as Fig. 3.7, for the earlier point of the simulation with two additional features of the flow highlighted. 60

4.1 The time evolution of the surface density of the stellar components of the mode. 74
4.2 The stellar density at 2 Gyr, just before the gas is added. 75
4.3 The time evolution of the first few Fourier amplitudes in the disc. . . 76
4.4 The velocity curve calculated from the monopole component of the N-body potential at 2 Gyr. 78
4.5 The positions of the centres of mass of the three components of the N-body model during the pure-N-body evolution. 78
4.6 The positions of the centre of stellar mass of all stellar particles as a function of radius. 79
4.7 Contours of the potential in the inner 100 pc in the (x, y) plane for two snapshots close to the end of the pure N-body simulation. 80
4.8 The first few multipoles of the N-body potential. 81
4.9 The power spectrum of the $m = 2$ component of the density in the (R, Ω) plane. 83
4.10 The time evolution of the gas surface density of the model. The stellar surface density is also plotted with white contours. 84
4.11 A slice of the gas density through the $y = 0$ plane, for the same snapshots as seen in Figure 4.10. 85
4.12 The positions of centres of mass of the components of the model. . . . 86

4.13 A comparison between the quadrupole of the N-body potential before and after the gas evolution. 87
4.14 The gas surface density in the (x, y) plane for 3 snapshots during the gas evolution separated by 12 Myr. 89
4.15 The surface density of the gas 200 Myr after the gas is released, and an (l, v) plot created from the model. 90
4.16 Features of the gas flow highlighted in the (x, y) plane, and their corresponding traces in the (l, v) plot. 90
4.17 A comparison between gas flow in the live N-body simulation and a simulation in a rigidly rotating frozen snapshot of the N-body potential. 93
4.18 A comparison between gas flow in the live N-body simulation and a simulation in a rigidly rotating potential consisting only of the monopole and quadrupole of the N-body potential, together with synthetic (l, v) plots created from each model. **Top row:** The live N-body +gas simulation. **Bottom row:** The gas simulation in a potential consisting of only the monopole and quadrupole components of the N-body potential. The right column shows the final gas density, and the left column shows the corresponding (l, v) plots. Again features from the live model have been plotted in red over the rigid (l, v) plot. 95
4.19 A close up view of the gas flow in the centre of the reference model and the N-body monopole + quadrupole simulation. 97
4.20 A comparison between the quadrupole moment of the N-body potential and the analytic quadrupole model of Equation 4.8. 98
4.21 A comparison between gas flow in the live N-body simulation and a simulation in a rigidly rotating potential consisting only of the monopole of the N-body potential and an analytic quadrupole 99

4.22 The gas surface density in each of the three potentials as the pattern speed of the bar is varied from 25 to 45 $\mathrm{km\,s^{-1}\,kpc^{-1}}$. 103
4.23 Corresponding (l, v) plots for the simulations shows in Figure 4.22. . . 104
4.24 The gas surface density in the two monopole + quadrupole potentials as the quadrupole strength is varied from 0.8 to 1.2. 105
4.25 Corresponding (l, v) plots for the simulations shows in Figure 4.24. . . 106
4.26 The gas surface density in the two monopole + quadrupole potentials as the length of the quadrupole is scaled by 0.8 to 1.2. 107
4.27 Corresponding (l, v) plots for the simulations shows in Figure 4.26. . . 108
4.28 The results of applying the automated ridge finding algorithm of Sormani & Magorrian (2015) to the (l, v) plot of the live N-body model. 110
4.29 The SMHD distance between the live N-body model and simulations in the three model potentials a function of Ω_p. 113
4.30 The SMHD distance between the live N-body model and rigid simulations as a function of the strength of the quadrupole, $\tilde{A}$, from 0.8 to 1.2. 114
4.31 The SMHD distance between the live N-body model and rigid simulations as a function of the scale length of the quadrupole, $\tilde{r}$, from 0.8 to 1.2. 115
4.32 Contours of SMHD distance between the live N-body simulation and a grid of simulations with a potential consisting of the N-body monopole and quadrupole. 116
4.33 As Figure 4.32, but for the N-body monopole + analytic quadrupole potential. 116

5.1 A crude 3D model of the CMZ produced by inclining and tilting the simulation as a razor thin disc. 125

5.2 A zoom in view of the x_2 disc in the reference model of Chapter 4 during the simulation. 129
5.3 The angles defining the orientation of $\hat{\mathbf{n}}$ of the CMZ during the evolution of the simulation. 130
5.4 A zoom in view of the x_2 disc at various stages during the low resolution N-body simulation. 133
5.5 The angles defining the orientation of $\hat{\mathbf{n}}$ of the CMZ in the low resolution N-body potential during the evolution of the simulation. 133
5.6 The orbit frequency Ω (solid line) and the vertical epicyclic frequency ν (black line) calculated from the azimuthally averaged potential. . . 136
5.7 The time period of precession $T_n = 2\pi/\Omega_n$ of the plane of an inclined orbit in the central regions of the potential. 136
5.8 The angles defining the orientation of $\hat{\mathbf{n}}$ of the disc of test particles during the evolution of the simulation. 137

A.1 The final state of the gas in the higher resolution N-body model, and a mock (l, v) plot created from the model. 146
A.2 The SMHD distance between the live high resolution N-body model and simulations in the three model potentials a function of Ω_p. 148
A.3 The SMHD distance between the highres live N-body model and rigid simulations as a function of the strength of the quadrupole, $\tilde{A}$, from 0.8 to 1.2. 149
A.4 The SMHD distance between the highres live N-body model and rigid simulations as a function of the scale length of the quadrupole, $\tilde{r}$, from 0.8 to 1.2. 150
A.5 Contours of SMHD distance between the highres live N-body simulation and a grid of simulations with a potential consisting of the N-body monopole and quadrupole. 151

A.6 As Figure 4.32, but for the N-body monopole + analytic quadrupole potential. 151

List of Tables

4.1 Parameters of the reference model. 71

5.1 Parameters of the low resolution toy model. 132

A.1 Parameters of the higher resolution model. 145

Chapter 1

Introduction

We reside in the Milky Way, a barred spiral galaxy. Our species has studied the Milky Way since the first humans peered up into the night sky and wondered about the diffuse band of light that stretched from horizon to horizon, but it is only in the last few centuries that we have really begun to understand our Galaxy and its place in the wider Universe.

In 1750AD Thomas Wright first suggested that the appearance of the Milky Way on the sky was a projection effect due to our place in a flat layer of stars. This was expanded upon by Immanuel Kant in 1755AD, when he suggested that the Milky Way could be a gravitationally bound stellar disc, supported by ordered rotation in the same way as the solar system. The first reasonably accurate estimates of the size of the Milky Way and the position of the sun relative to the Galactic centre were given by Harlow Shapley in the early twentieth century. He used observations of globular clusters orbiting high above and below the Galactic disc to come within a factor of two of modern estimates (Shapley, 1918a,b, 1919).

The existence of external galaxies outside the Milky Way was a contentious issue. Astronomers have been aware of nebulae, "fuzzy" sources of light on the sky, since at least 150AD when Ptolemy described the appearance of several nebulous stars in

his *Almagest*. By the eighteenth century observers such as Messier and Herschel had catalogued a great many nebulae, noting their wide variety of morphologies. Some of the brightest and closest could be resolved into clusters of individual stars. Another family of objects, the planetary nebulae, seemed to consist of stars surrounded by rings of gaseous material. Many of the remaining objects seemed to fall into one of two categories; smooth elliptical systems, and more irregular disc-like objects containing whirlpools or spiral-shaped patterns.

Althought it was suggested relatively early in the study of these nebulae that these systems were distinct *island universes* much like the Milky Way, it took much debate before this became recognised as scientific fact. Given their apparent size, and the extent of the Milky Way, for the spiral nebulae to have a similar intrinsic size would mean that they existed at uncomfortably large distances from the Sun. It took the identification of Cepheid variable stars in the Andromeda nebula by Edwin Hubble to finally convince the community of the existence of galaxies outside the Milky Way.

Galaxies are often described as the building blocks of the Universe. Whether or not this is an appropriate analogy, galaxies are incredibly interesting objects. The amazing visual variety of galaxies has captured the imaginations of astronomers and non-scientists alike. A galaxy is a gravitationally bound system of stars, gas and dust embedded in a roughly spherical distribution of poorly understood "stuff" we call dark matter. In the modern theory of hierarchical structure formation galactic halos are understood to have initially formed from the collapse of small over-densities in the early Universe. The galaxies we observe today are the result of continuous accretion of gas and other smaller systems, and mergers between similarly sized systems. The study of the formation and evolution of galaxies encompasses a huge number of different physical processes; from quantum fluctuations in the early universe, to the physics of star formation and supernovae, to the gravitational dynamics of secular processes in galactic discs.

By far the most well understood galaxy is of course our own. It is the only system for which we can study in detail the individual motions of stars, and not just integrated properties such as surface brightness and velocity dispersions. This is enabled by our privileged position within the Galactic Disc, but this brings with it an additional problem, extinction.

Dust is the bane of astronomical observations. Tiny grains of solid material embedded in the gas that makes up the interstellar medium (ISM) of the Milky Way absorb optical light. This absorption is strongly biased towards shorter wavelengths, leading to a general "reddening" of sources obscured by dust. The ISM of the Milky Way is well confined to the plane of the disc, so extinction mostly affects our observations into the inner and outer disc.

Modern study of the Milky Way relies heavily on optical and near-IR surveys of individual stars. The GAIA mission is mapping the 3D positions and velocities of over a billion stars in the Milky Way (Gaia Collaboration et al., 2016). Its predecessor was the HIPPARCOS satellite which mapped out over 2 million stars (ESA, 1997). Spectroscopic surveys such as RAVE (Kunder et al., 2017) and APOGEE (Majewski et al., 2017) have enabled the systematic study of the chemical composition and physical properties of a large number of stars in the Galaxy. This explosion of available data in recent years has led to similarly huge jumps in our understanding of the Galaxy. Nonetheless, these studies are all still hampered by extinction, limiting what we can infer about the Galactic centre and disc. Constructing a complete picture of the Milky Way requires we find some way to peer through the dust.

1.1 The ISM in the Milky Way

Much of our knowledge of the inner region of the Milky Way comes from large scale radio surveys of the interstellar medium. The two most important emission lines

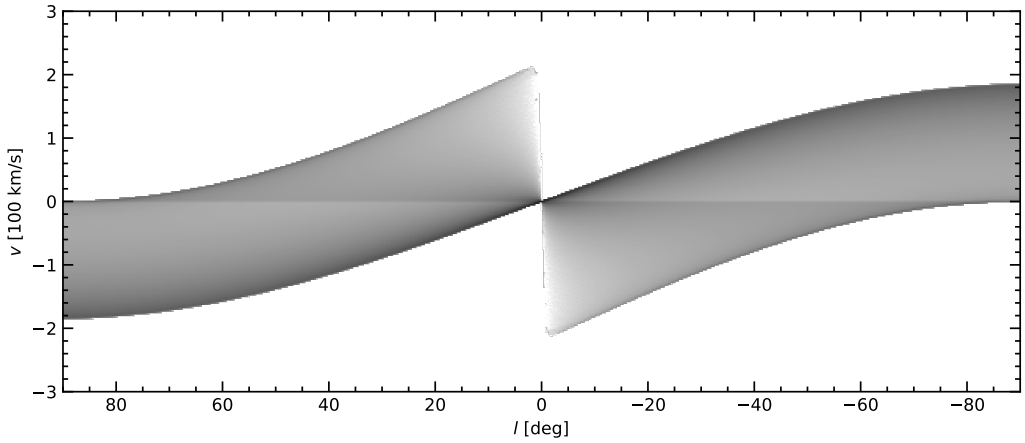

Figure 1.1: A mock (l, v) plot, created from a model of optically thin gas on perfectly circular orbits with $v_c = 220\,\mathrm{km\,s^{-1}}$ everywhere in the disc, assuming $R_\odot = 8\,\mathrm{kpc}$ and $v_\odot = 220\,\mathrm{km\,s^{-1}}$.

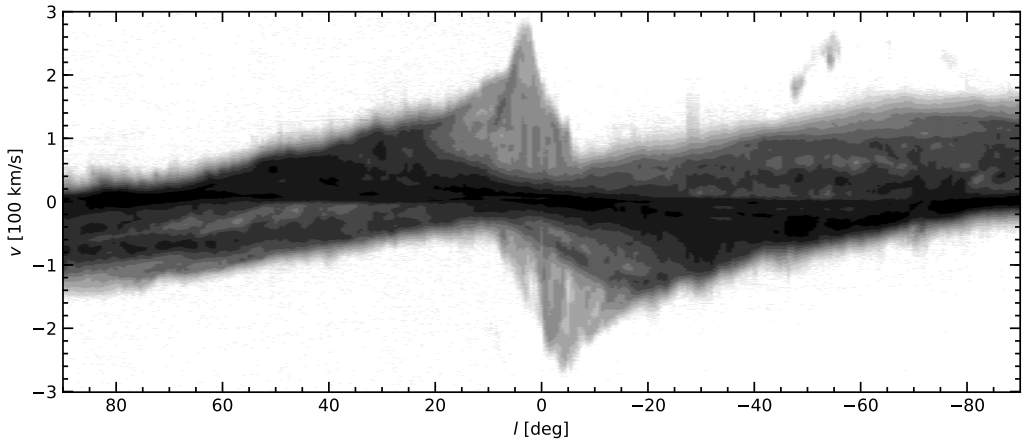

Figure 1.2: Brightness temperature of the HI 21 cm line emission for $|b| < 4°$ from Kalberla et al. (2005).

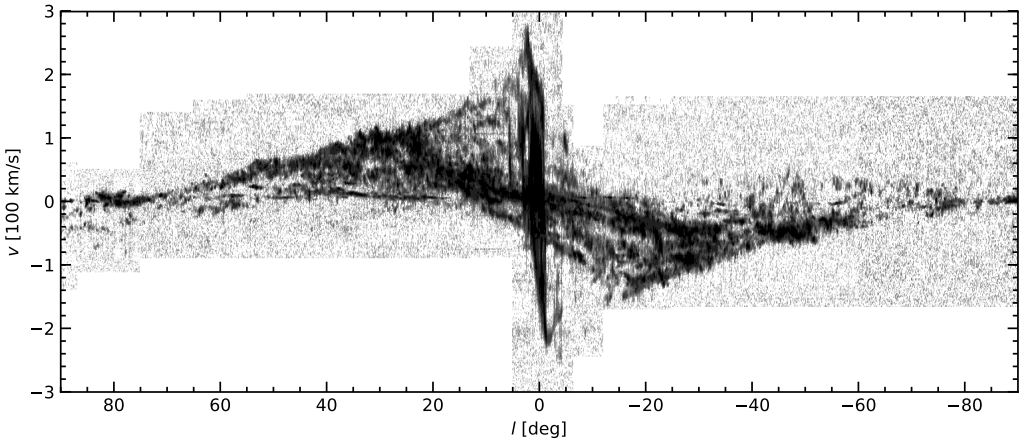

Figure 1.3: Brightness temperature of the ^{12}CO $J = 1 \rightarrow 0$ emission line for $|b| < 4°$ from Dame et al. (2001).

are the 21-cm neutral hydrogen line at 1.4202 GHz, corresponding to the transition between the two hyperfine levels of the ground state of HI, and the several mm length CO rotational transitions at around ~ 100 GHz. In general the 21-cm line is optically thin in the ISM, but this is not true for CO, which mostly exists in dense molecular clouds. However provided cloud-cloud crowding is not too important, as expected in the Milky Way, we can approximate it as optically thin (Binney & Merrifield, 1998).

When the first surveys of the 21-cm line of HI were carried out astronomers were for the first time able to get a clear idea of the large scale structure of the MW (Oort et al., 1958). However, with this new insight came new puzzles. The general understanding of the time was that the Milky Way was rotationally symmetric, and therefore that the gas should occupy roughly circular orbits. While the gas kinematics outside $R \sim 5\,\mathrm{kpc}$ could be well understood in terms of circular motion, observations from the inner Galaxy showed clearly non-circular kinematics.

Galactic coordinates are used to specify the position of a point on the sky relative to the orientation of the Milky Way. The Galactic equator is the great circle on the sky that is closest to the plane of the Galaxy. The Galactic latitude of a point on the sky, b, is the angle between the line-of-sight to this point and the Galactic equator,

measured perpendicularly to the equator. The Galactic longitude, l, is the position along the equator measured with respect to the rotational centre of the Milky Way. Our best estimate of the actual centre of the Galaxy, the supermassive black hole Sgr A*, actually lies at $l = 0^\circ\,04'\,06''$, as it was discovered after the definition of the Galactic coordinate system (Reid & Brunthaler, 2004).

Observational surveys of a given emission line produce a "data cube". At each point on the sky, (l, b), and for each line-of-sight velocity v the intensity of emission is recorded. Data of this type is usually displayed with an (l, v) plot, where we integrate over the less interesting coordinate b. A mock (l, v) plot, created from a model disc of optically thin gas on perfectly circular orbits with $v_c = 220\,\mathrm{km\,s^{-1}}$ is shown in Figure 1.1. The emission is smooth and featureless, and perfectly symmetric about the centre. The envelopes of the (l, v) plot peak around $l = 0$ at the circular velocity, and generally decline outwards to $l = \pm 90^\circ$. Despite the uniform density in (x, y) the emission is stronger at the envelopes due to crowding in velocity space at the point where the line-of-sight is tangential to the orbits.

Notably the regions at small $\pm l$ and $\mp v$ are completely devoid of emission. These are referred to as *forbidden velocities*, so called because material inside the solar circle on purely circular orbits would not occupy this region of (l, v) space. The straight line at $v = 0$ is a projection effect. For $\pm l$ material inside the solar circle is moving at $\pm v$, and material outside the solar circle at $\mp v$. Our line of sight intersects the orbits of material inside the solar circle twice, but outside only once, thus causing the discontinuous jump in intensity and $v = 0$.

Figure 1.2 is an (l, v) plot created from 21 cm HI emission line data from Kalberla et al. (2005) averaged over $|b| < 4^\circ$. An (l, v) plot of 2.6mm ^{12}CO data from Dame et al. (2001) is shown in Figure 1.3. Firstly it is clear that the simple model explains the large scale picture of the data, so cannot be too far from reality. As one would expect the molecular and atomic emission largely follow each other, although the

molecular gas is patchier and more concentrated towards the centre of the Galaxy as it traces the dense component of the ISM. But is it also clear that our simple model is far too naive.

The principal differences between the idealised model and the real data are:

- The are broad coherent ridges spanning the width of the (l, v) plot. These are present in both HI and CO data, and coincide with bumps on the envelope at their maximum extent.
- The envelope reaches much higher velocities at small l, $|v| \sim 270\,\mathrm{km\,s^{-1}}$, than would be expected from circular motion with a reasonable rotation curve.
- There is plenty of emission at the *forbidden velocities* in the few degrees either side of $l = 0$.
- In the central few degrees there exists a strong parallelogram shaped region of emission in the CO data, extending over several 100 $\mathrm{km\,s^{-1}}$. This is not seen in the HI data.
- The data is asymmetric about the Galactic Centre. This is particularly noticeable in CO in the inner regions.

At least some of these features can be explained by the presence of spiral arms in the disc. Already at the time of the first surveys it was well accepted that the Milky Way is a spiral galaxy (Oort et al., 1958). As shown by Roberts (1969), even a weak spiral potential can produce a highly non-linear response in the gas. Spiral patterns produce both density enhancements and velocity crowding that result in the strong bands of emission crossing the (l, v) plot in the HI and CO data.

The high velocity peaks and emission at forbidden velocities can both be explained if gas in the centre of the Galaxy deviates strongly from circular motion. Historically there have been two principal hypotheses for the source of this non-circular motion.

The first was that the gas had a strong radial component of motion because it was expanding outwards. The second was that the gas was on highly elliptical orbits due to the presence of a strong stellar bar in the disc of the Milky Way.

The expansion hypothesis suggested that the neutral gas in the central few kpc of the Galaxy was expanding outwards with a radial velocity of $\sim 100\,\mathrm{km\,s^{-1}}$ (e.g. Rougoor & Oort, 1959; Oort, 1977). Possible mechanisms generating this expansion included a burst of supernovae or magnetic fields. However it was recognised that this explanation had problems, most notably that the observed rate of expansion would completely deplete the Galactic center of gas in just a few million years.

The alternative hypothesis, proposed originally by de Vaucouleurs (1964), was that the centre of the Milky Way contained a bar. Already it was known that stellar bars are reasonably common in external galaxies. Convincing evidence for the existence of the Galactic bar came from two fronts. Firstly it was shown by Binney et al. (1991) that the bar could naturally explain many features of gas observations from the central few kpc. Secondly, direct evidence for the bar was observed in near-IR photometric data of the inner Galaxy (Blitz & Spergel, 1991; Weiland et al., 1994; Binney et al., 1997).

Interestingly, recent observations have detected kpc-scale bubbles of gamma-ray emission, the so-called "Fermi-bubbles", above and below the Galactic disc, emanating from the Galactic Centre (Su et al., 2010). These are believed to be generated by a recent massive injection of energy into the ISM in the centre of the Galaxy, somewhat similar to the original expansion hypothesis.

1.2 Epicycles, resonances, and orbits in barred potentials

The argument of Binney et al. (1991) was based on closed orbits in barred potentials. These are the key to understanding the dynamics of gas in the centre of the Milky Way. The stable closed orbit families in a given potential provide the backbone of the general orbital structure, as most orbits can be understood in terms of epicyclic oscillations around a particular closed orbit.

Due to its collisional nature, closed orbits are even more important for gas orbiting the galaxy. Dissipative processes will quickly dampen any excursions gas clouds make around the closed underlying orbit. We should expect that, provided the gas has enough time to settle roughly into equilibrium, the gas streamlines should closely follow the underlying closed orbit structure of the potential, perhaps modified slightly by pressure forces.

To understand the closed orbits in a rotating barred galaxy such as the Milky Way, we first consider the weak bar case. Consider a star moving in a potential with a weakly non-axisymmetric component rotating with a steady pattern speed $\Omega_{\rm p}$. In a frame corotating with the potential we write the potential as

$$\Phi(R,\phi) = \Phi_0(R) + \Phi_1(R)\cos(m\phi), \tag{1.1}$$

where m is a positive integer ($m = 2$ corresponding to a barred perturbation), and $|\Phi_1/\Phi_0| \ll 1$. As the non-axisymmetric component of the potential is weak the star will follow an almost circular orbit. For epicyclic motion around a circular orbit at R_g the star has two natural frequencies, the orbital frequency,

$$\Omega^2 = \left(\frac{1}{R}\frac{\partial\Phi_0}{\partial R}\right)_{R_g} \tag{1.2}$$

and the frequency of small radial excursions about the circular orbit, the radial epicyclic frequency,

$$\kappa^2 = \left(R\frac{\mathrm{d}\Omega}{\mathrm{d}R} + 4\Omega^2 \right)_{R_g}. \tag{1.3}$$

For the most part we can treat the non-axisymmetric disturbance as small, and the stars motion is close to the axisymmetric case, i.e. almost circular. Resonances occur when the forcing frequency Ω_p equals one of the natural oscillating frequencies of the star. The most important resonances are the corotation resonance (CR), the guiding centre radius that satisfies

$$\Omega_0 = \Omega_\mathrm{p}, \tag{1.4}$$

which occurs where the star is orbiting at the same frequency as the potential, and the inner (+) and outer (-) Lindblad resonances where

$$m(\Omega_0 - \Omega_\mathrm{p}) = \pm\kappa. \tag{1.5}$$

An inner Lindblad resonance (ILR) occurs when the star orbits more quickly than the rotating pattern of the potential, encountering successive peaks of the potential at the epicyclic frequency κ, and the outer Lindblad resonance (OLR) occurs in the same situation but when the star is orbiting more slowly than the potential. Depending on the form of the potential and value of Ω_p, two, one or zero ILRs may exist, but for most realistic mass distributions the potential will have a CR and OLR. There exist other resonances at various integer ratios, such as the 4:1 ultra-harmonic resonance (e.g. Binney & Tremaine, 2008), but these are of secondary importance to the dynamics of gas.

In a strongly barred rotating potential the epicyclic approximation is no longer valid. Instead we must turn to numerically studying the closed orbit families in a given potential. The two most important families of prograde stable orbits in a barred potential are the x_1 and x_2 orbit families (Contopoulos & Papayannopoulos,

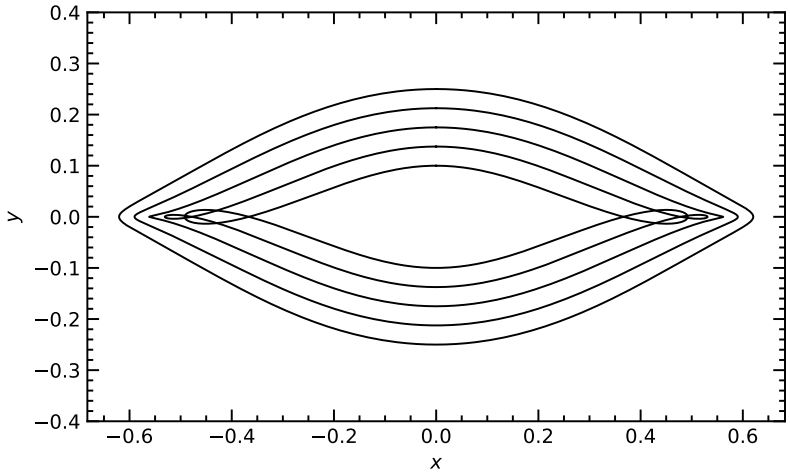

Figure 1.4: The outer x_1 orbits in the potential of Equation 1.6, where they become self-intersecting. Outside this region they become less and less elongated, as orbits far outside the bar orbit much more slowly, and so the non-axisymmetry of the potential is smoothed out at the bar rotates several times over a single orbital period. The major axis of the bar lies along the x-axis.

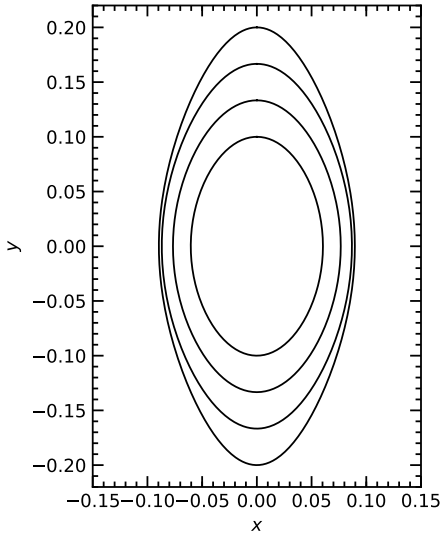

Figure 1.5: The x_2 orbit family of the barred potential. These are elongated perpendicular to the major axis of the potential, and only exist between the two energies corresponding to the ILRs of the potential.

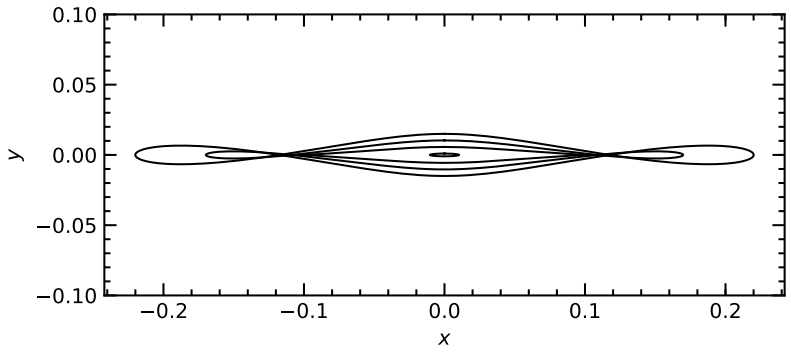

Figure 1.6: Some of the inner-most x_1 orbits in the rotating barred potential of Equation (1.6).

1980). We consider the simple toy barred potential

$$\Phi(x, y) = \frac{1}{2} v_0^2 \log(R_c^2 + x^2 + y^2/q^2), \tag{1.6}$$

rotating with pattern speed $\Omega_p = 100\,\mathrm{km\,s^{-1}\,kpc^{-1}}$, with $v_0 = 100\,\mathrm{km\,s^{-1}}$, $R_c = 0.3\,\mathrm{kpc}$ and $q = 0.8$. We study the closed orbits in a frame corotating with the potential.

The x_1 orbit family is elongated parallel to the bar major axis. At high energies (large radii) these are almost circular. Moving closer inwards they become increasingly elongated, eventually becoming "bowtie" shaped with self-intersecting loops at the tips (Figure 1.4). This energy roughly corresponds to the outer-ILR radius in the weak bar case. At this energy the second family of stable closed orbits appears, the x_2 family (Figure 1.5). These are elongated perpendicularly to the bar axis. Very close to the centre of the potential, at roughly the inner-ILR, the x_2 family disappears again, and the x_1 orbits stop self-intersecting (Figure 1.6).

Now consider releasing gas into the outer regions of the potential described above. It would settle onto the x_1 orbits, and as collisions between gas clouds dissipated energy the gas would slowly follow the series of x_1 orbits inwards into the potential. A collisional fluid cannot follow self-intersecting orbits, so shocks would form at the

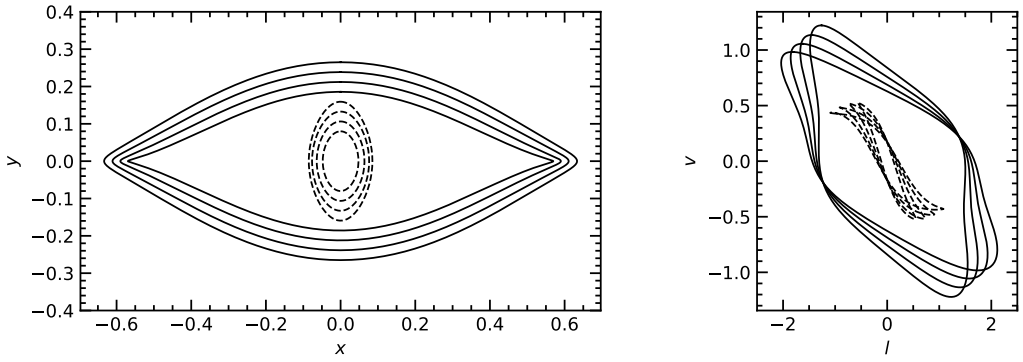

Figure 1.7: A selection of outer x_1 orbits and inner x_2 orbits, with their projections to the (l, v) plane. Gas on a similar sequence of orbits in the barred potential of the Milky Way would explain the non-circular motions observed in the Galactic center.

tips of the cusped x_1 orbit. The gas would lose energy at these shocks, and fall onto the more tightly bound x_2 orbits in the centre of the galaxy.

The right panel of Figure 1.7 shows a sequence of outer x_1 orbits just outside the cusped orbit, and the inner x_2 orbits. These orbits are projected into the (l, v) plane in the left hand panel, assuming an observer at $R = 8\,\mathrm{kpc}$ on a circular orbit with the GC-observer line making an angle of 20° to the bar major axis. The line-of-sight velocities of the highly elongated x_1 orbits reach well above the circular velocities, and they extend far into the regions of forbidden emission. The x_2 orbits trace out a similar, smaller parallelogram in the centre.

In the model proposed by Binney et al. (1991) gas occupying the elongated x_1 orbits is responsible for emission at the *forbidden velocities* in Figures 1.2 and 1.3. The molecular gas would be mostly produced in the shocks at the cusped orbit, the trace of which would produce the parallelogram seen in CO emission. The high velocity peaks of the (l, v) envelope are the result of gas streaming down the bar, with a large line-of-sight velocity component. The argument played a major role in convincing the wider astrophysics community of the existence of the bar in the Milky Way.

The picture has been extremely successful in explaining the gas flow in the cen-

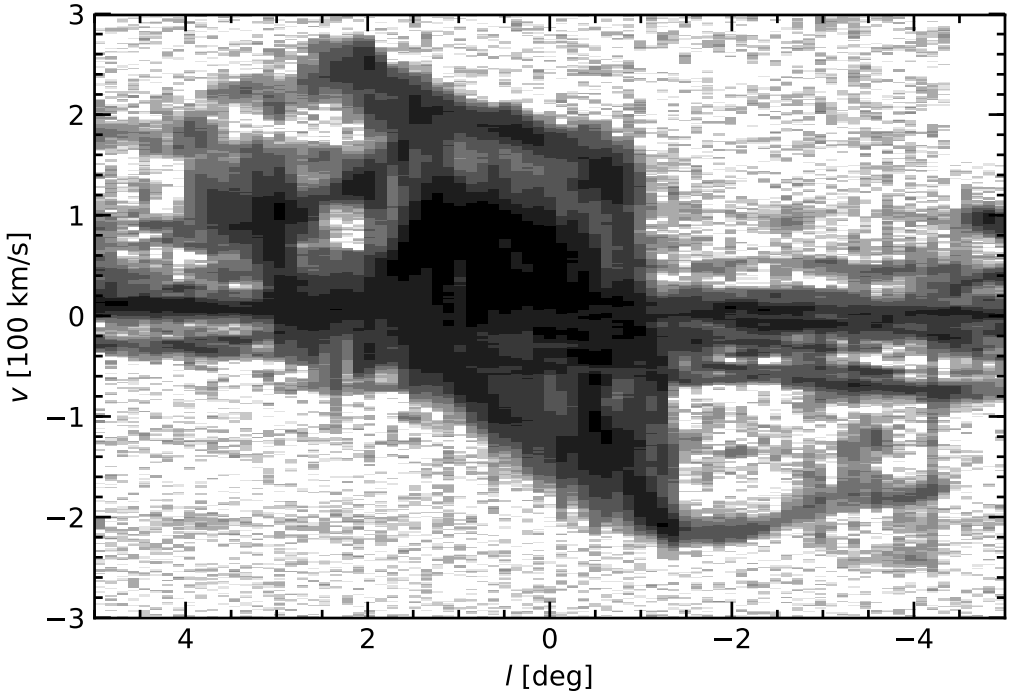

Figure 1.8: An (l, v) plot of the inner 5° in CO from Dame et al. (2001), highlighting the concentration of molecular gas and the asymmetry of emission about the Galactic center.

tral regions of the galaxy. Hydrodynamic simulations have confirmed that in barred potentials gas streamlines do indeed closely follow the closed orbits of the potential, in the manner described above (Jenkins & Binney, 1994; Athanassoula, 1992; Rodriguez-Fernandez & Combes, 2008; Sormani et al., 2015a).

1.3 The ISM in the Galactic center

Molecular gas in the Milky Way is strongly concentrated to the centre. Roughly half of the total molecular gas of the Milky Way is contained in the molecular ring (Binney & Merrifield, 1998), with a radius of 4 kpc. A region of considerable recent interest to astronomers is the Central Molecular Zone (CMZ). This is the innermost $\sim$ 500 pc of the MW, and contains some 10% of the Milky Way's molecular gas budget ($\sim 10^7\,M_\odot$, Ferrière et al. 2007). Gas flow in the CMZ has a particularly rich

and complex structure. Figure 1.8 shows an (l, v) plot for $|l| < 5°$ for ^{12}CO data from Dame et al. (2001). The kinematics show significant departures from circular motion, the molecular gas is strongly concentrated within the central few degrees, and emission is highly asymmetric about the Galactic center (GC) (e.g. Bally et al., 1988).

It is clear that the dynamics of gas in the CMZ must be understood in the context of gas flowing in a barred potential. As discussed above, gas in the CMZ follows x_2 orbits. Hence the CMZ is sometimes referred to as the x_2 disc. The CMZ is fed gas by shocks (Rodriguez-Fernandez et al., 2006), which efficiently bring material inwards onto the x_2 orbits from the outer parts ($R \simeq 2 - 3\,\mathrm{kpc}$).

High resolution molecular line studies of the CMZ reveal coherent features spanning the width of the (l, b, v) data cubes in several different species, including CO, CS, NH_3 and HNCO (Nagayama et al., 2007; Oka et al., 2007; Henshaw et al., 2016b). The origin of these features has been of interest for several decades, and proposed explanations include two spiral arms (Sofue, 1995; Sawada et al., 2004), a twisted elliptical orbit (Molinari et al., 2011), or an open stream (Kruijssen et al., 2015).

The physical conditions within the CMZ are far more extreme than in the Solar neighbourhood and outer regions of the Galaxy. Despite the extremely high column densities and pressures, star formation in the CMZ seems to be suppressed by at least an order of magnitude compared to what is predicted by our current understanding of star formation (e.g. Schmidt, 1959; Kennicutt, 1998; Longmore et al., 2013a; Kruijssen et al., 2014; Battersby et al., 2016). Longmore et al. (2013a) estimates the total SFR of the CMZ as $\sim 0.1\,\mathrm{M_\odot yr^{-1}}$, compared to a rate of $\sim 2 - 1\,\mathrm{M_\odot yr^{-1}}$ as predicted from classical star formation relations. A proper understanding of the structure and dynamics of gas in the CMZ may help reconcile this contradiction, and give us insight into the mechanics of star formation.

1.4 An Overview of this thesis

This work is generally focused on the study of the dynamics of gas in barred potentials, with a particular focus on the ISM in our own galaxy, the Milky Way. We are principally concerned with the following question: How can we use models of gas flow in barred potentials to understand observations of the MW, and can we use gas as a dynamical tracer to constrain the potential of the inner Galaxy?

In Chapter 2 we begin by discussing the various numerical schemes used in this thesis. This work relies heavily on the results of numerical calculations, and here we review the various algorithms and programs that are used in later chapters. We discuss the various hydrodynamical codes that are used to evolve gas in our models, the different ways we model the potential of the Milky Way, and the recipes used to construct initial conditions for our simulations.

In Chapter 3 we present a simple two dimensional hydrodynamical simulation in a rigid model of the potential of the Milky Way, and use it to suggest a dynamical interpretation of observations of the CMZ. We compare and contrast our model with alternative theories from the literature, and argue that it can naturally account for many features of the observations.

Next we examine the dynamics of gas flow in a live N-body potential. We construct an isolated barred N-body galaxy model, and run a three dimensional hydrodynamic simulation in the time dependent gravitational potential of the N-body component. We investigate the effect of the fluctuations and asymmetry of the potential on the gas flow, and ask if rigid bar models are good approximations to gas flow in the live potential. The parameter space of such models is large, so we also investigate whether the use of automated fitting methods can assist in fitting such models to observations.

Much of the discussion so far has focused on the dynamics of gas in the plane of the Galaxy. The vertical distribution of the ISM is non-trivial, particularly in the

center. In Chapter 5 we examine the vertical dynamics of gas in our models, and ask if we can learn anything interesting about the inner potential from the observed vertical configuration of the CMZ.

Finally, in Chapter 6, we wrap things up. We summarise the findings of each chapter, the successes and failures of our models, and highlight important avenues for future investigations.

Chapter 2

Numerical Methods

2.1 Introduction

This thesis makes extensive use of the results of numerical simulations. In the following chapters we are presented with the problem of solving several different partial differential equations, notably the equations of hydrodynamics, the collisionless Boltzmann equation, and Poisson's equation. Aside from an unfortunately small subset of problems these cannot be solved analytically, so we use numerical algorithms to find the solutions. There are a myriad of recipes to solve each problem. An understanding of the advantages and drawbacks of each approach is important to avoid interpreting numerical artefacts as a feature of the underlying physical problem.

This chapter provides an overview of the numerical methods used in the following chapters to solve these problems, and is intended to serve as a reference for the rest of the thesis, so that the later chapters can focus on the interesting results of the solutions and not the details of finding the solutions.

2.2 Hydrodynamic codes

The equations governing the motion of a fluid can generally be written as a system of conservation laws

$$\frac{\partial \mathbf{U}}{\partial t} + \nabla \cdot \mathbf{F} = \mathbf{S} \tag{2.1}$$

where $\mathbf{U}$ is a vector of conserved quantities (e.g. mass and momentum) describing the state of the fluid, $\mathbf{F} = \mathbf{F}(\mathbf{U})$ is a vector of fluxes, and $\mathbf{S} = \mathbf{S}(\mathbf{U})$ is a source term, including the gravitational acceleration $-\nabla\Phi$, and pressure forces P. In this thesis we model the ISM as an inviscid fluid, neglecting any viscosity.

Equation (2.1) requires an additional equation to solve. This relates the pressure P to properties of the fluid, and is known as the equation of state. In all the simulations presented in this thesis we assume a very simple equation of state for the gas, the isothermal equation of state:

$$P = c_s^2 \rho. \tag{2.2}$$

When modelling the ISM as isothermal the sound speed is a phenomenological sound speed that is meant to take into account the effects of small-scale turbulence (e.g. Roberts, 1969; Cowie, 1980). Therefore "temperature" in our isothermal assumption is related to the velocity dispersion of clouds rather than a microscopic temperature. Effectively we are assuming that the timescale of heating and cooling is far shorter than the dynamical time. Therefore any heating, e.g. due to compression at a shock, is instantaneously radiated away to restore the initial temperature. Sormani et al. (2015a) found that the choice $c_\mathrm{s} \gtrsim 10\,\mathrm{km\,s^{-1}}$ makes the location of the transition from the x_1 to x_2 families of orbits consistent with observations.

The first step to numerically solve an equation such as Equation (2.1) is to discretise it. We divide the region of interest into a grid of discrete cells centered at grid points $\mathbf{x}_i$, and divide the time dimension into a grid of discrete points t_n, with the value of $\mathbf{U}$ within cell i at time t_n labelled as $\mathbf{U}_i^n$.

We now need some way of advancing our solution through time, i.e. given $\mathbf{U}_i^n$ we want to find $\mathbf{U}_i^{n+1}$. The general steps of any hydrodynamic algorithm are: use some interpolation scheme to reconstruct $\mathbf{U}(\mathbf{x})$ from the cell-averaged values $\mathbf{U}_i$, calculate appropriate values for $\mathbf{F}$ and the derivative $\nabla \cdot \mathbf{F}$ using a finite differencing scheme, and then integrate Equation (2.1) to update $\mathbf{U}$.

2.2.1 Shocks

Astrophysical fluid problems present particular challenges to numerical algorithms. These flows are often supersonic and involve large density contrasts. As Roberts (1969) showed with a simplified one dimensional model, even mild spiral forcing by stellar structure can induce strong shocks in the interstellar medium of the galaxy.

Shocks are discontinuities in $\mathbf{U}$. Our algorithm of choice should be able to accurately resolve these discontinuities while still conserving the mass and momenta of our fluid. The principle difficulty comes when computing the fluxes $\mathbf{F}$. Typically one would like to compute the fluxes between cells using the value of $\mathbf{U}$ at the cell edges. As we only track the cell averaged values of $\mathbf{U}$ this requires some form of interpolation. Strong shocks result in large jumps in $\mathbf{U}$ between neighbouring cells, so naive interpolation methods can result in overshooting, and unwanted numerical oscillations in the reconstructed variables. As we shall see, successful algorithms require "slope limiters" that preserve monotonicity of the solution in regions of discontinuities.

The work in this thesis uses two codes for solving Equation 2.1. The first is an implementation of a comparatively simple algorithm, dubbed the second-order flux splitting method, or "FS2", that nonetheless has been shown to work particularly well for the kind of supersonic inviscid flows that we encounter when studying large scale gas flows in galaxies. We use an implementation of FS2 originally written by Prof John Magorrian (Sormani et al., 2015a). The second is PLUTO (Mignone et al., 2007), a highly modular open source fluid solver designed specifically for astrophysical

fluid problems.

2.2.2 The second-order flux splitting method (FS2)

van Albada & Sanders (1982) presented a study of the stability and accuracy of several different fluid solvers when considering a test problem based on the response of gas to the potential of spiral arms in a galaxy. Of the algorithms they considered the most suited to the particular demands of the problem was the second order flux splitting method, or FS2.

We consider a two dimensional inviscid compressible fluid, with an isothermal equation of state $P = c^2\rho$, where c is the sound speed, and P the pressure. In this case we can write

$$\mathbf{U} = \begin{pmatrix} \rho \\ \rho u \\ \rho v \end{pmatrix}, \tag{2.3}$$

where u is the x component of velocity, and v the y component.

For brevity we consider the one dimensional case, so that Equation (2.1) for our simple case reduces to

$$\frac{\partial \mathbf{U}}{\partial t} + \frac{\partial \mathbf{F}}{\partial x} = \mathbf{S}. \tag{2.4}$$

with the flux term

$$\mathbf{F}(\mathbf{U}) = \begin{pmatrix} \rho u \\ \rho(u^2 + c^2) \\ \rho u v \end{pmatrix}. \tag{2.5}$$

This algorithm first makes the convenient simplifying assumption to consider the contributions from the source term and the flux term separately. First the source

term

$$\frac{\partial \mathbf{U}}{\partial t} = \mathbf{S} \tag{2.6}$$

is integrated over half a timestep, and the updated value of $\mathbf{U}$ is used to then integrate

$$\frac{\partial \mathbf{U}}{\partial t} + \frac{\partial \mathbf{F}}{\partial x} = 0 \tag{2.7}$$

over a full time step, followed by the integration of Equation (2.6) again over another half time step, so this is a second order algorithm. This has the advantage that Equation (2.6) can often be integrated analytically.

In FS2 we usually work with the primitive (not conserved) fluid variables

$$\mathbf{Q} = \begin{pmatrix} \rho \\ u \\ v \end{pmatrix}, \tag{2.8}$$

which are assumed to form a piecewise linear distribution within each cell:

$$\mathbf{Q}(x)_i = \mathbf{Q}_i + (x - x_i)\frac{(\delta \mathbf{Q})_i}{\Delta x} \qquad x_{i-1} < x < x_{i+1} \tag{2.9}$$

where x_i is the position of the centre of grid i, Δx is the grid spacing, with

$$(\delta\rho)_i = \rho_i \cdot \mathrm{ave}\Big(2\frac{\rho_{i+1} - \rho_i}{\rho_{i+1} + \rho_i},\, 2\frac{\rho_i - \rho_{i-1}}{\rho_i + \rho_{i-1}}\Big) \tag{2.10}$$

and

$$(\delta q)_i = c \cdot \mathrm{ave}\Big(\frac{q_{i+1} - q_i}{c},\, \frac{q_i - q_{i-1}}{c}\Big) \tag{2.11}$$

where $q \in \{u, v\}$, and c is the sound speed. The function $\mathrm{ave}(a, b)$ is known as the van Albada slope limiter, and tends to the average of a and b when they are close, but tends to the smaller of the two when the difference between them is large. Averaging of

this form prevents central differencing across a shock, which would lead to numerical oscillations, and the formulation of Equation (2.10) ensures that ρ remains positive. The specific function used is

$$\mathrm{ave}(a,b) = \frac{(b^2+\epsilon^2)a + (a^2+\epsilon^2)b}{a^2+b^2+\epsilon^2} \tag{2.12}$$

where ϵ is a small bias of the order of $(\Delta x)^3$ that prevents the clipping of smooth but large gradients. We follow van Albada et al. (1982) and set $\epsilon = 0.008$.

The cell averaged fluid variables are advanced by half a time step to $\mathbf{Q}_i^{n+1/2}$ by integrating Equation (2.6). Then Equation (2.9) is used to calculate the values at the boundaries $\mathbf{Q}^{n+1/2}_{(i\pm1/2)\mp}$, where the subscript $(i+1/2)-$ indicates the value at the negative x side of the boundary at $x_{i+1/2}$, and vice-versa. The boundary values of the primitive variables are then transformed back into the conserved variables $\mathbf{U}$ to calculate the fluxes.

The flux at the cell boundaries is split into a positive flux (in the direction of the flow) $\mathbf{F}^+$ and a negative flux (against the flow) $\mathbf{F}^-$, with

$$\mathbf{F}^+(\mathbf{U}) = \begin{cases} \mathbf{F}(\mathbf{U}) & u \geq c \\ \begin{pmatrix} \frac{\rho}{4c}(u+c)^2 \\ \frac{\rho}{2}(u+c)^2 \\ \frac{\rho}{4c}(u+c)^2 v \end{pmatrix} & |u| < c \\ 0 & u \leq -c \end{cases} \tag{2.13}$$

and $\mathbf{F}^-(\mathbf{U}) = \mathbf{F}(\mathbf{U}) - \mathbf{F}^+(\mathbf{U})$. This expression for the flux has continuous first derivatives. The net flux across the boundary at $x_{i+1/2}$ is then

$$\Phi^{n+1/2}_{i+1/2} = \mathbf{F}^+(\mathbf{U}^{n+1/2}_{(i+1/2)-}) - \mathbf{F}^-(\mathbf{U}^{n+1/2}_{(i-1/2)+}) \tag{2.14}$$

which is used to update the cell centred variables. Finally Equation (2.6) is integrated over half a time step again.

It can be shown that this method is stable to small wavelength perturbations if:

$$\frac{c\Delta t}{\Delta x} \leq \frac{1}{2}, \tag{2.15}$$

where Δt and Δx are the time and grid spacing respectively. This is the Courant-Friedrichs-Lewy (CFL) condition (Courant et al., 1928). Intuitively it can be understood as the condition that the time step is smaller than the amount of time it takes a signal to propagate over a single grid cell.

The upwind differencing used in the reconstruction step and the split flux term mean that this algorithm is particularly suited to the study of problems with strong shocks and supersonic flows, and accurately conserves mass and momentum. It is also transparent and computationally convenient.

2.2.3 PLUTO

The simulations presented in Chapters 4 and 5 were run using PLUTO, a highly modular and flexible fluid code developed specifically to solve astrophysics problems Mignone et al. (2007). Generally speaking, PLUTO integrates the fluid equations by first interpolating the fluid variables at the cell edges, then calculating fluxes at the cell boundaries, and finally updating the fluid variables through a time stepping algorithm, much like FS2. The principal advantage of PLUTO for our use cases is that it is massively parallelisable. This is achieved through domain decomposition, where the computational domain is divided into multiple subregions, each of which is handled by a different processor.

PLUTO allows the user to choose from a wide variety of options for each step. We use a linear reconstruction method with the van Albada slope limiter, equivalent to

Equation (2.9). Once the fluid variables have been interpolated at the cell boundaries, calculating the fluxes requires solving a Reimann problem at each boundary. This is an initial value problem of the form

$$\mathbf{U}(x,t_0) = \begin{cases} \mathbf{U}^+, & \text{for} \quad x > x^+, \\ \\ \mathbf{U}^-, & \text{for} \quad x < x^+. \end{cases} . \tag{2.16}$$

In principle this can be solved exactly. PLUTO has a variety of different solvers for this problem; we use the *tvdlf* option that employs a simple Lax-Friedrichs scheme (Lax, 1954). This method has a relatively high numerical viscosity when compared to some of the other Reimann solvers, but is more stable and robust for the type of problems we consider. To update the solution in time we use the second order Runge-Kutta method (Gottlieb & Shu, 1998). This choice of options provides a good trade off between computational efficiency, numerical stability and accuracy.

2.3 Rigid bar models

Hydrodynamic simulations in rigidly rotating potentials are very commonly used to study the dynamics of gas in the centre of the Milky Way (see e.g. Jenkins & Binney, 1994; Rodriguez-Fernandez & Combes, 2008; Sormani et al., 2015a,c; Li et al., 2016; Ridley et al., 2017; Sormani et al., 2018b). The simulations presented in Chapter 3 are of this type.

In models such as these the gas evolves in an externally applied constant potential. The simulations are typically performed in a frame corotating with the bar with pattern speed Ω_p. In this frame the fluid equations become:

$$\begin{aligned} \partial_t \rho + \nabla \cdot (\rho \mathbf{v}) &= 0 \\ \partial_t \mathbf{v} + (\mathbf{v} \cdot \nabla)\, \mathbf{v} &= -\frac{\nabla P}{\rho} - \nabla \Phi - 2\boldsymbol{\Omega}_\mathrm{p} \times \mathbf{v} + \Omega_\mathrm{p}^2 \mathbf{x}. \end{aligned} \tag{2.17}$$

In Chapter 3 we calculate Φ from a multicomponent analytic model of the density distribution of the Milky Way using a multipole expansion (Binney & Tremaine, 2008).

2.4 N-body modelling

N-body models are extremely powerful tools to study the behaviour and evolution of collisionless systems such as galaxies. They enable us to relax any assumptions about time independence and symmetry of the potential used in rigid bar models. In Chapters 4 and 5 we explore the dynamics of gas in a live N-body potential. The dynamics of an isolated collisonless system is governed by the collisionless Boltzmann equation (CBE)

$$\frac{\partial f}{\partial t} + \mathbf{v} \cdot \nabla f - \nabla \Phi \cdot \frac{\partial f}{\partial \mathbf{v}} = 0 \tag{2.18}$$

where $f = f(\mathbf{x}, \mathbf{v}, t)$ is the distribution function (DF) which describes the phase space density of particles and $\Phi = \Phi(\mathbf{x}, t)$ is the gravitational potential generated by the DF

$$\Phi(\mathbf{x}, t) = -G \int \frac{\rho(\mathbf{x}', t)}{|\mathbf{x} - \mathbf{x}'|} \mathrm{d}^3\mathbf{x}' \tag{2.19}$$

where $\rho(\mathbf{x}, t)$ is the spatial density of particles

$$\rho(\mathbf{x}, t) = \int f(\mathbf{x}, \mathbf{v}, t) \mathrm{d}^3\mathbf{v}. \tag{2.20}$$

The characteristics of the CBE, along which the DF is constant, are given by

$$\frac{\mathrm{d}\mathbf{x}}{\mathrm{d}t} = \mathbf{v} \tag{2.21}$$

$$\frac{\mathrm{d}\mathbf{v}}{\mathrm{d}t} = \mathbf{a} \equiv -\nabla \Phi. \tag{2.22}$$

In other words, they are the ballistic orbits in the gravitational potential given by Equation (2.19). The central principle of N-body modelling is to integrate the CBE along the characteristics, using Monte Carlo sampling to estimate Φ.

2.4.1 GROMMET

In this thesis we use the N-body code GROMMET (Magorrian, 2007). GROMMET is a particle mesh (PM) code (Hockney & Eastwood, 1988; Binney & Tremaine, 2008). To solve for the gravitational potential the basic steps of the PM method are:

1. Use the positions of the N-body particles to estimate the density on an evenly spaced Cartesian grid of points in three dimensions.

2. Solve Poisson's equation for the gravitational potential at each grid point.

3. Calculate the gravitational acceleration at each grid point using finite differencing.

4. Interpolate the accelerations back to the positions of each particle using the same interpolation scheme as (1).

The regularity of the grid points means that efficient Fourier transform techniques can be used to solve for Φ, and as the most computationally intensive steps are the mass assignment and interpolation of the accelerations the cost of PM techniques generally scale linearly with particle number N.

GROMMET uses the cloud-in-cell interpolation method to assign particle masses onto the grid and to interpolate gravitational accelerations at particle positions. In this scheme each particle may be visualised as a homogeneous cube with side length equal to the grid spacing. Each mass element in the cube is then assigned to the nearest grid point. This is a simple algorithm that means that the mass assigned to a particular grid point from one particle varies continuously as the particle moves across

the mesh. Using the same interpolation scheme for the mass assignment and acceleration calculation means that the code respects Newton's third law, and therefore conserves linear momentum.

Once the mass is assigned to the grid, GROMMET uses the method of James (1977) to solve for the gravitational potential at the grid points. First, the potential is found that corresponds to the potential generated by an electric charge density with the same values as the mass density on the grid inside a grounded box (so the potential vanishes at the boundaries). Then Gauss' theorem is used to find the charge density that would be generated on such a bounding box, and the potential corresponding to this charge density is calculated. This potential is subtracted from the original potential to give the gravitational potential generated by the isolated mass distribution. This method is computationally efficient in both time and memory, being roughly twice as fast as the usual procedure of doubling the extent of the mesh (Binney & Tremaine, 2008) and using 1/8 as much memory (Magorrian, 2007).

The spacing of the grid sets the effective softening length of the potential. As a typical galaxy has a strongly concentrated mass distribution GROMMET uses a series of nested grids to improve efficiency. Each grid has the same number of points, but half the extent. This means that the potential in the inner regions, where it is most interesting, is calculated with a far higher resolution than the outer regions. In practice this requires careful book-keeping to ensure that Newton's third law is respected when considering the forces between particles covered by different meshes. The positions of the grids are fixed and must be specified at the beginning of the simulation, making GROMMET well suited to the study of isolated systems but less suited for other problems such as the study of merging galaxies or cosmological simulations.

To move particles along orbits GROMMET uses a standard leapfrog integrator. This is symplectic, time reversible and conserves momentum. The code does contain the option for a more efficient block-timestep scheme, where finer boxes have an

associated shorter time step, but we do not use this option for the sake of simplicity.

To evolve the gas in the live N-body potential we have modified PLUTO to include GROMMET. At each time step we interpolate the gravitational accelerations onto the hydrodynamic grid. We do not include the gas mass in the potential calculation.

2.5 Generating N-body models of barred galaxies

To generate initial conditions for our N-body models we follow the method of McMillan & Dehnen (2007) with some modifications to include the multimass sampling scheme of Sigurdsson et al. (1995) in order to improve resolution in the central regions of the model. The main steps of the process are as follows:

1. Create equilibrium initial conditions for the spherical components (the halo and optional bulge) of the galaxy including the monopole component of the potential of the disc as an external potential.

2. Evolve this N-body initialisation while slowly growing the non-spherical components of the disc potential to allow the particles to fully relax in the presence of the disc.

3. Replace the rigid disc potential with an N-body disc by sampling from the distribution function in the potential of the relaxed non-disc components.

2.5.1 The bulge and halo

For an isotropic system in equilibrium in a time-independent potential Φ, the DF is purely a function of the energy:

$$f = f_0(E). \tag{2.23}$$

The DF is related to the density through an Abel integral equation, which can be inverted (Eddington, 1916) to give

$$f_0(E) = \frac{1}{\sqrt{8}\pi^2}\frac{\mathrm{d}}{\mathrm{d}E}\int_0^E \frac{\mathrm{d}\Phi}{\sqrt{E-\Phi}}\frac{\mathrm{d}\rho}{\mathrm{d}\Phi} \tag{2.24}$$

All of the models in this work use spherical isotropic Hernquist (1990) profiles for the bulge and the halo,

$$\rho(r) = \frac{Ma}{2\pi r(a+r)}, \tag{2.25}$$

where M and a are the total mass and the scale length respectively. We calculate the DF for each component by solving Equation (2.24) including the full spherical potential of the bulge, halo, and monopole of the disc. Including the monopole of the disc in this step prevents the density distributions of each component changing significantly while the full disc potential is introduced in the next step.

Of course, the bulge and halo of the Milky Way are not isotropic. We draw the particles from an isotropic distribution initially, but both the bulge and the inner halo become significantly flattened during the growth of the disc potential (see below). Furthermore, the bulge becomes strongly triaxial during bar formation in the live simulation. As discussed in Chapter 4, the inclusion of a bulge in necessary in the initial conditions to provide a strong enough central concentration of mass to ensure that the potential has an inner-Lindblad resonance, which is important for the formation of a nuclear gas disc supported by x_2 orbits.

We could create equal mass realisations of each component by drawing particles from $f_0(E)$. However, for an equal mass realisation of a Hernquist profile the fraction of particles within a radius r goes as r^2/a^2 for $r \ll a$. For a realistic high resolution model of the Milky Way's halo with $M = 10^{12}\mathrm{M}_\odot$, $a = 30\,\mathrm{kpc}$, and $N = 1 \times 10^6$ this gives only ∼300 halo particles of mass $10^6\mathrm{M}_\odot$ in the inner-most 500 pc of the galaxy. The small number of high mass particles produces an artificially noisy, rapidly varying

potential in the centre of the galaxy where the gas flow is most interesting. To reduce this artificial source of noise we increase the resolution in the centre by drawing particles from the sampling distribution:

$$f_s(E, L) = h(E, L) f_0(E), \tag{2.26}$$

where $f_0(E)$ is the isotropic distribution function and (Sigurdsson et al., 1995)

$$h(E, L) = A \begin{cases} \left(\frac{r_{\rm peri}}{a}\right)^{-\lambda} & \text{if } r_{\rm peri} < a, \\ 1 & \text{otherwise,} \end{cases} \tag{2.27}$$

where $r_{\rm peri}(E, L)$ is the pericentre radius of a particle with energy E and angular momentum L, and A is a normalisation constant. The parameter λ sets the steepness of the increase in sampling near the centre which we set equal to 1. Following this scheme a particle sampled at (E, L) is assigned the mass $Mf_0(E)/Nf_s(E, L)$ so that the increase in particle number density near the centre is balanced by a reduction in particle mass.

We then evolve the spherical components using GROMMET whilst adiabatically growing the non-spherical part of the disc potential. In practice this means that we evolve the particles in the externally applied potential

$$\Phi(t) = \Phi_0 + A(t)(\Phi_{\rm full} - \Phi_0) \tag{2.28}$$

where Φ_0 is the monopole of the disc potential, $\Phi_{\rm full}$ is the full disc potential. The growth of the non-spherical component of the potential is controlled by $A(t)$, which varies smoothly from $A(0) = 0$ to $A(T_{\rm grow}) = 1$. We then let the particles fully relax in the new potential for another period $T_{\rm grow}$, which is set to a value several times larger than the dynamical time in the region of the disc.

2.5.2 The disc

While creating the initial conditions of the disc of our models we proceed under the approximation that we can completely decouple the planar and vertical motion of each disc particle. We sample disc particles from the DF of McMillan & Dehnen (2007)

$$f_{\rm disc}(E_\parallel, E_\perp, L_z) = \frac{\Omega(R_{E_\parallel})\tilde{\Sigma}(R_{E_\parallel})}{(2\pi)^{3/2}\kappa(R_{E_\parallel})}\frac{1}{z_d\,\sigma_z(R_{E_\parallel})}\exp\left[-\frac{E_\perp}{\sigma_z^2(R_{E_\parallel})}\right] \times \frac{1}{\tilde{\sigma}_R^2(R_{E_\parallel})}\exp\left[-\frac{\Omega(R_{E_\parallel})[L_z - L_c(R_{E_\parallel})]}{\tilde{\sigma}_R^2(R_{E_\parallel})}\right], \tag{2.29}$$

where $E_\parallel$ and $E_\perp$ are the planar and vertical components of total energy respectively, L_z is the z-component of angular momentum, $R_{E_\parallel}$ is the radius of the circular orbit with energy $E_\parallel$, $\Omega(R)$ and $\kappa(R)$ are the angular and radial epicyclic frequency respectively, $L_c(R)$ is the angular momentum of a circular orbit at radius R, $\sigma_z(R)$ is the vertical velocity dispersion and $\tilde{\Sigma}(R)$ and $\tilde{\sigma_R}(R)$ are chosen such that the surface density and radial velocity dispersion of the sampled particles are close to the desired target profiles $\Sigma(R)$ and $\sigma_R(R)$.

The DF given by Equation (2.29) was originally proposed by Dehnen (1999b). It follows from the argument that warming of a stellar disc by secular processes can be described by an exponential in radial action and vertical energy, where radial action is approximated by $\omega_R J_R \sim \Omega(E)[L_c(E) - |L|]$ (Dehnen, 1999a).

We omit several steps in the original method of McMillan & Dehnen (2007) that were designed to reduce noise in the initial conditions of the disc by more regularly sampling phase space. This noise seeds the formation of a bar, and we are trying to produce barred N-body models. In practice our sampling procedure is as follows:

1. Set $\tilde{\Sigma} = \Sigma$ and $\tilde{\sigma}_R = \sigma_R$.

2. Draw a radius R from the surface density $\tilde{\Sigma}(R)$ and set $E_\parallel$ to the energy of a

circular orbit at R.

3. Draw a number $\xi \in (0,1)$ and set $L_z = \ln(\xi)\tilde{\sigma}_R^2(R)/\Omega(R)$. If $|L_z| > L_c(R)$ restart from Step (2).

4. Integrate the orbit with these values of $E_\parallel$ and L_z for one radial period T_R and tabulate $R(t)$ and $\dot{R}(t)$. Draw $t \in (0, T_R)$ and $\phi \in (0, 2\pi)$ and set $R = R(t)$, $\dot{R} = \dot{R}(t)$, $\phi = \phi$, and $\dot{\phi} = L_z/R(t)$.

5. Repeat (2) to (4) until the desired number of disc particles have been sampled.

6. Evaluate the actual surface density and radial-velocity dispersion produced by this procedure $\Sigma_{\rm out}$ and $\sigma_{{\rm out},R}$ and iteratively adapt

$$\tilde{\Sigma}(R) \to \tilde{\Sigma}(R)\frac{\Sigma(R)}{\Sigma_{\rm out}(R)}, \quad \tilde{\sigma}_R(R) \to \tilde{\sigma}_R(R)\frac{\sigma_R(R)}{\sigma_{{\rm out},R}(R)}. \tag{2.30}$$

7. Iterate steps (2) to (6) until $\Sigma(R)$ and $\sigma_R(R)$ are reproduced to within the desired degree of accuracy.

8. Sample the vertical position of each particle from an exponential profile $z \in \exp(-|z|/z_d)$ and draw v_z from a Gaussian distribution with variance σ_z^2.

In practice $\tilde{\Sigma}$ and $\tilde{\sigma_R}$ converge after approximately 5 iterations, and we use a total of 10 steps in this work.

The distribution function leaves the choice of Σ and σ_R free. We model the disc with a double exponential profile

$$\rho_d(R,z) = \frac{M_d}{4\pi R_d^2 z_d}\exp\left[-\frac{R}{R_d} - \frac{|z|}{z_d}\right], \tag{2.31}$$

so that $\Sigma(R) \propto \exp(-R/R_d)$. We set $\sigma_R(R)$ such that Toomre's Q (Toomre, 1964)

$$Q = \frac{\sigma_R \kappa}{3.36 G \Sigma} \tag{2.32}$$

is constant with radius. We calculate κ from the full potential including the contributions from the bulge and halo, and for all simulations in this work we set $Q = 1.0$ everywhere in the disc, to ensure the quick formation of a strong bar.

We have carried out a number of simple tests of the various steps of this method, including testing the stability of the initial spherical components without the disc, testing the stability of an isolated high-Q disk in an externally applied rigid halo potential, and testing a complete compound model while suppressing bar or spiral instabilities by randomising the azimuth of each disc particle after every timestep (McMillan & Dehnen, 2007), confirming that the method produces a close-to equilibrium realisation of a full compound galaxy with the desired properties. This iterative DF approach has several advantages over other methods: It avoids the non-equilibrium effects of moment based methods such as Hernquist (1993) that assume a locally Maxwellian velocity distribution, it allows the precise control of the density distributions of each component compared to methods that use a fully DF based approach, such as Kuijken & Dubinski (1995), and it is computationally cheaper than fully iterative methods such as Yurin & Springel (2014).

As a final step we half the mass of each particle and include the mirror distribution of all particles with $\mathbf{x}$ and $\mathbf{v}$ reflected through the origin. This ensures that the centre of mass of the system remains stationary.

2.5.3 Gas

We set up the gaseous component in our simulations in an initially axisymmetric configuration. All the gas is initially on circular, planar orbits. We set the midplane gas density to a constant value, and solve for the the vertical density profile assuming that the gas is in hydrostatic equilibrium. Therefore the vertical density satisfies

$$c_s^2 \frac{\partial \rho}{\partial z} = -\rho \frac{\partial \Phi}{\partial z} \tag{2.33}$$

which is solved by

$$\rho(R,z) = \rho(R,0)\exp\left[-\frac{\Phi(R,z)-\Phi(R,0)}{c_s^2}\right]. \tag{2.34}$$

Assuming $v_R = v_z = 0$ the circular velocity of the gas is then given by

$$\frac{v_c^2}{R} = \frac{\partial\Phi}{\partial R} + c_s^2\frac{1}{\rho}\frac{\partial\rho}{\partial R} \tag{2.35}$$

In practice the last term in this equation is always negligible compared to the first, so we do not include it when calculating the initial velocities of the gas.

Chapter 3

A Dynamical Model of the Central Molecular Zone of the Milky Way

3.1 Introduction

The molecular gas of the Milky Way is strongly concentrated towards the centre. The central molecular zone (CMZ), the $\sim 500\,\mathrm{pc}$ region around the Galactic center, contains around 10% of the total molecular gas budget of the Galaxy (Ferrière et al., 2007). Astronomers are interested in the CMZ for a multitude of reasons. It offers an excellent laboratory for the study of star formation in an extreme environment (Longmore et al., 2013a). Gas is also an excellent dynamical tracer. It is well established that the centre of the Milky Way contains a bar, and that the rotating non-axisymmetric potential of the bar strongly affects the gas flow in the inner-most few kpc. Surveys have observed the CMZ in a variety of molecular emission lines (e.g. Bally et al., 1988; Dame et al., 2001; Henshaw et al., 2016a). Emission from the Galactic centre is extremely complex, with elongated features spanning several degrees, multiple molecular cloud complexes, and a high degree of asymmetry.

This Chapter has been published as Ridley et al. (2017).

This chapter will present a simple two-dimensional isothermal simulation of gas in a realistic rigid model of the Galactic potential. We will show how we can use this model to interpret the pattern of emission from the Galactic center. We identify the CMZ as a central disc of gas closely following x_2 orbits, containing two nuclear spiral arms, and show that this can explain many features of the distribution and kinematics of gas in the CMZ. Nuclear spirals are commonly observed in external barred spiral galaxies (e.g. Schinnerer et al., 2002; Martini et al., 2003a,b; Kuno et al., 2008; van de Ven & Fathi, 2010). It would therefore be natural to also find them in the centre of our Galaxy. They arise commonly in hydrodynamic simulations in barred potentials (e.g. Ann & Thakur, 2005; Li et al., 2015), thus they are automatically consistent with the large scale flow in and around the bar. If indeed nuclear spirals are present in the centre of the MW, the density enhancement along the spiral arms would result in ridges of emission spanning the width of the CMZ similar to those observed in the (l, b, v) data cubes. The compression produced by the spiral shocks would provide a natural mechanism for the formation of complex molecular species.

The presence of nuclear spiral arms at the centre of the MW has been discussed for some time. Sofue (1995) used a purely kinematic spiral arm model to deproject the (l, v) distribution of emission in the CMZ to produce a face-on map. Sawada et al. (2004) compared emission and absorption maps to derive distances of clouds along lines-of-sight without the use of kinematic models, and the resulting face-on map was consistent with the presence of two arms of gas in the central region. However, neither of these was a dynamical model derived from physical principles. Our aim here is to improve on previous work by producing a fully dynamic model of the CMZ consistent with the gas flow in the entire central region of the Galaxy. As we describe below, our picture differs in several significant ways from previous works and corrects some inconsistencies of the spiral arm interpretation of Sofue (1995) and Sawada et al. (2004) as discussed in Henshaw et al. (2016b).

This chapter is adapted from Ridley et al. (2017), and is structured as follows. In Section 3.2 we discuss the data used in this chapter, and highlight particular features of interest. In Section 3.3 we describe the numerical scheme and the potential used to run the hydrodynamical simulation. The results of the model are described in Section 3.4, and we discuss the successes and shortcomings of the model in Section 3.5. Finally in Section 3.6 we summarise our conclusions.

3.2 Data

Here we briefly describe some characteristics of some high resolution observations of the CMZ. This section should serve as a reference for the remainder of the chapter.

We focus on NH_3 (1,1) emission in the region $-1^\circ \leq l \leq 3.5^\circ$, using data from the H_2O Southern Galactic Plane Survey (HOPS; Walsh et al. 2011, Purcell et al. 2012). The data have a spatial resolution of ~ 60 arcsec and a spectral resolution of $2\,\mathrm{km\,s^{-1}}$, and have been fit using the Semi-automated multi-COmponent Universal Spectral-line fitting Engine (SCOUSE [1]; Henshaw et al. 2016b). These data and the fits are discussed in detail in Longmore et al. (2017).

Although NH_3 shows some signs of self-absorption in the CMZ, the distribution and kinematics of emission show the same large scale features as observed in CO (Rodriguez-Fernandez et al., 2006), HNCO (Henshaw et al., 2016b) and CII (Langer et al., 2017). In this work we focus mainly on coherent features in the (l, b, v) data cube, and not on the precise details of the emission.

Fig. 3.1 shows the (l, v) and (l, b) projections of the SCOUSE fits to the data. We note several structures of particular interest, highlighted in Fig. 3.2:

1. Blue points: Arm I, an extended ridge of emission running from $l = -0.7^\circ$, $v = 100\,\mathrm{km\,s^{-1}}$ to $l = 0.7^\circ$, $v = -50\ \mathrm{km\,s^{-1}}$.

[1] https://github.com/jdhenshaw/SCOUSE

2. Red points: Arm II, another ridge of emission running parallel to Arm I from $l = -0.7°$, $v = 70\,\mathrm{km\,s^{-1}}$ to $l = 0.7°$, $v = -150\,\mathrm{km\,s^{-1}}$. Sofue (1995) identified Arms I and II as two spiral arms within the CMZ, however Kruijssen et al. (2015) proposed that they are the projection of gas clouds on an open ballistic orbit.

3. Magenta points: Arm III, also known as the "polar arc". A high velocity feature at a large inclination, suggested as a continuation of Arm II by Sofue (1995)

4. Green points: Sgr B2 cloud complex and the dust ridge. The Sgr B2 cloud is a well studied molecular cloud complex around $(l, b, v) \simeq (0.7°, 0.1°, 10 - 70\,\mathrm{km\,s^{-1}})$. An unusually high number of independent velocity components are present at each (l, b) pixel (Henshaw et al., 2016b), and the velocity dispersions are also unusually broad. Suggested explanation for this complex velocity structure include a shell-like arrangement produced by supernovae or the result of a collision between two molecular clouds (e.g. Henshaw et al., 2016b, and references therein). Between Sgr B2 and G0.253+0.016 (the "Brick", rightmost black square) lies a prominent ridge of dust emission containing several molecular clouds. See section 3.5.1 for a more in depth discussion.

5. Pink points: 1.3° cloud complex, a huge molecular cloud structure suggested by Rodriguez-Fernandez et al. (2006) as the site of accretion onto the CMZ.

6. Black points: Clump 2, a molecular cloud complex at $(l, b, v) \simeq (3°, 0.2°, 20 - 150\,\mathrm{km\,s^{-1}})$. As Stark & Bania (1986) suggested, the incredibly high internal velocity dispersion and high bulk velocity make it extremely likely that this is the signature of a dust lane or spiral arm.

7. Cyan points: Cloud M of Rodriguez-Fernandez et al. (2006), possibly associated with the far side dust lane.

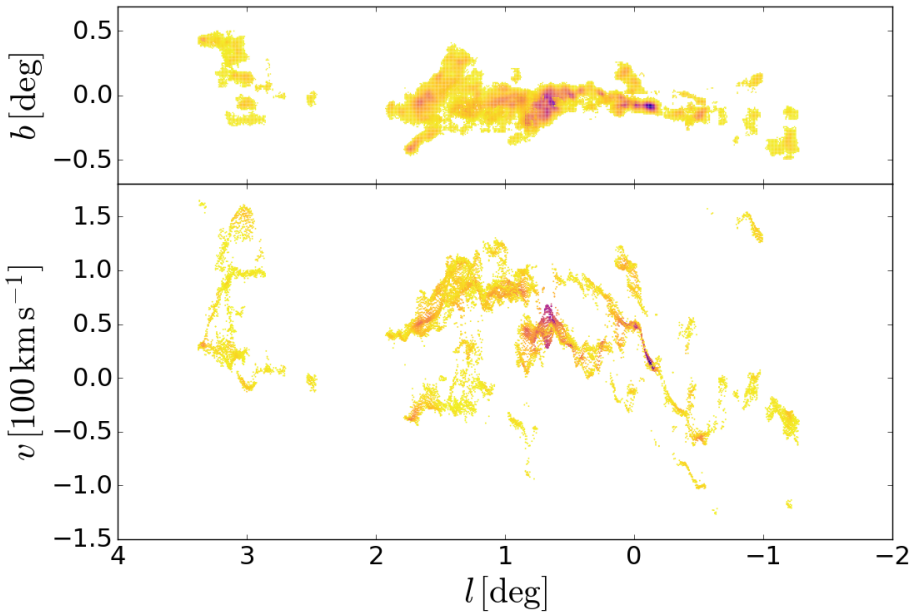

Figure 3.1: NH_3 $(1-1)$ data from the HOPS survey (Purcell et al., 2012), fit with the SCOUSE algorithm (Henshaw et al., 2016b). Top panel: The spatial distribution of emission in (l, b). Bottom panel: The position velocity distribution in (l, v). Each point represents a spectral component as determined by the SCOUSE algorithm, coloured by brightness temperature (arbitrary units).

Also shown in the same figure are locations of some prominent molecular clouds. The black triangles are the 20 km s^{-1} and 50 km s^{-1} clouds, two bright clouds located near to Sgr A* in projection, believed to be connected to Arm II. The black plus is Sgr C, a star forming molecular cloud complex at the tip of Arm II, multiple line-of-sight velocity components. For a more complete discussion, see for example Rodriguez-Fernandez et al. (2006); Henshaw et al. (2016b).

3.3 Methods

3.3.1 The potential

Our model uses an externally applied rigidly rotating potential, as discussed in Section 2.3. We use a realistic MW potential that is the sum of 4 components: bar, bulge, disc, halo. As a starting point we use the best fitting potential of McMillan (2017).

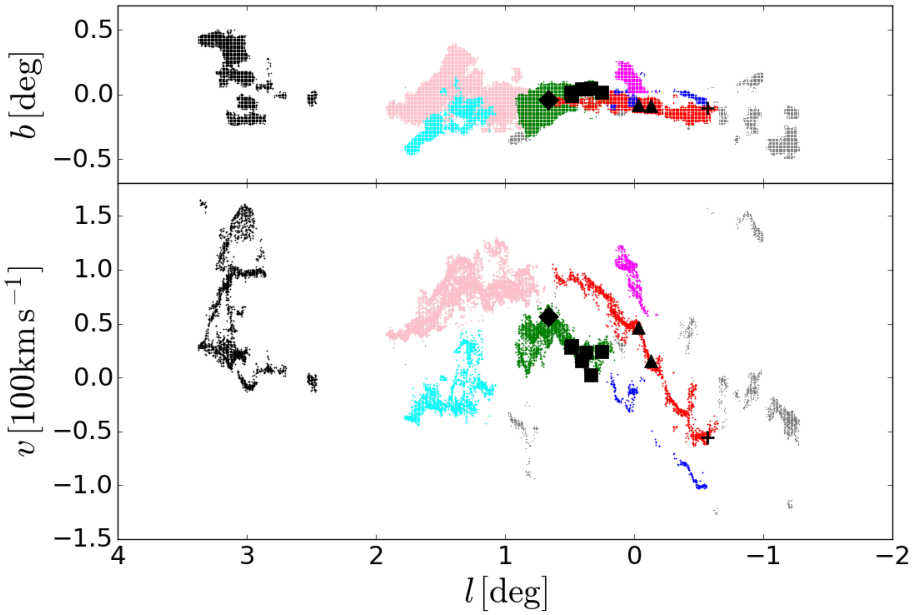

Figure 3.2: The data of Fig. 3.1, with features of interest highlighted in various colors. **Blue points**: Arm I. **Red points**: Arm II. **Magenta points**: Arm III, also known as the "polar arc". **Green points and black diamond**: Sgr B2 cloud complex and the dust ridge. **Pink points**: 1.3° cloud complex. **Black points**: Clump 2 of Stark & Bania (1986). **Cyan points**: Cloud complex M of Rodriguez-Fernandez et al. (2006). **Black triangles**: the 20 and 50 $\mathrm{km\,s^{-1}}$ clouds. **Black plus**: Sgr C. **Black squares:** From left to right dust ridge clouds B to F and G0.253+0.016, also known as "the Brick".

This is an axisymmetric model, and therefore cannot accurately represent the central region of the Galaxy, which is dominated by a rotating stellar bar. As we focus on this region, and in particular on the effects of the bar, we perform the following modifications:

1. We add a barred component. This is chosen such that its quadrupole fits the best fitting quadrupole in Sormani et al. (2015c).

2. We modify the inner bulge density profile to make it more centrally concentrated, so that the potential has an Inner Lindblad Resonance (ILR) which is required for the x_2 orbit family to exist as these are believed to provide the backbone for the CMZ.

3. We adjust the parameters of the other components to compensate for the introduction of the barred component. This means that we slightly decrease the mass of the disc and the halo in order to compensate for the extra mass introduced by the bar, in such a way that the circular velocity at the Sun position remains approximately constant.

We can expand the potential in the plane of the Galaxy in multipoles as follows:

$$\Phi(R,\phi) = \Phi_0(R) + \sum_{m=1}^{\infty} \Phi_m(R)\cos\left(m\phi\right), \tag{3.1}$$

where $\{R,\phi,z\}$ denote planar polar coordinates. As the bar is perfectly bisymmetric and aligned with the x-axis all sine terms in the expansion are zero.

Fig. 3.3 shows the circular velocity curve of the potential and the contributions from each component separately. Our definition of "circular velocity curve" is based on the axisymmetric part of the potential:

$$V_c(R) \equiv \sqrt{R\frac{\mathrm{d}\Phi_0}{\mathrm{d}R}}. \tag{3.2}$$

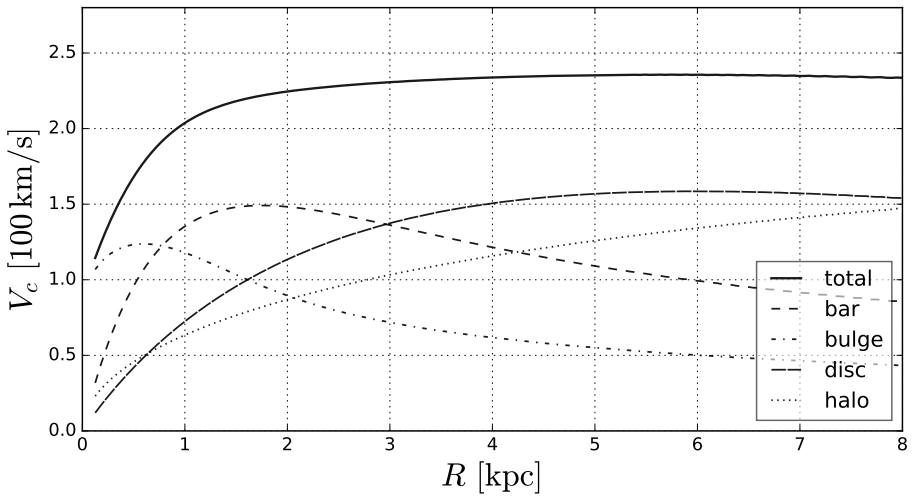

Figure 3.3: The full curve shows the circular velocity curve for the potential used in this chapter. The separate contributions from bulge, disc and halo are shown with dot-dashed, dashed and dotted lines respectively.

Since the gas undergoes strong non-circular motions in the region dominated by the bar, which for our Galaxy corresponds approximately to the region within Galactocentric radius $R = 3\,\mathrm{kpc}$ (e.g. Binney & Merrifield, 1998), the "circular velocity speed" can be significantly different from the speed of the gas obtained in simulations, or observed in the Galaxy, at the same radii (e.g. Binney et al., 1991, SBM15a).

Fig. 3.4 shows the quadrupole and the octupole of the potential used in this chapter. These are generated by the bar, which is the only non-axisymmetric component in our potential.

The details of each component of the potential are as follows.

Bulge. This component is generated by the following density distribution:

$$\rho_{\mathrm{b}} = \frac{\rho_{\mathrm{b0}}}{(a/a_0)^{\alpha}} \exp\left[-\left(a/a_{\mathrm{cut}}\right)^2\right] \tag{3.3}$$

where

$$a = \sqrt{x^2 + y^2 + \frac{z^2}{q_{\mathrm{b}}^2}}. \tag{3.4}$$

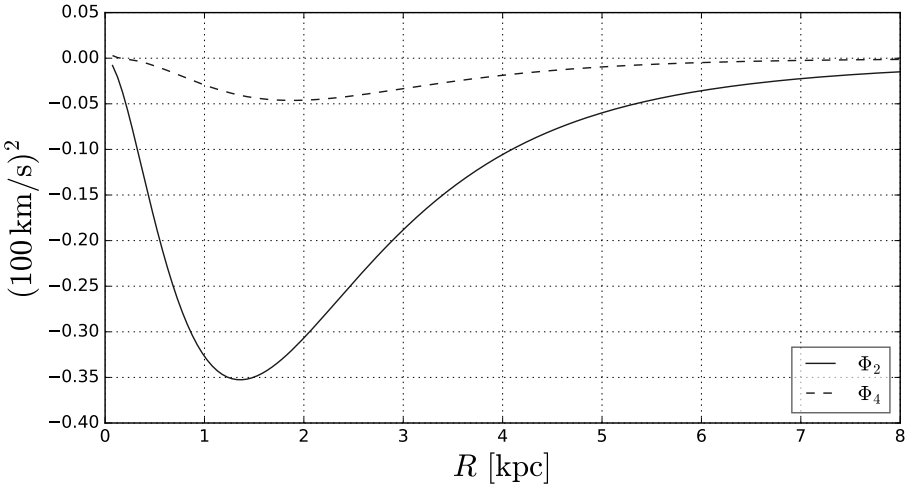

Figure 3.4: The quadrupole Φ_2 and octupole Φ_4 of the potential used in this chapter. The non-axisymmetric components of the potential are all entirely generated by the bar, given by Equation 3.5.

We use the following values for the parameters: $\alpha = 1.7$, $\rho_{\mathrm{b0}} = 0.8 M_\odot\,\mathrm{pc}^{-3}$, $a_{\mathrm{cut}} = 1.0\,\mathrm{kpc}$, $q_{\mathrm{b}} = 0.5$, and without loss of generality we arbitrarily set $a_0 = 1.0\,\mathrm{kpc}$. The value $\alpha = 1.7$ for the inner slope ($R \lesssim 500\,\mathrm{pc}$) of the density distribution is consistent with near-infrared photometry (e.g. Bissantz & Gerhard, 2002; Launhardt et al., 2002). We cut the bulge at $a_{\mathrm{cut}} = 1.0\,\mathrm{kpc}$ as we assume that beyond this radius the bar dominates over the bulge.

Bar. The density of the bar is taken to be:

$$\rho_{\mathrm{B}} = \rho_{\mathrm{B0}} \exp\left(-a/a_{\mathrm{B}}\right), \tag{3.5}$$

where

$$a = \sqrt{x^2 + \frac{y^2 + z^2}{q_{\mathrm{B}}^2}}, \tag{3.6}$$

with the following values for the parameters: $\rho_{\mathrm{B0}} = 5 M_\odot\,\mathrm{pc}^{-3}$, $a_{\mathrm{B}} = 0.75\,\mathrm{kpc}$ and $q_{\mathrm{B}} = 0.5$. The bar is also assumed to rotate with constant pattern speed of $\Omega_{\mathrm{p}} = 40\,\mathrm{km\,s^{-1}\,kpc^{-1}}$. This places the Inner Lindblad Resonance at $R_{\mathrm{ILR}} = 1.2\,\mathrm{kpc}$ and

the corotation resonance at $R_{\rm CR} = 5\,{\rm kpc}$. The form of the bar density distribution is chosen to be exponential as infrared photometry has found the Milky Way bar density profile to be roughly exponential (Wegg & Gerhard, 2013). The parameters, including the pattern speed, have been chosen such that the quadrupole of the bar matches the best fit quadrupole of Sormani et al. (2015c). This bar is perfectly prolate and cylindrical, the bar of the real MW has a boxy component with a significant vertical extent, but as we entirely interested in the in-plane component of the potential this is unimportant.

Disc. We assume that the disc is the sum of a thick and a thin disc (Gilmore & Reid, 1983). The density distribution is:

$$\rho_{\rm d} = \frac{\Sigma_1}{2z_1} \exp\left(-\frac{|z|}{z_1} - \frac{R}{R_{\rm d1}}\right) + \frac{\Sigma_2}{2z_2} \exp\left(-\frac{|z|}{z_2} - \frac{R}{R_{\rm d2}}\right), \tag{3.7}$$

where $\Sigma_1 = 850 M_\odot\,{\rm kpc}^{-2}$, $R_{\rm d1} = 2.5\,{\rm kpc}$, $z_1 = 0.3\,{\rm kpc}$, $\Sigma_2 = 174 M_\odot\,{\rm kpc}^{-2}$, $R_{\rm d2} = 3.02\,{\rm kpc}$, $z_2 = 0.9\,{\rm kpc}$. These parameters are slight modifications of the parameters of McMillan (2017).

Halo. This is a simple Navarro et al. (1996) profile. The density distribution is:

$$\rho_{\rm h} = \frac{\rho_{\rm h0}}{x(1+x)^2} \tag{3.8}$$

where $x = r/r_h$, $\rho_{\rm h0} = 0.00811 M_\odot\,{\rm pc}^{-3}$, and $r_h = 19.6\,{\rm kpc}$. This is a slight modification of the best fit model of McMillan (2017).

Figure 3.5 compares our stellar mass model of the central region of the MW with results of Launhardt et al. (2002) derived from infrared photometry. We find that our model agrees well with the data. We do not explicitly include the potential due to the central black hole Sgr A* in our simulations as it has no effect on the gas flow

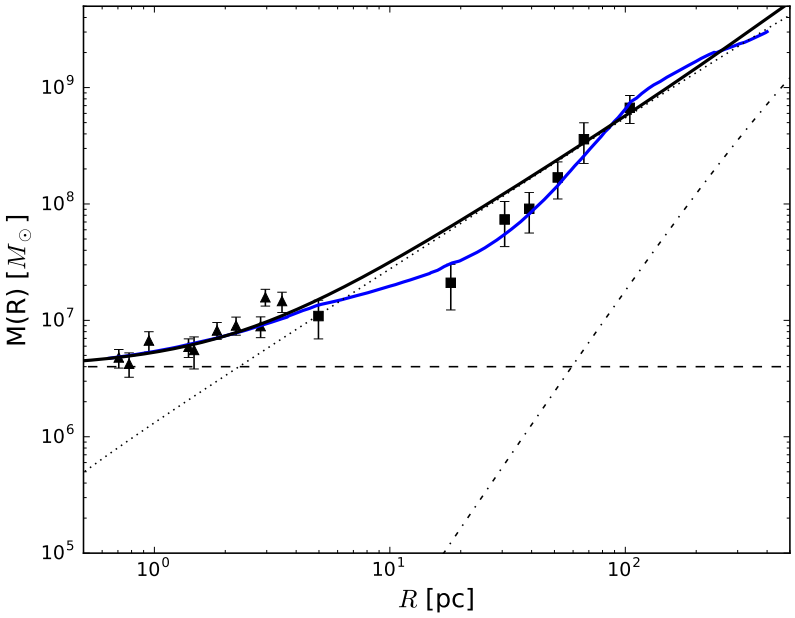

Figure 3.5: Enclosed mass within spheres of radius R for our model, compared to dynamic and photometric estimates for the Milky Way. **Dashed line:** A central black hole of mass $4 \times 10^6 M_\odot$. **Dotted line:** The bulge. **Dash-dotted line:** The bar. **Solid black line:** The sum of all three components. **Solid triangles:** McGinn et al. (1989). **Solid squares:** Lindqvist et al. (1992). **Solid blue line:** the total enclosed mass form Launhardt et al. (2002), see their figure 14.

at the scales we consider here.

3.3.2 Numerical scheme

As discussed in Section 2.2.2 we solve the fluid equations using an Eulerian code based on the second-order flux-splitting scheme developed by van Albada et al. (1982) and later used by Athanassoula (1992), Weiner & Sellwood (1999) and others (e.g. Sormani et al., 2015a,b,c) to study gas dynamics in barred potentials.

In the following simulations, we assume that the gas is a two-dimensional inviscid isothermal fluid governed by the Euler equations. The gas is not self-gravitating and flows in the externally imposed barred potential of Section 3.3.1 above.

The CMZ of the MW has a thickness of 15-30 pc and a radius of ∼200 pc (Ferrière et al., 2007). As the vertical extent of the gas is so much smaller that the radial extent, our 2D model should be able to capture the important points of the gas flow. We will explicitly test this assumption in the following chapter.

An additional term is introduced in the continuity equation to implement the recycling law of Athanassoula (1992). The recycling law was originally meant to take into account the effects of star formation and stellar mass loss in a simple way. In practice, the only effect of the recycling law is to prevent too much gas from accumulating in the very centre and to replace gas lost at the boundary due to the outflow boundary conditions. It does not affect the morphology of the results, so our results do not change if we disable the recycling law. The dynamical equations in an inertial frame are

$$\begin{aligned} \partial_t \rho + \nabla \cdot (\rho \mathbf{v}) &= \alpha_{\mathrm{r}} (\rho_0^2 - \rho^2), \\ \partial_t \mathbf{v} + (\mathbf{v} \cdot \nabla)\, \mathbf{v} &= -\frac{\nabla P}{\rho} - \nabla \Phi, \\ P &= c_{\mathrm{s}}^2 \rho, \end{aligned} \tag{3.9}$$

where ρ is the surface density of the gas, P is the pressure, Φ is the gravitational potential, $\mathbf{v}$ is the velocity, c_s is the sound speed, α_r is a constant representing the efficiency of the recycling law and ρ_0 is the initial surface density. We adopt recycling efficiency $\alpha_\mathrm{r} = 0.3\,M_\odot\,\mathrm{pc}^{-2}\,\mathrm{Gyr}^{-1}$ and initial density $\rho_0 = 1\,M_\odot\,\mathrm{pc}^{-2}$ (Athanassoula, 1992), and use an isothermal sound speed of $c_\mathrm{s} = 10\,\mathrm{km\,s}^{-1}$

Our grid is 1750×1750 cells on a side. The resolution is $\mathrm{d}x = 5\,\mathrm{pc}$, so the total simulated area is a square with side 8.75 kpc. We start with gas in equilibrium on circular orbits in an axisymmetrised potential and turn on the non-axisymmetric part of the potential gradually during the first 150 Myr to avoid transients. The orbital timescale at $R = 1\,\mathrm{kpc}$ is $\sim 15\,\mathrm{Myr}$ in our potential, so this amounts to 10 orbital times. We have verified that increasing this timescale does not influence our final results. We use outflow boundary conditions: gas can freely escape the simulated region, after which it is lost forever. The potential well is sufficiently deep, however, to prevent excessive quantities of material from escaping. The grid does not fully enclose the corotation resonance, however we have verified with lower resolution simulations that this has no effect on the final state of the gas flow. The most important factor for the grid extent is whether it fully encloses the dust lane shocks.

To project material to the (l, v) plane, we assume an angle $\phi = 20°$ between the Sun-GC line and the bar major axis (the x-axis of the simulation), consistent with current estimates (e.g. Bland-Hawthorn & Gerhard, 2016), and a Sun-GC distance of $R_0 = 8\,\mathrm{kpc}$.

3.4 Gas dynamics

3.4.1 Large-scale gas flow

Figure 3.6 shows the surface density of the hydro simulation at $t = 280\,\mathrm{Myr}$. At this time the gas flow has reached an approximate steady state. Far from the centre,

outside $R \sim 1$kpc, the gas closely follows closed orbits belonging to the x_1 family, which are highly elongated along the major axis of the bar. The gas slowly drifts inwards along this sequence of orbits as collisional processes dissipate energy until, close to the Inner Lindblad Resonance, the "cusped" x_1 orbit is reached. At this point, the gas cannot continue to follow the x_1 orbits because they become self-intersecting. The gas piles up at these cusps, and two almost straight shocks form from gas plunging almost radially from the tips of the x_1 orbits towards the CMZ, where it settles on the less-extended, more circular x_2 orbits, forming a central disc. Sormani et al. (2015a) present a thorough and more general study of the dynamics of gas in barred potentials.

This gas flow can explain many features of observations of the inner Galaxy, such as the high terminal velocities of the gas, internal features seen in (l, v) plots, and the concentration of molecular gas within a "parallelogram"-like shape in the (l, v) plane, see e.g. Fux 1999; Sormani et al. 2015c; Li et al. 2016. Our model of the CMZ is therefore embedded in a consistent gas flow that can reproduce features of the whole barred region, and not just of the CMZ. Accretion of gas onto the CMZ occurs naturally as a result of the simulation.

A hydrodynamic simulation such as the one described above can become unstable at a sufficiently high resolution. This is commonly observed in simulations of this type (e.g. Kim et al., 2012, SBM15a), and is believed to be a real physical phenomenon, dubbed the "wiggle instability" (Wada & Koda, 2004; Kim et al., 2014; Sormani et al., 2017). We will discuss this further in Section 3.5.2. Nonetheless the large-scale features of the flow remain approximately constant over time.

3.4.2 Nuclear spirals

Nuclear spirals are evident in the inner region ($R \lesssim 500\,\mathrm{pc}$) in Fig. 3.6, with the outer end of each spiral arm connected to the inner end of each shock. We propose

below that some of the streams observed in the data are associated with these nuclear spiral arms.

These spirals are kinematic density waves, caused by the constructive interference of excursions of the gas about the x_2 orbits, see Wada (1994); Sormani et al. (2015b). The streamlines of the gas do not flow along the spiral arms, but through them, and crowding of the streamlines leads to the formation of density enhancements. Gas is compressed as it enters the spiral arm, and decompresses as flows away. In the real Galaxy this compression may trigger gravitational collapse, in which case the gravitationally bound clump of gas would remain compressed as it left the spiral arm and continued to flow around the CMZ following an approximately ballistic orbit. Even though our simulations neglect self-gravity, this form of behaviour is still observed due to the wiggle instability (see Section 3.5.2). This causes the spiral shocks to fragment into distinct clumps, and these clumps continue around the CMZ until they collide into the other shock.

The precise morphology of the nuclear disc and spiral arms is affected by the resolution and sound speed of the simulation (SBM15a). This dependency is complex. Both the resolution and the sound speed affect the location at which the shocks form, and hence the location at which gas is fed onto the CMZ. They also affect the dynamics within the CMZ, such as the stability of the flow (see Section 3.5.2). We set the resolution and the sound speed to reasonable values in our model in order to focus on discussing how nuclear spirals, if indeed present in the Milky Way, would appear in observations and affect the dynamics of gas within the CMZ.

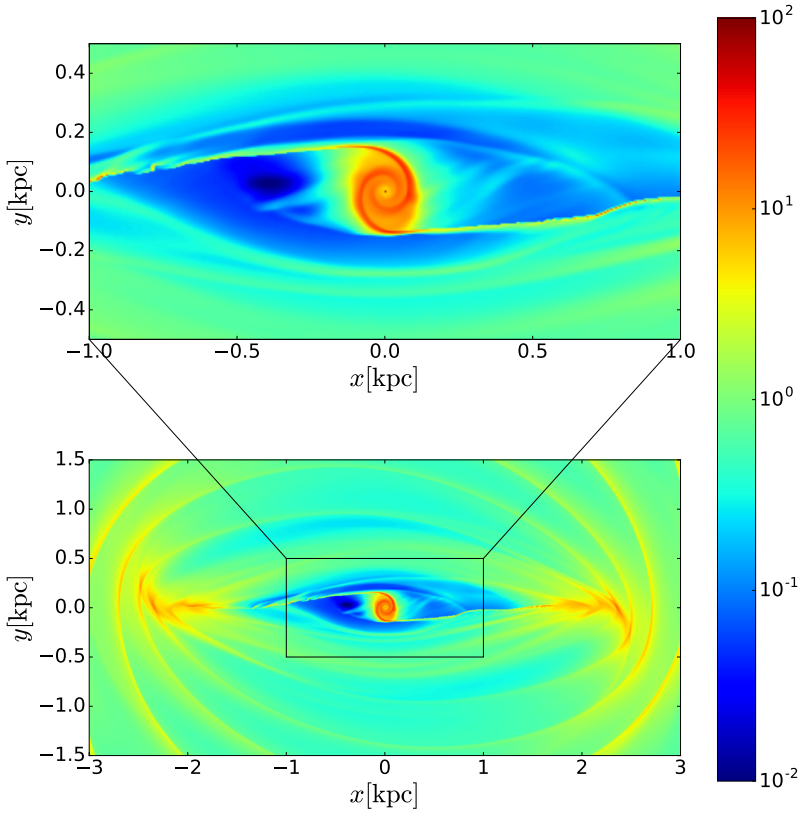

Figure 3.6: Bottom: the fluid density of the simulation at 280Myr, after the flow has reached an approximate steady state. Top: a closer view of the central region of the simulation. The colorbar is in units of $M_\odot\,\mathrm{pc}^{-2}$.

3.5 Discussion

3.5.1 Interpretation of (l, v) features and face-on map of the CMZ

Using our model of the gas flow we can understand the features previously identified in the data. Figure 3.7 shows a close up view of the central region of the simulation, with several features of the flow highlighted. In red and blue are the outer parts of the near-side and far-side spiral arms respectively, and in green is the positive-latitude shock connecting the tip of the cusped x_1 orbit to the x_2 disc. The bottom panel shows the projection of these features in the (l, v) plane. Also shown is the NH_3 data for comparison.

3.5.1.1 Arms I and II

In the longitude-velocity plane, the two spiral arms produce two parallel ridges of emission reaching from positive latitude and velocity to negative latitude and velocity (red and blue in the bottom panel of Fig. 3.7). Moving outwards-in along the red (blue) arm in the top panel of Fig. 3.7, the corresponding trace in the bottom panel is from negative (positive) longitude and velocities to positive (negative) longitude and velocities. As the tangent point between the line of sight and the spiral arm is approached, approximately where the red and blue colours end in Fig. 3.7, the direction of movement in the (l, v) plane is reversed and we go back again towards negative (positive) longitudes.

The two parallel ridges in the bottom panel of Fig. 3.7 have a similar range in longitude and a similar slope to Arm I and II in Fig. 3.2. Thus we identify Arm II (I) as the projections of the near (far) side nuclear spiral arm. These two features were identified with two spiral arms also in the interpretation of Sofue (1995). However, in the interpretation of this author the two arms were swapped in the (l, v) plane: they

identified the Arm I (II) as the projections of the near (far) side nuclear spiral arm, the opposite of our interpretation. This difference allows us to correct an inconsistency of the spiral arms of Sofue (1995) pointed out by Henshaw et al. (2016b) regarding the placements on the $20\,\mathrm{km\,s^{-1}}$ and $50\,\mathrm{km\,s^{-1}}$ clouds (see Section 3.5.3 below).

We interpret Arm III (the"Polar Arc") as a spur of gas extending from Arm II (as proposed in Binney et al. 1991), however we note that this simplified 2D model cannot explain its position at high inclination.

3.5.1.2 1.3° cloud complexes

Figure 3.8 shows a face-on view of the CMZ, together with streamlines of the gas flow. These streamlines do not follow the spiral arms, but go through it at an angle. A dense gas cloud, formed for example as a consequence of compression in the arm, can leave the spiral arm and continue its course along a streamline. This would eventually collide with material on the positive-longitude shock, at a position that depends on where it is ejected from the spiral arm. We would expect such collisions to create cloud complexes with complicated spatial and velocity structure (Henshaw et al., 2016a).

We have observed this happening in our simulations: the gas fragments due to the wiggle instability, and the fragments tend to leave the spiral arms by following the streamlines and collide with material entering the other arm. Similar behaviour is seen in the simulations of Dobbs et al. (2008) or Smith et al. (2014) who model the dynamics of the ISM and molecular cloud formation during spiral arm passage on large galactic scales. In the real ISM, a cloud could form also by other means, for example as a consequence of becoming quasi self-gravitating after compression. However, we do not include self-gravity in the present work.

These collisions would also throw material out of the plane of the CMZ. Observations do indeed suggest that the extent in latitude is greater at the left and right

edges of the CMZ (top panel of Fig. 3.2).

Thus we interpret the 1.3° cloud complex as the result of cloud-cloud collisions between the end of the dust-lane shock and the inner disc, and Sgr B2 as material that has detached from the red arm (discussed further below). In this interpretation, the observed complicated velocity structures and unusually large vertical extent of the gas (see cyan and pink in the top panel of Fig. 3.2) are created by collisions (as also interpreted by Bally et al. 2010).

3.5.1.3 Placement of prominent molecular clouds

An understanding of the history of the environment of a star forming molecular cloud would give insight into the physical processes that can trigger and regulate star formation. Several gas clouds in the CMZ have been identified as the possible progenitors of star clusters (Longmore et al., 2013b), the locations of these prominent cloud complexes within the CMZ are therefore of particular interest because they represent an excellent opportunity to study star formation in extreme conditions (Kruijssen et al., 2014).

Using the steady-state velocity field of the gas flow any (l, v) point can be deprojected to one or more (x, y) positions: in practice there will often be two or more points along a line of sight with the same line of sight velocity, so additional information is required to map a given point in (l, v) space to the (x, y) plane.

The Brick (Lis & Menten, 1998; Longmore et al., 2012; Rathborne et al., 2015) and the $20\,\mathrm{km\,s^{-1}}$ and $50\,\mathrm{km\,s^{-1}}$ clouds (Molinari et al., 2011) have been detected in absorption at IR wavelengths, which suggests that they lie in front of the GC. In addition, Reid et al. (2009) measured both the parallax and proper motion of water masers in Sgr B2, placing it at 130 ± 6pc in front of the GC with $(\mu_l, \mu_b) = (2.3 \pm 1.0, -1.4 \pm 1.0)\,\mathrm{mas\,yr^{-1}}$. These data break the degeneracy of our model, allowing us to place these clouds within the CMZ.

Plotted in Figure 3.8 are the position of some prominent molecular clouds in our interpretation. The 20 and 50 $\mathrm{km\,s^{-1}}$ clouds, with Sgr C, lie along the near side spiral arm, in front of the GC.

As noted by Kruijssen et al. (2015), the Sgr B2, the dust ridge, and the Brick seem to form a continuous structure in (l, b, v) space. This region of emission (the green points in Fig. 3.2) is complex, with multiple components, and it is tempting to identify this structure as the continuation of Arm I. However, this would place the clouds behind the GC, while the data suggest the opposite. Therefore we interpret this region of emission as the superposition of two distinct physical regions in the Galaxy that happen to be at the same location in the (l, v) projections: Arm I behind the GC, and a spur of material detaching from Arm II on the near side, containing the Brick, dust ridge clouds, and Sgr B2.

This is also consistent with the observations that Sgr B2 is host to a high rate of star formation. The compression created by cloud cloud collisions would provide a natural mechanisms for triggering gravitational collapse and star formation.

These interpretations should be taken with a grain of salt. It is tempting to connect Sgr B2 and the Brick with Arm I, the far side arm. The presence of the Brick in absorption together with the observed parallax and proper motion of Sgr B2 would go against this interpretation. However, this relies on the assumption that we know the infrared emission patterns within the CMZ, and clouds in front of the GC show absorption and clouds behind the GC are obscured. While these assumptions are plausible there is always the possibility that they are incorrect, and that the geometry of the CMZ is different to what we have described here. Further observations of the kinematics of molecular clouds in the CMZ are needed to fully understand the three-dimensional distribution of the gas in the centre of the Galaxy.

3.5.1.4 Summary

As shown in Figure 3.7 we interpret:

1. Arm II (I) as the projections of the near (far) side nuclear spiral arms.
2. Sgr B2, the dust ridge, and the Brick cloud as a spur of material detaching from the red arm, the end of which (Sgr B2) is colliding with shocked material reaching the inner disc.
3. The 1.3° cloud complex on one side and the area surrounding Sgr C on the other side as the two sites where the shocks feed the two spiral arms.
4. The polar arm as a spur of material detaching from the red arm (at a further out location than Sgr B2).
5. The $20\,\mathrm{km\,s^{-1}}$, $50\,\mathrm{km\,s^{-1}}$ and Sgr C clouds as condensations along the near side spiral arm.

This model is intended to provide a framework for interpreting the gas flow in the CMZ rather than a detailed fit to all individual observational features. Our interpretation is the result of simulations that were intended to describe the larger-scale flow pattern in the Galactic bar that were not fine-tuned to model the CMZ, so some discrepancies are to be expected. Further efforts in fitting such models to observations may hopefully simultaneously improve our understanding of the inner Galactic potential and provide further insight into observations of the CMZ.

3.5.2 Unsteady flow in the CMZ

Simulations of gas flow in barred potentials are known to be susceptible to a phenomena dubbed the "wiggle" instability. This causes the shocks to periodically develop vortices along their length, break apart, and reform. This results in an unsteadiness

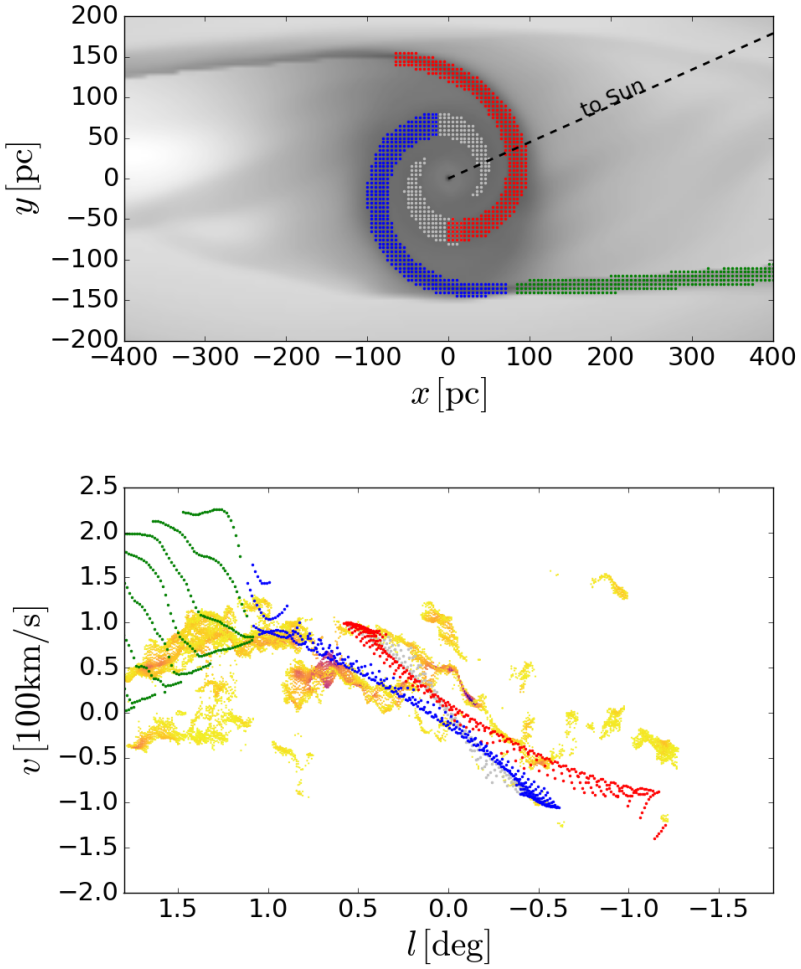

Figure 3.7: Top panel: The near and far side nuclear spiral arms and the positive latitude shock are highlighted in red, blue and green respectively. The inner regions of both arms are also highlighted in gray. Dashed line: The Sun-GC line for our assumed viewing angle of $\phi = 20°$. Bottom panel: Projection of the highlighted features to the (l, v) plane, plotted with the data of Fig. 3.1.

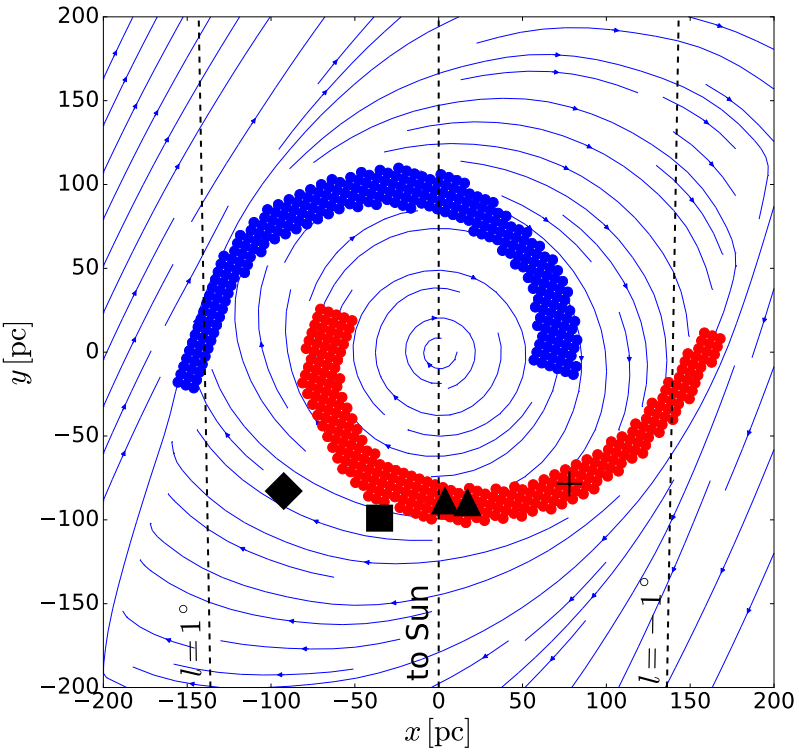

Figure 3.8: A face-on schematic view of the model of the CMZ. The figure has been rotated so that the Sun is at $(x, y) = (0, -8)$. The near and far side spiral arms are shown in red and blue respectively. Streamlines of the gas flow are shown. The black symbols denote the locations of prominent molecular clouds, as in Fig. 3.2. From left to right: Sgr B2 (black diamond), G0.253+0.016, also known as "the brick" (square), the 20 km s^{-1} and 50 km s^{-1} clouds (triangles), Sgr C (plus).

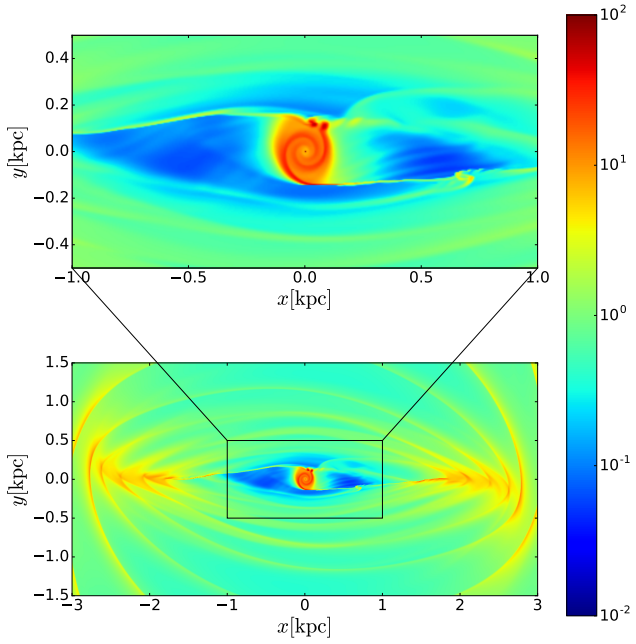

Figure 3.9: Bottom: The fluid density of the simulation at the earlier point of 207 Myr. The flow has reached an approximate steady state, but shows several signs of unsteadiness. Top: A closer view of the central region of the simulation. The colorbar is in units of $M_\odot\,\mathrm{pc}^{-2}$.

in the central gas flow. It is observed across a wide variety of fluid codes (e.g. Kim et al., 2012; Fragkoudi et al., 2016, SBM15a). Kim et al. (2014) and Sormani et al. (2017) have presented theoretical arguments that this instability arises from the periodic nature of the shocks seen in these simulations. This periodicity quickly amplifies any inhomogeneity in the flow or deformation of the shock front.

Our model is mostly stable. However, there are a few signatures of the wiggle instability in the flow. Figure 3.10 shows the gas density at $t = 207\,\mathrm{Myr}$ in the simulation. The flow in the inner region shows some signs of unsteadiness. Most significantly, a bead of material has formed along the positive longitude shock, and two clumps of material have formed along the near-side spiral arm. The features are highlighted (in black and pink respectively), in Figure 3.10, along with their counterparts in the (l, v) plane.

The two pink "clumps" are formed as a consequence of the wiggle instability.

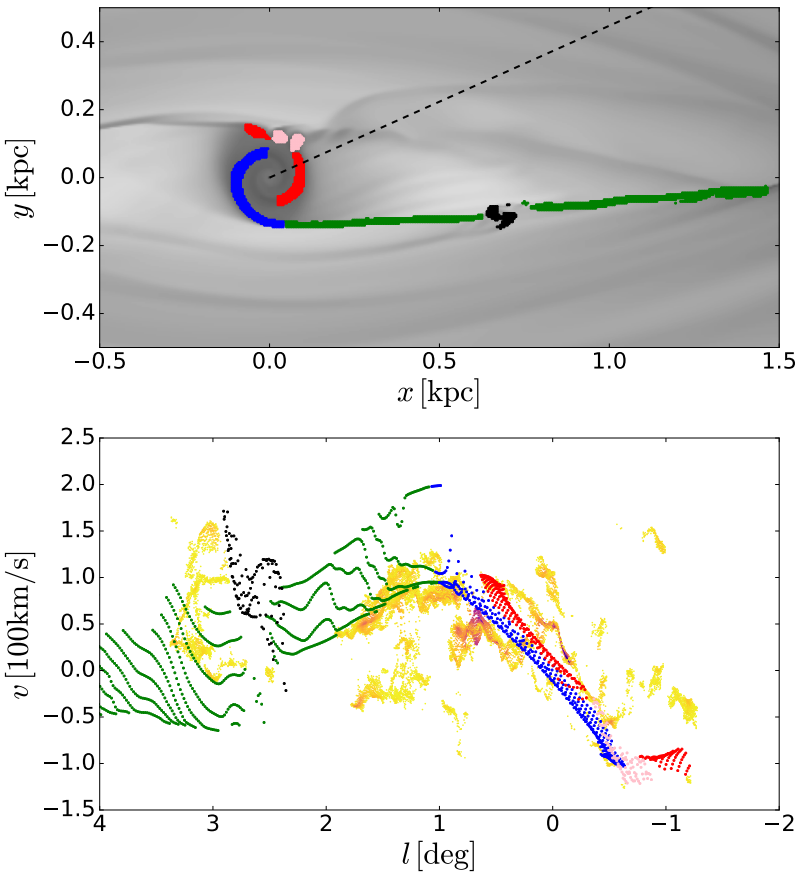

Figure 3.10: The same as Fig. 3.7, for the earlier point of the simulation with two additional features of the flow highlighted: Black points: a "bead" of material on the positive latitude shock. Pink points: Two clumps of material along the near-side spiral arm. Both are signatures of the wiggle instability.

Dense material belonging to the pink region is seen detaching from the spiral arms and later colliding with material on the blue arm, close to the point where it is fed by the green shock, as in our interpretation of the Sgr B2 and 1.3° cloud complexes in Section 3.5.1.2.

It is particularly tempting to associate the signature of the black "bead" along the shock in Figure 3.10 with the Clump 2 cloud complex. They are almost coincident in (l, v) space, and have a similar velocity structure. We therefore interpret the Clump 2 cloud complex as material that is in the process of transitioning from the x_1 to the x_2 orbits, part way down the shock, as originally suggested by Stark & Bania (1986).

These results suggest that the wiggle instability may be responsible for at least three other important facts related to the CMZ.

1. Approximately three-quarters of the molecular emission from $|l| \lesssim 4°$ comes from positive longitudes (e.g. Bally et al., 1988; Burton et al., 1992). In particular, we note that Arm II is far weaker in emission than Arm I, and there appears to be no counterpart to the Sgr B2 and 1.3° cloud complexes at negative latitudes. The asymmetry is too big to be attributed solely to a perspective effect from an inclined bar (Jenkins & Binney, 1994). The wiggle provides a natural mechanism that breaks the symmetric nature of the gas flow.

2. The star formation rate in the CMZ is lower by a factor of $\simeq 10$ than expected from current theories of star formation. Kruijssen et al. (2014) argue that turbulence is the likely cause for this anomaly (see also Bertram et al., 2015). The wiggle instability may also be an important source of turbulence in the CMZ.

3. Henshaw et al. (2016a) recently reported the detection of "corrugations" in a stream of gas within the CMZ, which they identify as gas streaming towards molecular cloud condensations seeded by gravitational instabilities. However, if

the spiral shocks are being deformed by the wiggle instability, this would also produce an oscillation in the (l, v) structure very similar to observations.

3.5.3 Comparison with previous work

The presence of spiral arms at the centre of the MW has been discussed for some time. However, ours is the first dynamical model that takes the larger scale Galactic bar into account consistently, and differs from previous models in several significant ways.

The model of Sofue (1995) is purely kinematic. They assumed that gas flows parallel to the spiral arm. As we have already emphasised, the gas streamlines in our model does not flow along the spiral, but rather through it, and the spiral overdensity is created by crowding of these streamlines. Clouds that form as a result of compression in the spiral arm would detach from the arm shortly after. This is also a key difference between our model and the open stream model of Kruijssen et al. (2015). In the latter, the observed streams in (l, v) plane are produced by gas flowing along a single open ballistic orbit, and therefore one could try to identify a temporal sequence as the gas evolves along the orbit (an hypotheses suggested by Longmore et al., 2013b). Whether a temporal sequence could be identified is less straightforward in our model, especially on timescales longer than a fraction of the dynamical time needed to cover an x_2 orbit.

Another difference between ours and the model of Sofue (1995) is that the two arms are swapped in the (l, v) plane: they identified the near Arm II (I) as the projections of the near (far) side nuclear spiral arm, the opposite of our interpretation.

The spiral arm model as suggested by Sofue (1995) and Sawada et al. (2004) was reconsidered by Henshaw et al. (2016b), but it was discounted in favour of the open stream model of Kruijssen et al. (2015). This was primarily because the configuration of arms that was considered placed the $20\,\mathrm{km\,s^{-1}}$ and $50\,\mathrm{km\,s^{-1}}$ clouds on the far side

of the GC, and as these clouds are seen in absorption (Molinari et al., 2011) they are most probably on the near side. The model we present here corrects this inconsistency, as the $20\,\mathrm{km\,s^{-1}}$ and $50\,\mathrm{km\,s^{-1}}$ clouds are connected to Arm I, which we place on the near side of the CMZ (the red points in Fig. 3.7).

Kruijssen et al. (2015) have argued that observations suggest that Arm II and the Sgr B2 and 1.3° cloud complexes are unconnected, separate features (see the red circle in their fig. 2 and the discussion in their section 2.3). In our model this is indeed the case, as they correspond to projections of physically distinct parts of the gas flow. In contrast, they were connected in the model of Molinari et al. (2011).

Using an unbarred, axisymmetric potential based on the density profile of Launhardt et al. (2002), Kruijssen et al. (2015) showed that if one assumes that the coherent gas streams in the CMZ all lie along a single ballistic orbit, then an orbit can be found that fits the observed (l, b, v) distributions of the streams well. Given the freedom that such a model affords, it is perhaps unsurprising that such an orbit can be found, and their model fails to explain how gas from the larger-scale flow might end up on such an orbit. Our model was not originally intended to provide a fit to the CMZ data, but instead was constructed to match the larger scale flow pattern in the Galactic bar. It automatically accounts for the inflow of shocked gas into the CMZ, and the effect of the non-axisymmetric potential of the bar, both of which are likely to have important consequences on the characteristics of the gas dynamics in the CMZ.

The main weakness of our model is that the projections of the spiral arms are at lower velocities than their observational counterparts. In particular, the near-side arm (red in Fig. 3.2) would need to be at higher line-of-sight velocities to fully match the observations. However, we note again that our model is not tuned to fit the CMZ. The potential is a relatively simple multi-component model of the Galaxy, in which the quadrupole was chosen to fit several completely different large scale features of

the Galactic (l, v) diagram rather than the CMZ (Sormani et al., 2015c). It is thus remarkable how closely the model reproduces the majority of the observed features in the CMZ, although features in our simulation and those in the data do not line up perfectly.

There are several other factors which may affect gas flow in the CMZ not considered here, primarily magnetic fields and stellar feedback. Crocker et al. (2010) found a lower limit of 50 μG for the magnetic field on 400 pc scales near the Galactic Centre, however Kruijssen et al. (2014) argued that, assuming equipartition, gas densities in the CMZ are above the critical density at which turbulent pressure dominates over magnetic pressure. They also argue that the observed star formation rate in the CMZ is too low for stellar feedback to overcome turbulent pressure. Therefore, following previous work, we assume that the dominating factor driving gas flow on the scales considered here is the response to the gravitational potential.

3.5.4 Follow-up work

The asymmetry of emission in the CMZ is a long standing problem. Recently Sormani et al. (2018b) revisited this topic by performing high resolution simulations with the moving-mesh code AREPO, including a live chemical network that tracked the chemistry of the ISM in the simulations. The equations also included realistic heating and cooling terms. The simulations were performed in the same galactic potential as used in this work. The gas in the simulations was affected by thermal instability of Field (1965), forming a two phase medium of cold clumps of molecular gas embedded a warmer diffuse atomic component. The periodic formation and destruction of shocks in the central region due to the wiggle instability led to the intermittent and stochastic production of molecular gas in the CMZ. This resulted in a strong asymmetry in the distribution of gas across the central few degrees, comparable to the asymmetry observed in the real CMZ, providing convincing evidence that the wiggle instability

plays a role in the asymmetry.

3.6 Conclusion

In this chapter we have shown that several features present in (l, b, v) data cubes of molecular emission from the CMZ can be reproduced by nuclear spiral arms arising from gas flow in a barred potential. We have presented a simple hydrodynamical model of isothermal gas moving in an externally imposed barred potential, which was designed to reproduce features of the gas flow on a much larger scale. In the simulation, a central disc of gas on x_2 orbits develops, containing two spiral arms. The disc is connected to the outer regions of the simulation by two shocks.

The model provides a very natural explanation for the structure of the CMZ. Nuclear spirals are common in external galaxies, arise frequently in simulations and are consistent with the larger scale flow in and around the bar.

Although our model is not tuned to the CMZ, it does nevertheless successfully reproduce many aspects of the data. We have shown that the ridges and clouds seen in the data can be understood as the projection of the spiral arms and the shocks to the (l, v) plane. In particular:

1. The two spiral arms produce two parallel ridges in the (l, v) plot, running diagonally from positive (l, v) to negative (l, v).

2. In the region where, in our interpretation, the shock connects to the x_2 disc, cloud-cloud collisions are expected, both between material detaching from the spiral arms and between material running down the shock into the nuclear disc. Large cloud complexes with complex line-of-sight velocity structure, such as Sgr B2 and 1.3°, are examples of the result of such collisions from material detaching from the red arm and shocked material reaching the inner disc.

3. It is possible for cloudlets and spurs of material to detach from the spiral arms as a consequence of the fact that streamlines have a component of the velocity perpendicular to the spiral arms. We interpret the polar arm and the dust ridge as an example of such a spur.

4. A bead of material moving down the positive-latitude shock would produce a vertical emission feature at positive l, disconnected from the CMZ, similar to Bania Clump 2.

5. The compression produced by spiral shocks in the CMZ provides a natural mechanism for producing the densities and pressure necessary for the production of the molecular species that we observe in the region.

The wiggle instability, often seen in simulations of gas flow in barred potentials, may provide a natural explanation for two important CMZ facts:

1. The observed asymmetry of emission. Some particular signatures of unsteady flow are present in both the simulation and the data.

2. The low star formation rate observed in the CMZ. The wiggle instability would provide the source of turbulence needed to suppress star formation.

This topic has been investigated by Sormani et al. (2018b) using simulations that track the chemistry of the ISM, confirming that the wiggle instability can naturally account for the asymmetry of the CMZ.

The features of the model presented here are a qualitatively good match to the data, but there are a number of discrepancies, notably the too small line of sight velocities produced by nuclear spirals in the (l, v) plane. The model is by no means a "best fit", and has been chosen to show that a simple gas flow model in a realistic potential can provide a useful and physically appealing interpretation of the features observed in the CMZ.

The simulations of this chapter neglect much of the physics of the ISM. In modelling the gas as a single phase isothermal medium we have assumed that the microphysics of the gas; the heating, cooling and chemical reactions are unimportant on the scales we consider when compared to the response to the gravitational potential. We have also assumed we can ignore any time dependence and asymmetry in the galactic potential. The first assumption has been tested by Sormani et al. (2018b). The work of the next chapter will address this last assumption.

Chapter 4

Gas Flow in Live N-body Potentials

4.1 Introduction

In the previous chapter we have assumed that the gravitational potential of the Galaxy can be well modelled as rigidly rotating, bisymmetric, and constant in time. This is a convenient simplification, and has been very commonly used (e.g. Jenkins & Binney, 1994; Rodriguez-Fernandez & Combes, 2008; Sormani et al., 2015a,b,c; Li et al., 2016). Hydrodynamic models that use a rigid potential have been very successful in explaining observations of gas flow in the centre of the Galaxy and have been used to constrain some parameters of the bar, particularly the pattern speed (Sormani et al., 2015c; Li et al., 2016). As our understanding of the galactic potential continues to evolve, it is important to understand the limitations of the assumptions that such models make. If fluctuations in the central galactic potential are strong enough to disturb the gas out of equilibrium then gas flow models in rigid potentials will be of limited usefulness. Alternatively, if these effects can safely be ignored, then rigid gas flow models are a promising tool with which to constrain the galactic potential.

The most obvious and realistic way of modelling a time dependent gravitational potential is with an N-body model. To date the most relevant and complete study on the dynamics of gas in N-body bars is the work of Fux (1999). He performed SPH simulations in self-consistent Milky Way-like N-body simulations with N between $\sim 5 \times 10^5$ and $\sim 3.5 \times 10^6$, and used the results to interpret features in (l, v) data from the bar region. The gas flow in these simulations was very asymmetric, and never reached a steady state. This was primarily because the centre of mass of the stellar bar decoupled from the centre of mass of the system, and wandered around with a displacement of several hundred parsecs. This would indeed suggest that the asymmetry and time dependence of the Galactic potential are important when considering the centre of the Galaxy, and that rigid models have limited applicability. However the polar grid used to calculate the gravitational potential in the simulations may have been responsible for amplifying this off-centering (Pfenniger & Friedli, 1993), thus over exaggerating the fluctuations in the potential.

In this chapter we use high resolution N-body simulations with a gaseous component to study the dependence of the gas flow on the time dependence and asymmetry of a realistic barred potential. We begin with a carefully constructed axisymmetric multicomponent galaxy model, including a stellar disc, bulge and dark halo. This model is evolved using a particle mesh N-body code explicitly designed to conserve linear momentum. Once a strong bar has formed in the simulation, the gaseous component is allowed to evolve for several dynamical times in the live potential of the N-body simulation. We do not include the self gravity of the gas; it evolves purely in the gravitational potential of the N-body component. We examine the unsteadiness of the gas, and compare it to the gas flow in a rigid potentials designed that closely match the potential of the N-body simulation. Finally we examine whether it is possible to determine parameters of the N-body potential by fitting equilibrium gas flow models to mock observations of the more realistic simulations.

This chapter is structured as follows: Section 4.2 discusses the numerical scheme used to run the simulation, the choice of initial conditions, the time evolution, and the final state of the N-body potential. In Section 4.3 we examine the gas flow in the live simulation. In Section 4.4 gas flow in the live N-body potential is compared to simulations in various rigid potentials. In Section 4.5 examine the consequences of varying parameters of our rigid models, and attempt to fit an analytic bar model to the N-body potential by matching hydrodynamical simulations to mock observations of the live simulation. Finally Section 4.7 sums up.

4.2 Our reference N-body model

The choice of codes used to run these simulations is important for several reasons. Many N-body codes do not respect Newton's third law, and hence do not conserve momentum, which can lead to artificial instabilities such as exaggerated bar-halo wandering (Pfenniger & Friedli, 1993). To evolve the N-body component of the simulations we use GROMMET, (Magorrian, 2007), a fast and efficient particle-mesh code that conserves linear momentum to within machine precision. To solve the hydrodynamical equations we use PLUTO, a grid based astrophysical fluid solver with many different physics options Mignone et al. (2007). See Chapter 2 for a detailed discussion of the numerical methods of this chapter.

To evolve the gas in the live N-body potential we have modified PLUTO to incorporate GROMMET. In general the CFL condition regulating the minimum hydrodynamic time step (Section 2.2) is a tighter constraint than the minimum time step needed for the N-body component, so we evolve the N-body component once every 10 hydrodynamic time steps. For the hydrodynamic component the grid cell size $\Delta x = 20\,\mathrm{pc}$, $\Delta t = 1 \times 10^{-1}\,\mathrm{km\,s^{-1}\,kpc^{-1}} \simeq 10^4$ yr.

After constructing the initial conditions, the N-body model is evolved without

gas for 2 Gyr. We do not include the gas initially because of the high computational cost of the hydrodynamic component, and because we are primarily interested in the response of the gas to the bar, which takes several dynamical times to form. The gaseous component is released after 2 Gyr and reaches an approximately steady state after 1 bar rotation, $\sim 160 - 200$ Myr. We evolve the gas for 400 Myr in total.

During construction of the initial conditions for our N-body models we sample the bulge, halo and disc DFs separately, and then stitch each component together to form the galaxy model. In the discussion below, whenever we refer to a "bulge/halo/disc" particle, we mean a particle that was initially created by sampling from the DF of the respective component.

4.2.1 Initial conditions

Parameter	Value	Description
M_t	$1.43 \times 10^{12}\mathrm{M}_\odot$	Total mass
$M_\star$	$5.43 \times 10^{10}\mathrm{M}_\odot$	Total baryonic mass
M_h	$1.37 \times 10^{12}\mathrm{M}_\odot$	Halo mass
a_h	$37.8\,\mathrm{kpc}$	Halo scale length
M_b	$5 \times 10^{9}\mathrm{M}_\odot$	Bulge mass
a_b	$200\,\mathrm{pc}$	Bulge scale length
M_d	$4.93 \times 10^{10}\mathrm{M}_\odot$	Disc mass
Σ_d	$1.25 \times 10^{10}\mathrm{M}_\odot\,\mathrm{kpc}^{-2}$	Central disc surface density
R_d	$2.5\,\mathrm{kpc}$	Disc scale length
z_d	$300\,\mathrm{pc}$	Disc scale height
Q	1.0	Toomre's Q
N_t	2×10^6	Total number of particles
N_h	8×10^5	Number of halo particles
N_b	4×10^5	Number of bulge particles
N_d	8×10^5	Number of disc particles

Table 4.1: Parameters of the reference model.

Bar formation in N-body simulations is inherently chaotic, and as such it is impossible to predict or control the final state of a model given the initial conditions (Sellwood & Debattista, 2009). Hence in this chapter we do not attempt to create

a perfect model of the Milky Way. Instead this model is designed to be a useful analogue with which to probe the relevant physics.

To generate initial conditions for the N-body components we follow the method of McMillan & Dehnen (2007) with some modifications following the multimass sampling scheme of Sigurdsson et al. (1995) to improve resolution in the central regions of the model. The method is discussed in detail in Section 2.5, but to recap the main steps of the process are:

1. Create equilibrium initial conditions for the spherical components (the halo and bulge) of the galaxy from the spherical DF including the monopole component of the potential of the disc as an external potential.

2. Evolve this N-body initialisation while slowly growing the non-spherical components of the disc potential to allow the particles to fully relax in the presence of the disc.

3. Replace the rigid disc potential with a live N-body disc by sampling from the disc DF in the potential of the relaxed non-disc components.

This method is flexible and generates an N-body initialisation that is very close to collisionless equilibrium. For a full discussion of the numerical methods used in this chapter see Chapter 2.

The model is initially axisymmetric, and contains a bulge, disc, and halo. We base our initial conditions primarily on the best fitting model of McMillan (2017). The bulge and halo initially follow a Hernquist profile, with density given by

$$\rho(r) = \frac{Ma}{2\pi r(a+r)}. \tag{4.1}$$

McMillan (2017) did not use this density profile for either the bulge or halo. We use a Hernquist model for the bulge for computational convenience. We expect this profile

will change quite significantly due to the growth of the bar. We use a Hernquist profile for the halo because it provides a good match to the NFW profile used by McMillan (2017) at small radii ($< 20\,\mathrm{kpc}$) but has fewer particles on unintersting loosely bound orbits. We have chosen the parameters of the halo such that the inner density profile matches the inner density profile of the best fit NFW model of McMillan (2017).

The disc is modelled with a double exponential profile with density

$$\rho(R,z) = \frac{\Sigma_d}{2z_d} \exp\Big\{ -\frac{R}{R_d} - \frac{|z|}{z_d} \Big\} \tag{4.2}$$

The parameters of the model are summarised in Table 4.1. The total and stellar mass are that of McMillan (2017), as are the structural parameters of the disc, however the mass of the bulge has been increased and the scale length decreased to ensure that the model has an ILR and therefore that x_2 orbits exist in the potential, and the disk mass has been slightly decreased to account for this.

The model is initially perfectly point-symmetric, i.e. we include the mirror distribution of particles created by reflecting both $\mathbf{r}$ and $\mathbf{v}$ through the origin, so that both the centre of mass and total momentum of the entire model are 0 to within machine precision.

The recipe that we follow for constructing the initial conditions allows for a free choice of the radial velocity dispersion $\sigma_R(R)$ for the disc particles, which we chose such that Toomre's $Q = \frac{\sigma_R \kappa}{3.36 G \Sigma} = 1.0$ everywhere in the disc. This is a highly unstable value, and ensures that a strong bar forms quickly in the model to reduce the total computational time needed for the simulation.

We should note that this model differs from the MW in several important ways. Primarily it has a reasonably high mass, concentrated bulge to ensure that the final central density is high enough for the gas to form an x_2 disc, as we observe in the Milky Way. Too shallow a central density profile results in a completely different

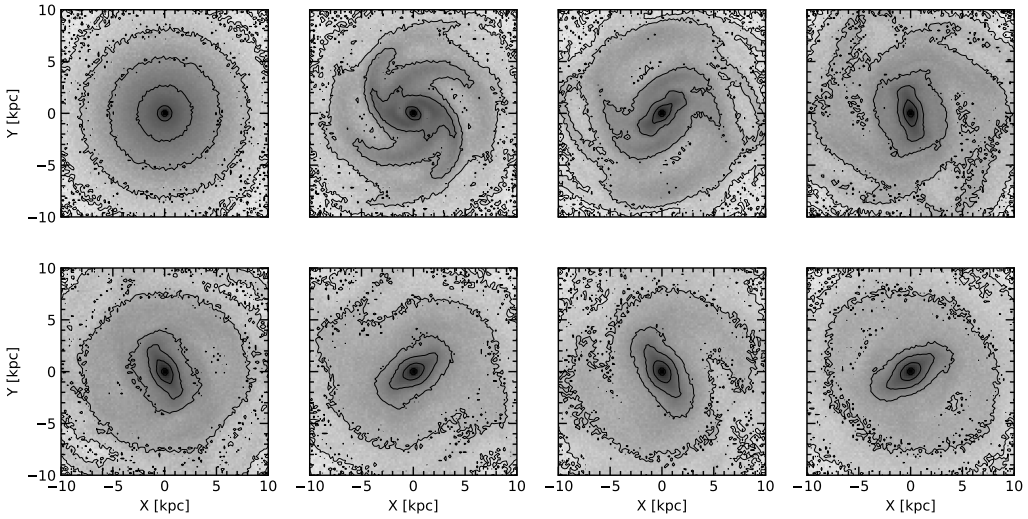

Figure 4.1: The time evolution of the surface density of the stellar components (bulge and disc) over the first 2 Gyr. The snapshots are spaced ∼285 Myr apart. The disc is initially smooth and featureless, but spiral modes seeded by shot noise grow quickly leading to the formation of a strong rotating bar in the centre of the model.

central gas flow (see e.g. Li et al., 2016). Secondly it is completely isolated. The MW is part of the Local Group, with several close neighbours, each of which exert tidal forces on the Galaxy. This could amplify $m = 1$ modes and the off-centring we observe in our model.

4.2.2 Characteristics of the N-body model

We integrate the N-body components using GROMMET. The gravitational potential is calculated using a series of 12 nested inertial grids, with the largest and most coarse extending to 3500 kpc to encompass the entire halo, and the smallest covering the central 850 pc with a grid spacing of 13 pc. The N-body time step is $\Delta t = 1\,\mathrm{km\,s^{-1}\,kpc^{-1}} \simeq 10^5$ yr. We have verified with a number of test simulations that adding an additional inner grid does not affect the gas flow in the N-body potential, nor the macroscopic properties of the N-body model.

Figure 4.1 shows the evolution of the stellar surface density (disc and bulge). As $Q < 1.2$ everywhere in the disc, it is initially bar unstable. Spiral modes grow

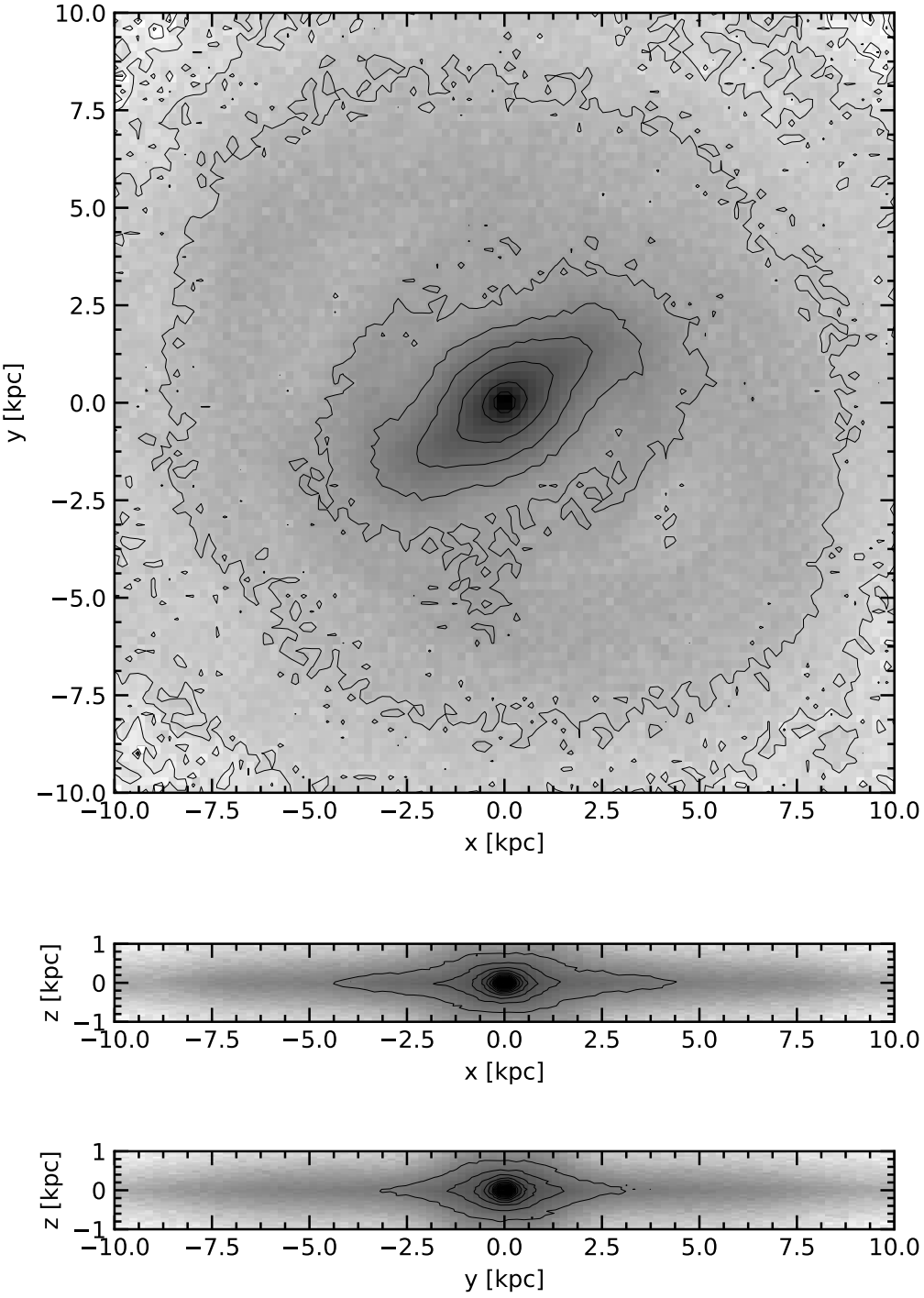

Figure 4.2: The stellar density at 2 Gyr, just before the gas is added.

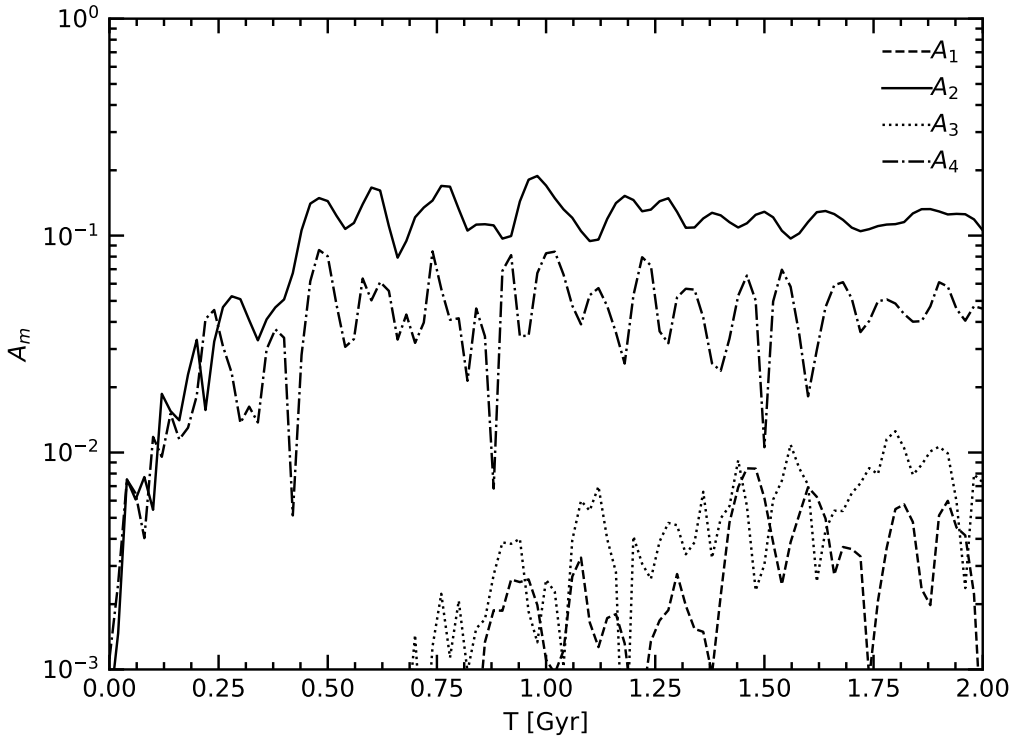

Figure 4.3: The time evolution of the first few Fourier amplitudes in the disc. The odd modes are suppressed to the level of machine error at $t = 0$ due to the symmetry of the initial conditions. The $m = 2$ and $m = 4$ modes grow quickly initially due to the growth of spiral structure and the bar, but reach a maximum strength after around 500 Myr. The odd modes grow more slowly and noisily, but from 1.5 Gyr the strengths of each mode remain fairly constant.

from initial fluctuations in density due to Poisson noise. These spiral waves are swing-amplified and lead to the formation of a strong rotating bar in the centre of the galaxy. The final state of the model is shown in Figure 4.2. By 2 Gyr (the final snapshot) the bar is well formed and the rest of the disc is relatively quiescent. While the side of view of the disc shows a hint of a boxy/peanut bulge structure, it is not immediately obvious, and much less strong than expected when compared to observations of the Milky Way's central regions. This is likely due to the stabilising presence of a massive bulge in our simulations. As previously discussed, the inclusion of a bulge is necessary to produce a realistic gas flow in our models. The lack of a realistic b-p bulge in our model has no effect on our final results, as our gas is well confined to the central plane of the disc.

Figure 4.3 shows the evolution of the first few global Fourier amplitudes in the disc

$$A_m = \frac{1}{N}\Big|\sum_i \exp(im\phi_i)\Big|, \tag{4.3}$$

where the sum is over all disc particles, N is the total number of disc particles and ϕ_i is the azimuthal angle of particle i in a coordinate system centred on the centre of mass of the disc. The $m = 2$ mode is the most dominant due to the bar, it grows quickly initially but reaches a maximum value around 500 Myr and remains fairly constant for the rest of the run. The odd modes are initially suppressed due to the symmetrising step in constructing the initial conditions but grow steadily over the course of the simulation.

Figure 4.4 plots the circular speed $v_c(R)$ (Equation 3.2) as function of radius calculated from the monopole component of the potential. Also plotted are the contributions from each component.

In the simulations of Fux (1999) the coherence of the gas flow in the central regions was destroyed by the density centre of the stellar component of the N-body model wandering around the total centre of mass of the system. This oscillation had an

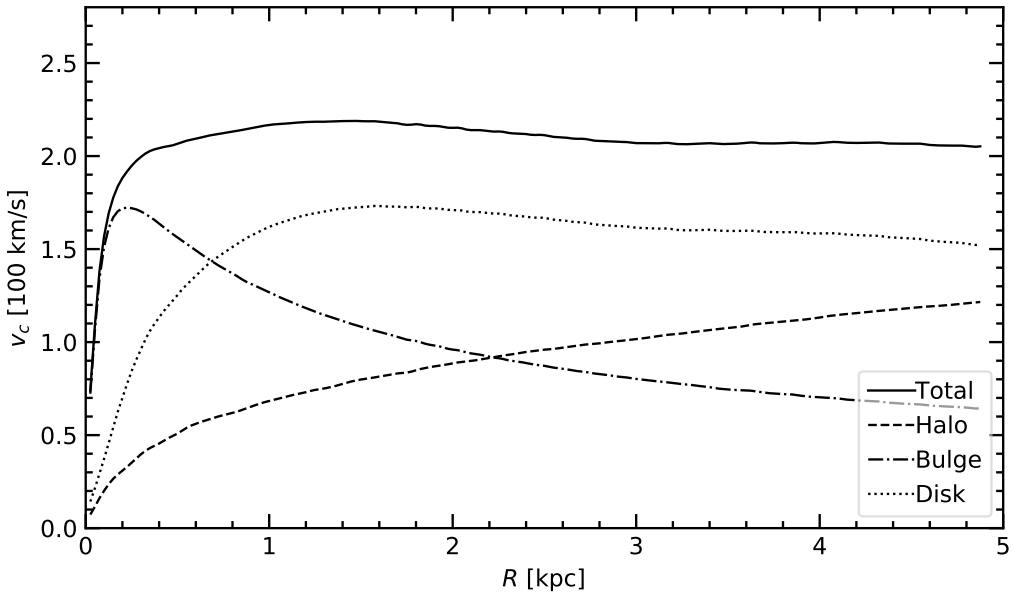

Figure 4.4: The velocity curve calculated from the monopole component of the N-body potential at 2 Gyr. The contributions of each separate component are also plotted.

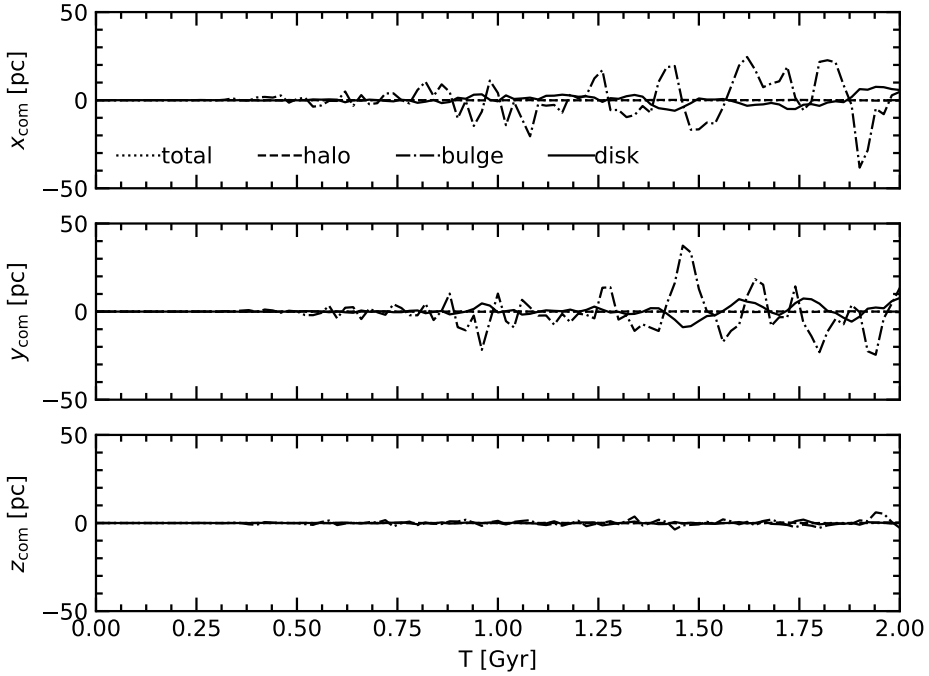

Figure 4.5: The positions of the centres of mass of the three components of the N-body model during the pure-N-body evolution.

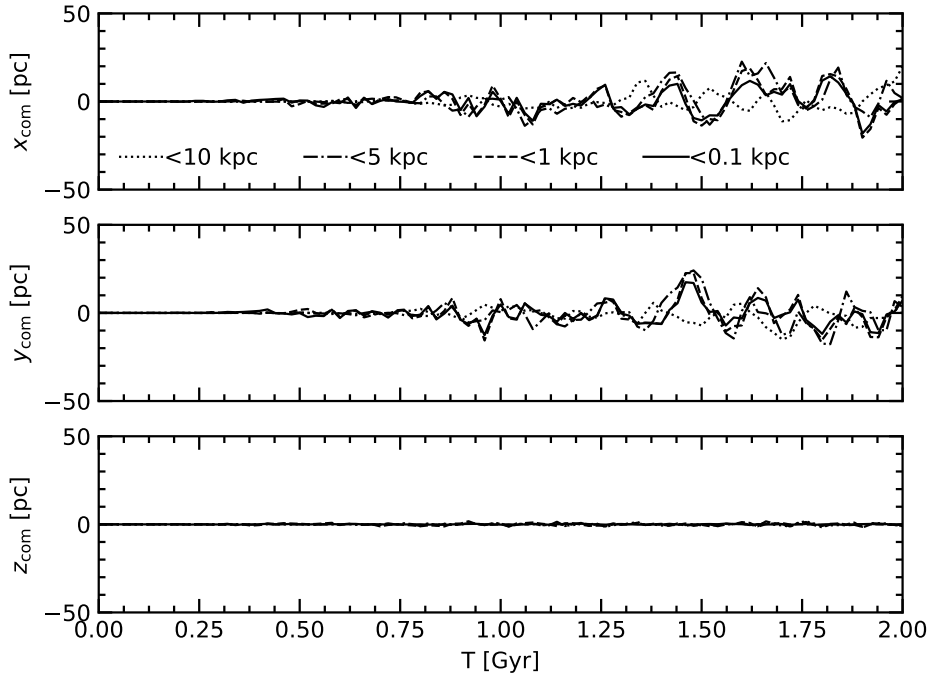

Figure 4.6: The positions of the centre of stellar mass of all stellar particles inside 0.1 kpc (solid line), 1 kpc (dashed line), 5 kpc (dashed-dotted line) and 10 kpc (dotted line) during the pure-N-body evolution. The inner regions remain closely coupled together but move fairly independently of the total CoM.

amplitude of several hundred pc and a frequency of 20-30 km s^{-1} kpc^{-1}. Figure 4.5 shows the positions of the centres of mass of the halo, bulge, disc and entire system for our model. Due to the symmetry of our initial conditions and the momentum conserving nature of GROMMET the total centre of mass (CoM) remains stationary at the origin of the coordinate system. The CoMs of each component are also stationary initially, but do begin to wander around each other in the (x, y) plane, remaining close to $z = 0$. However, these excursions have a maximum extent of a few tens of pc, not the several hundred seen by Fux (1999).

Figure 4.6 shows the centre of mass of all the stellar particles within 0.1, 1, 5 and 10 kpc. The central parts of the simulation are closely coupled and move together, fairly independently of the total CoM of the stellar component. This effect is similar

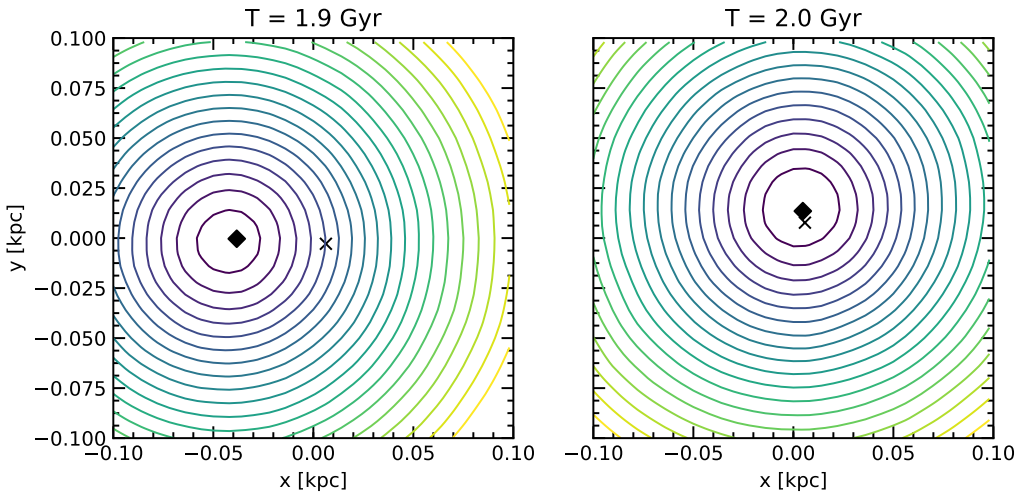

Figure 4.7: Contours of the potential in the inner 100 pc in the (x, y) plane for two snapshots close to the end of the pure N-body simulation, separated by 100 Myr. Also plotted are the centres of mass of the bulge (black diamond) and disc (black cross) for each snapshot. The off-centring of the centre of mass of the inner galaxy causes the minimum of the potential to move away from the origin, tracing this off-centring.

to that seen in Fux (1999).

The wandering of the centre of mass of the inner regions also causes the minimum of the potential to shift away from the origin, as shown in Figure 4.7. This effect is important, because when comparing the N-body potential to the analytic models previously used the most natural thing to do is to expand the potential in a series of multipoles. If this expansion is not done around the minimum of the potential, which as we have seen is not necessarily the origin, then the strength of the odd-m modes will be exaggerated.

The potential solver in GROMMET calculates the potential on a series of nested grids, with the grid spacing decreasing by a factor of 2 between each grid. To analyse the potential we first read it out onto an evenly spaced grid covering 16 kpc × 16 kpc centred on $(0, 0)$, with a spacing of 0.02 kpc to match the hydrodynamic grid. We then translate our coordinate system such that the minimum value of Φ is at the origin. This shift is typically just a single grid point, or 20 pc.

We can now decompose the potential about the minimum in the (x, y) plane into

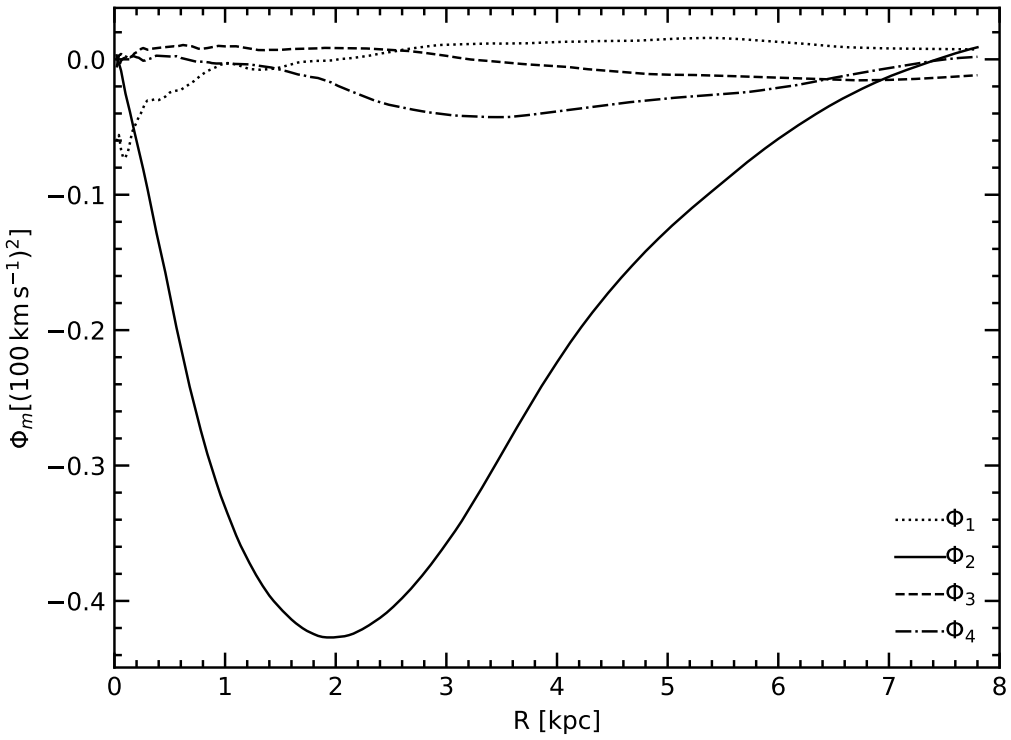

Figure 4.8: The first few multipoles of the N-body potential.

multipoles. We first rotate the potential such that the major axis of the bar lies along the x-axis. We take the angle of the major axis of the bar to be the phase of the $m = 2$ component at the maximum value of $|\Phi_2(R)|$. This phase remains relatively constant over several kpc so this is a reasonably robust definition. We can then expand as

$$\Phi(R, \phi) = \Phi_0(R) + \sum_{m=1}^{\infty} \left(\Phi_m^c(R)\cos(m\phi) + \Phi_m^s(R)\sin(m\phi)\right). \tag{4.4}$$

We will henceforth refer to the $m = 2$ cosine term as the quadrupole. This is the dominant component due to the presence of the bar. All of the sine terms are close to zero in the region of interest, so we will drop the c label for the remainder of this chapter. We will further discuss the effect of this approximation in Section 4.6. The first few cosine terms are shown in Figure 4.8.

We determine the pattern speed of the bar using Fourier analysis, following Sellwood & Athanassoula (1986). We decompose the surface density at each radius into

a superposition of rotating components:

$$\rho(R,\phi,t) = \sum_n \int \mathrm{d}\omega\, \rho_n(R,\omega) e^{i(n(\phi-\phi_{n\omega 0})+\omega t)}. \tag{4.5}$$

By performing the inverse transform and looking at the power spectrum of the coefficients in the (R,Ω) plane for a particular m-mode

$$|\rho_m(R,\Omega)|^2 \propto \left| \int \mathrm{d}t\, \mathrm{d}\phi\, \rho(R,\phi,t) e^{-i(n\phi+\Omega t)} \right|^2 \tag{4.6}$$

we can identify solidly rotating features, as these will appear as ridges that extend over a wide range in R and a narrow range in Ω.

In practice we generally compute the power spectrum from the final 400 Myr of the simulation, as by this point the disc has generally quietened down and the bar is well developed and rotating steadily. We bin the particles into annuli, and extract the desired m amplitude from the Fourier transform of the binned azimuthal density. From this we get a time series of Fourier amplitudes by radius, which we multiply by a $\sin^2(\pi(t-t_i)/(t_i-t_f)$ filter, where t_i and t_f are the initial and final times respectively, to reduce edge effects. Then we Fourier transform in time, and take the amplitude-squared to get the power spectrum.

Figure 4.9 shows logarithmic contours of $|\rho_2(R,\Omega)|^2$ for the surface density shown in Figure 4.1. The bar clearly stands out as a steadily rotating pattern with $\Omega_p = 36\,\mathrm{km\,s^{-1}\,kpc^{-1}}$. We estimate Ω_p as the weighted average of Ω:

$$\Omega_p = \frac{\int \Omega |\rho_2|^2 \mathrm{d}\Omega}{\int |\rho_2|^2 \mathrm{d}\Omega}. \tag{4.7}$$

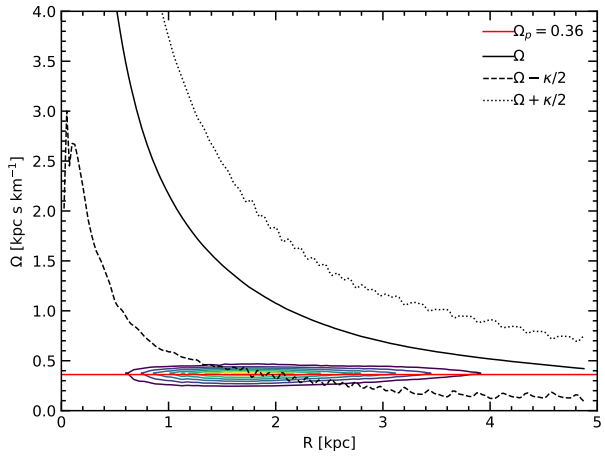

Figure 4.9: The power spectrum of the $m = 2$ component of the density in the (R, Ω) plane, for the simulation presented in Figure 4.1, with frequency curves calculated from the azimuthally averaged potential. The power spectrum is calculated from the last 400 Myr of the pure N-body evolution. The bar is clearly visible as a horizontal ridge at $\Omega = 36\,\mathrm{km\,s^{-1}\,kpc^{-1}}$, stretching over several kpc in radius.

4.3 Gas flow in the live N-body potential

At 2 Gyr we introduce the gas. The hydrodynamic grid has dimensions $8\,\mathrm{kpc} \times 8\,\mathrm{kpc} \times 1\,\mathrm{kpc}$, with a grid spacing $\mathrm{d}x = 20\,\mathrm{pc}$. The gas is initially on circular orbits and in vertical hydrostatic equilibrium as described in Section 2.5.3. We release the gas and allow it to evolve in the full N-body potential, which likewise continues to evolve in time. The gas is purely a passive dynamical tracer and does not contribute to the gravitational potential, nor does it form stars. We use an isothermal equation of state, with sound speed $c_s = 10\,\mathrm{km\,s^{-1}}$. We do not include a gas recycling term as used in Chapter 3, as previously discussed this does not affect the final results. The gas flow takes around 1 bar rotation period, or 160 Myr, to reach a steady state. We evolve the gas for a total of 400 Myr.

Figure 4.10 shows the evolution of the surface density of the gas. Shocks quickly form at the leading edge of the bar, where the gas transitions from the outer x_1 orbit family to the inner x_2 orbit family, forming a nuclear disc in the centre of the model.

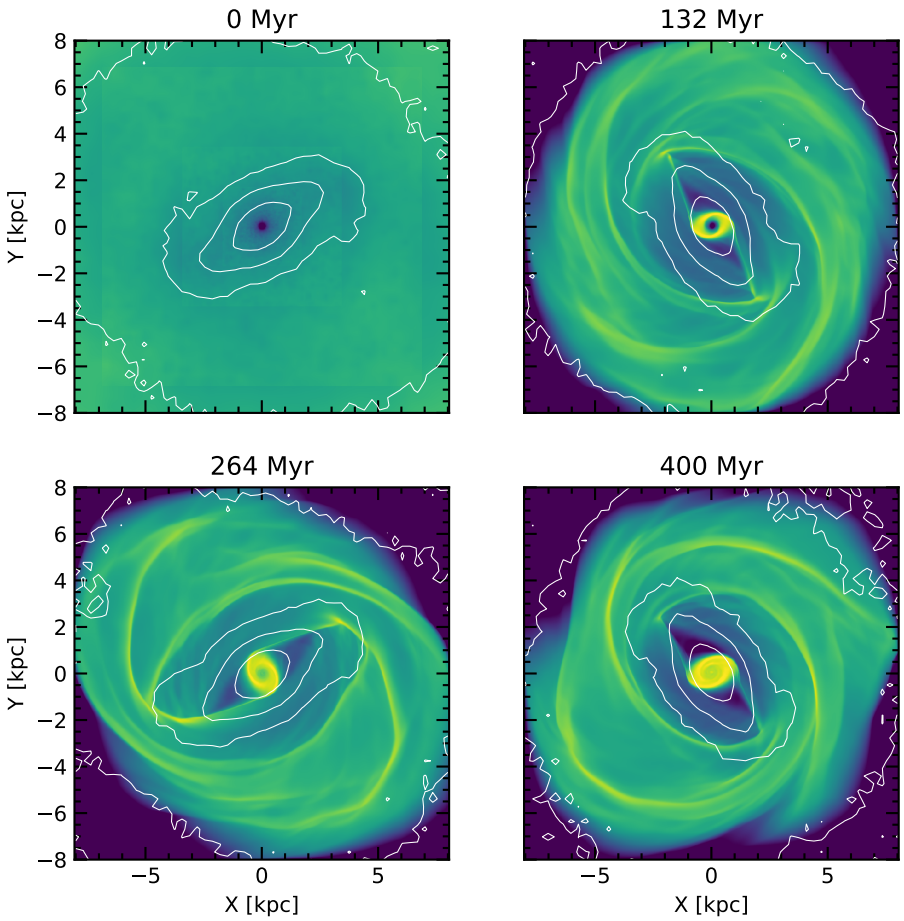

Figure 4.10: The time evolution of the gas surface density of the model. The stellar surface density is also plotted with white contours.

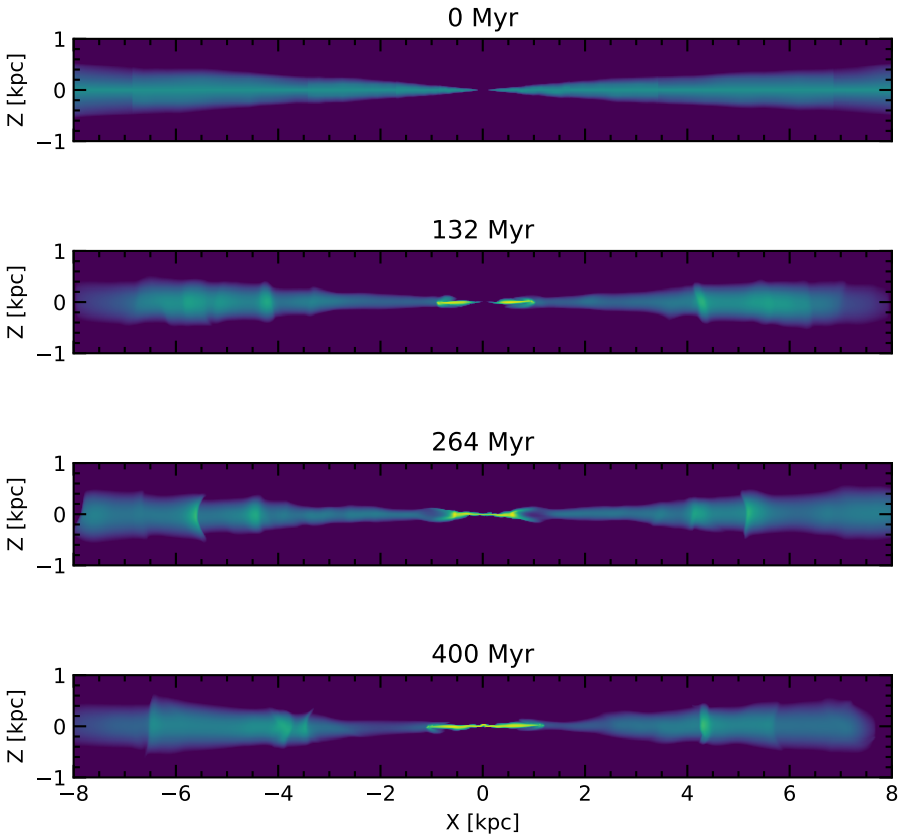

Figure 4.11: A slice of the gas density through the $y = 0$ plane, for the same snapshots as seen in Figure 4.10. The gas remains confined to a thin layer than flares out slightly in the outer regions. The nuclear disc is visible as a slightly tilted disc of high density gas in the centre. Spiral arms in the outer disc can also been seen as bands of enhanced density.

Outside the bar region the gas follows the weakly elongated x_1 orbits, with multiple spiral arms present in the gas density.

The gas flow is mostly bisymmetric about the centre. In particular the positions and shapes of the two dust-lane shocks are very similar, and the nuclear disc remains smooth and elliptical at all times in the simulations. Gas flow in the outer disc is slightly less regular, but still fairly symmetric, particularly the strong 4 armed spiral pattern that connects to the tips of the bar.

Vertically the gas remains well confined to the $z = 0$ plane, as shown in Figure 4.11. The gas disc flares slightly as R increases and the strength of the potential

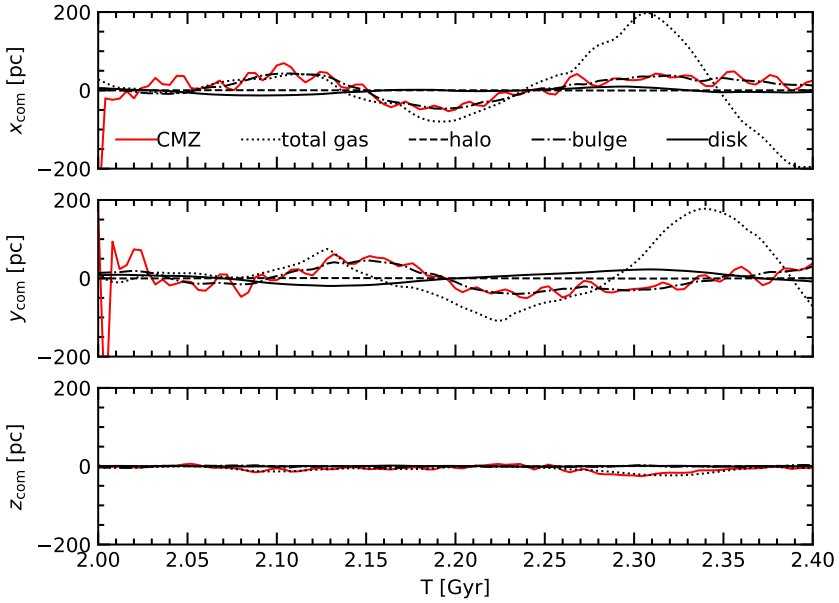

Figure 4.12: The positions of centres of mass of the components of the model. Red solid line: the CMZ of the model, defined as gas within the inner 1.5 kpc with a density greater than the total mean density. Dotted line: the total gas mass. Dashed line: the halo. Dash-dotted line: the bulge. Solid line: the disk. During the gas evolution the centres of mass of each N-body component continue to oscillate around the origin. The gas also does so, with greater amplitude, but the central gas remains closely coupled to the inner mass distribution.

well decreases. Spiral arms in the outer disc also cause the gas thickness to slightly increase. In the centre the nuclear disc remains fairly flat, but tilts slightly. The vertical dynamics of the inner gas will be discussed in more detail in the next chapter. For the most part it appears that we can well approximate the gas as 2D.

4.3.1 How stationary is the gas flow?

During the 400 Myr that the gaseous component is live the N-body model also continues to evolve. The centres of mass of the various components continue to oscillate around the centre of mass of the entire system, and so does the centre of mass of the gas (see Figure 4.12). The excursions of the total centre of mass of the gas are

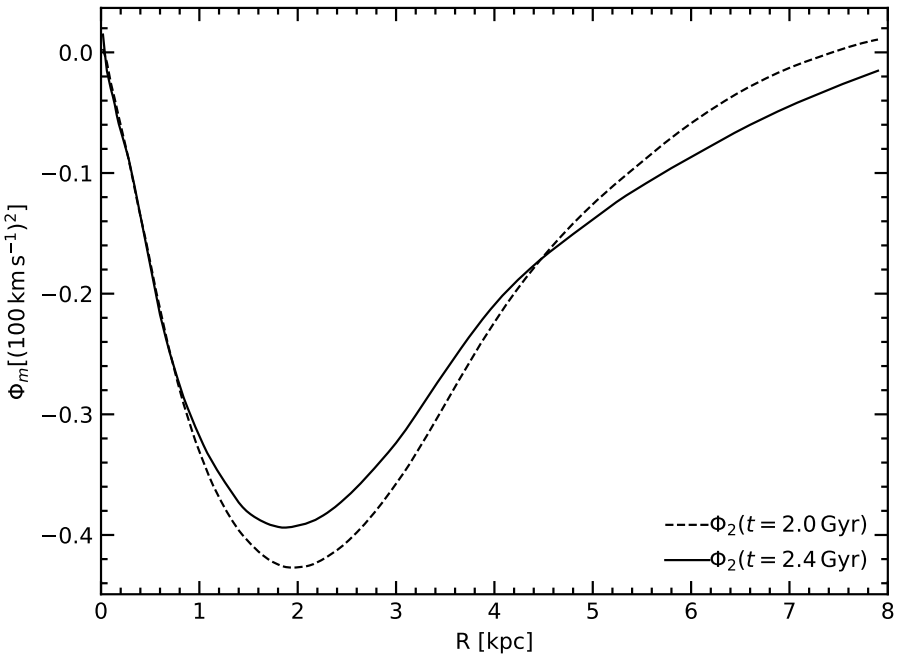

Figure 4.13: A comparison between the quadrupole of the N-body potential at $t = 2.0\,\mathrm{Gyr}$ when the gaseous component is released, and $t = 2.4\,\mathrm{Gyr}$ at the end of the simulation. The quadrupole changes noticeably during this time, becoming weaker and slightly more extended.

several times greater (∼200 pc) than the maximum amplitude of the wandering of the N-body components (∼50 pc), but this effect is exaggerated by the patchy distribution of the gas and the interaction of the outer gas disc with the square edges of the bounding box. The red line in Figure4.12 shows the centre of mass of the CMZ of the models, defined in this case as gas within the central 1.5 kpc with a density greater than the mean density of the entire simulation. The centre of mass of the CMZ remains well coupled to the centre of mass of the inner stellar distribution throughout the entire simulation.

As is shown in Figure 4.13, the quadrupole of the potential becomes slightly weaker and more extended over the course of the gas simulation. The pattern speed of the bar does not change measurably, however. Measuring Ω_p from the final 400 Myr of the pure N-body simulation before the gas is evolved and the 400 Myr of the gas + N-body simulation both give a value of 36 km s^{-1} kpc^{-1}.

As expected, the dynamic nature of the N-body model results in a time dependent gravitational potential. The question to ask is if the variations in the potential are strong enough, and happen on a short enough timescale, that the gas does not reach equilibrium in the potential, to the point where rigid bar models are not a good match to the dynamics of the gas. Alternatively, if changes in the potential are slow enough then the gas will always be close to equilibrium. The dynamical time at $R = 400\,\mathrm{pc}$ is $\sim 10\,\mathrm{Myr}$, far shorter than the timescale over which the variations in the potential become significant. Therefore we would expect the gas in the inner regions not to stray far from equilibrium. However, the dust lane shocks that are feeding the nuclear disc originate at $R \sim 3 - 4\,\mathrm{kpc}$, where the dynamical time is $\sim 100\,\mathrm{Myr}$. So if the central disc is constantly fed gas from the out-of-equilibrium outer regions then it may never have a chance to settle down.

Figure 4.14 shows three snapshots of the central gas surface density during the simulation. The snapshots are seperated in time by 12 Myr. Each image has been rotated so that the major axis of the bar, defined as in Section 4.2.2, lies along the x-axis. There are slight differences between the gas flow in each snapshot; the position and shape of the dust lane shocks vary slightly, as do the spiral arms in the outer disc, but overall the state of the gas remains fairly constant over this short time period. The variation that is present is caused by movement of the tips of the dust lane shocks relative to the major axis of the bar, this has the effect of causing the shocks themselves to kink slightly. The bar of our N-body model does not rotate perfectly as a solid body, and also beats will the spiral pattern present in the outer disc. As a result the positions of the tips of the shocks "wobbles" slightly from one moment to the next, but overall remains well aligned with the bar.

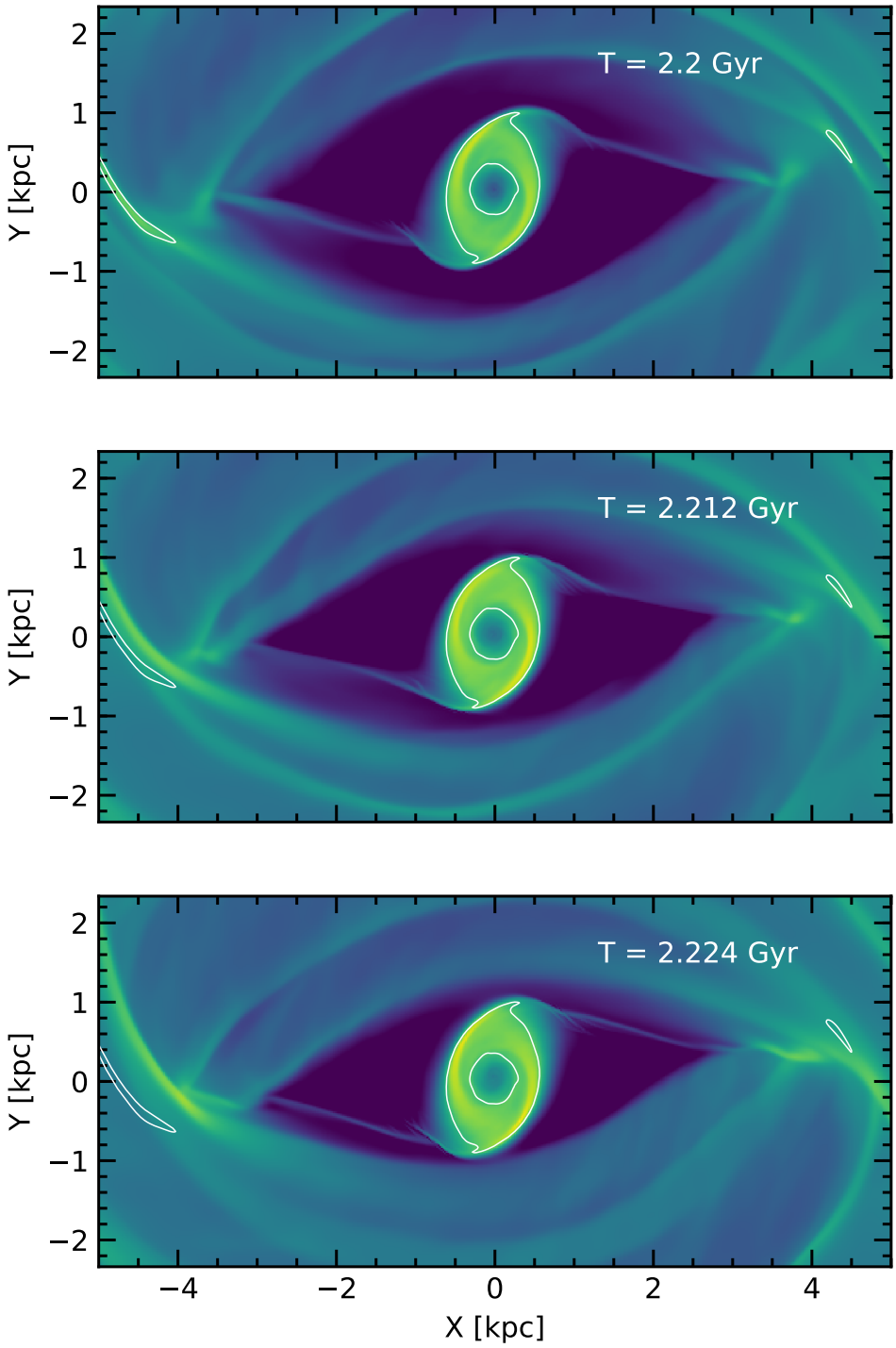

Figure 4.14: The gas surface density in the (x, y) plane for 3 snapshots during the gas evolution separated by 12 Myr. The image has been rotated so that the major axis of the bar lies along the x-axis in all three plots. Also plotted are white contours corresponding to the gas density in the first panel. There are some small changes in the gas flow, particularly at the tips of the dust lane shocks, but overall the gas flow remains fairly constant.

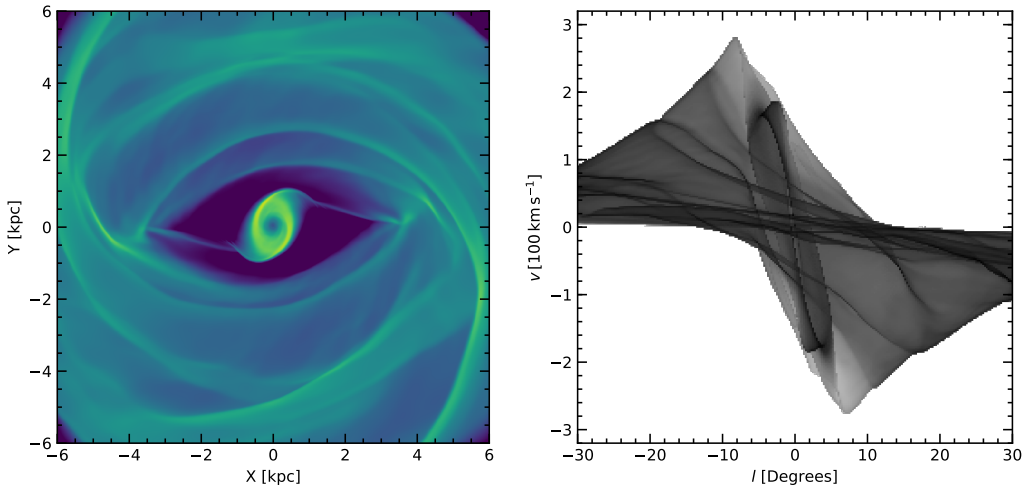

Figure 4.15: The surface density of the gas 200 Myr after the gas is released, and an (l, v) plot created from the model. The gas has been rotated so that the bar lies along the x-axis. The observer is assumed to be at $R_{\mathrm{O}} = 8\,\mathrm{kpc}$ on a circular orbit with $v_{\mathrm{O}} = 220\,\mathrm{km\,s^{-1}}$, and the observer-GC line makes an angle $\phi_{\mathrm{O}} = 20°$ with the x-axis.

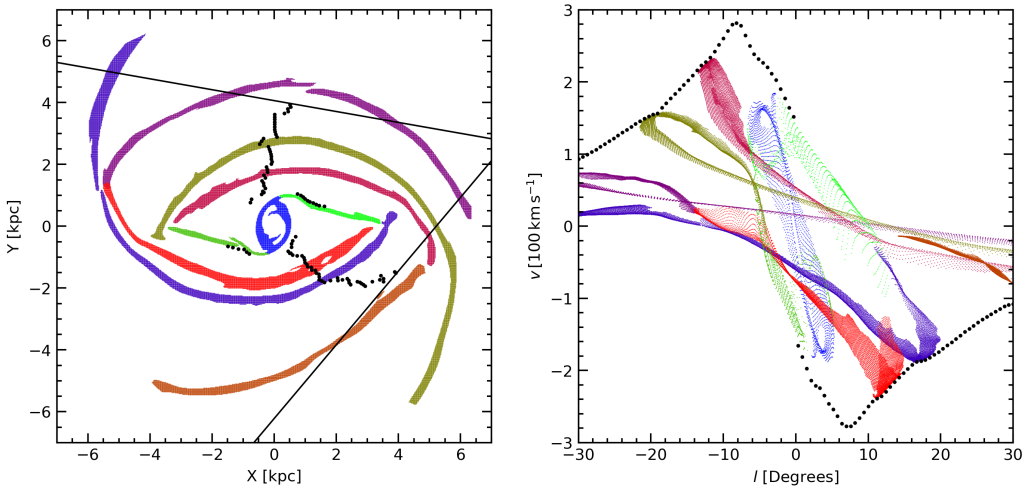

Figure 4.16: Features of the gas flow highlighted in the (x, y) plane, and their corresponding traces in the (l, v) plot. The black lines trace the lines of sight at $l = \pm 30°$, showing the total field of view. The black dots are the terminal velocity points, the positions of the maximum or minimum v at a particular l. Spiral arms in the disc produces ridges in the (l, v), and bumps on the envelope of emission where they are tangential to the line of sight. The central disc appears as a parallelogram-like structure in the centre of the model.

4.3.2 Mock observations

Observations of gas emission from the MW are typically displayed as longitude-velocity, or (l, v) plots. Here v is line-of-sight velocity. To better relate our results to observations we create synthetic (l, v) plots from the model following a simple scheme. We assume that the observer is at $R_{\rm O} = 8\,{\rm kpc}$ on a circular orbit with $v_{\rm O} = 220\,{\rm km\,s^{-1}}$, and that the observer-GC line at an angle $\phi_{\rm O} = 20^\circ$ to the bar major axis, roughly matching the position of the Sun in the MW. We then interpolate the fluid variables onto a grid in heliocentric coordinates and bin in l and v, in bins of width $\Delta l = 0.25^\circ$ and $\Delta v = 2.5\,{\rm km\,s^{-1}}$. We assume that the emission in a particular (l, v) bin is linearly proportional to the mass of gas in that bin. This procedure is equivalent to the simplest possible radiative transfer calculation, assuming that the gas is optically thin. An (l, v) plot created from the model in this way is shown in Figure 4.15.

The complex and non-axisymmetric state of the gas flow in the simulation leads to a similarly complex (l, v) distribution. Figure 4.16 shows several features of the gas flow highlighted by various colours in the (x, y) plane, and their counterparts in the (l, v) plane. This perfectly illustrates the previously discussed argument of Binney et al. (1991) in Section 1.2 as applied to gas flow in our own galaxy. The spiral arms in the outer gas disc lead to ridges of emission spanning the width of the (l, v) plot, and also create "bumps" on the envelope where they touch it. Gas flowing on highly elongated streamlines near the cusped x_1 orbit gives rise to terminal velocities in the centre that are much higher than the local circular speed. The central x_2 disc is clearly visible as a dark parallelogram-shaped region in the inner-most few degrees. Also plotted in black are the points at which the gas reaches "terminal" velocity, or the maximum v for a given line-of-sight. Due to non-circular motions in the disc these points do not trace out a continuous arc.

Our simulations show little if any signatures of the wiggle instability (Section

3.5.2, Kim et al. (2014); Sormani et al. (2015a, 2018b)). This is due to our use of a hydrodynamic grid with spacing $\Delta x = 20\,\mathrm{pc}$, which is large enough to suppress the instability. We have chosen this grid spacing in order to isolate the effect of the time varying N-body potential on the gas, and remove the complicating effect that such hydrodynamic instabilities would have. The effect of resolution on gas flow models in barred potentials is a complex topic (Sormani et al., 2015a), and a full exploration is beyond the scope of this work. In all simulations presented here we keep the spacing of the grid constant.

4.4 How do rigid models compare?

Despite variations in the N-body potential, the gas does appear to reach an approximately steady state. We now compare gas flow in the live N-body potential to two simulations in which the gas evolves in a rigidly rotating constant potential to examine the differences, if any, between the live simulation and the more idealised models of Section 2.3 and Chapter 3. We evolve all rigid models for 400 Myr to match the live simulation.

4.4.1 A frozen N-body model

The most obvious and best fitting choice of model to use for the N-body potential is a frozen snapshot of the N-body potential. Figure 4.17 presents a comparison between the live 3D model (the "live-N-body" model from now on), and a simulation with a constant potential computed from the final state of the N-body model, rigidly rotating with a pattern speed of $\Omega_p = 36\,\mathrm{km\,s^{-1}\,kpc^{-1}}$, which will henceforth be referred to as the "frozen-N-body " model. To prevent any differences in initial conditions between the three and two dimensional simulations affecting the comparison the gas densities of both have been scaled such that total mean density $\bar{\Sigma} = 1\mathrm{M}_\odot\,\mathrm{kpc}^{-2}$. As there is

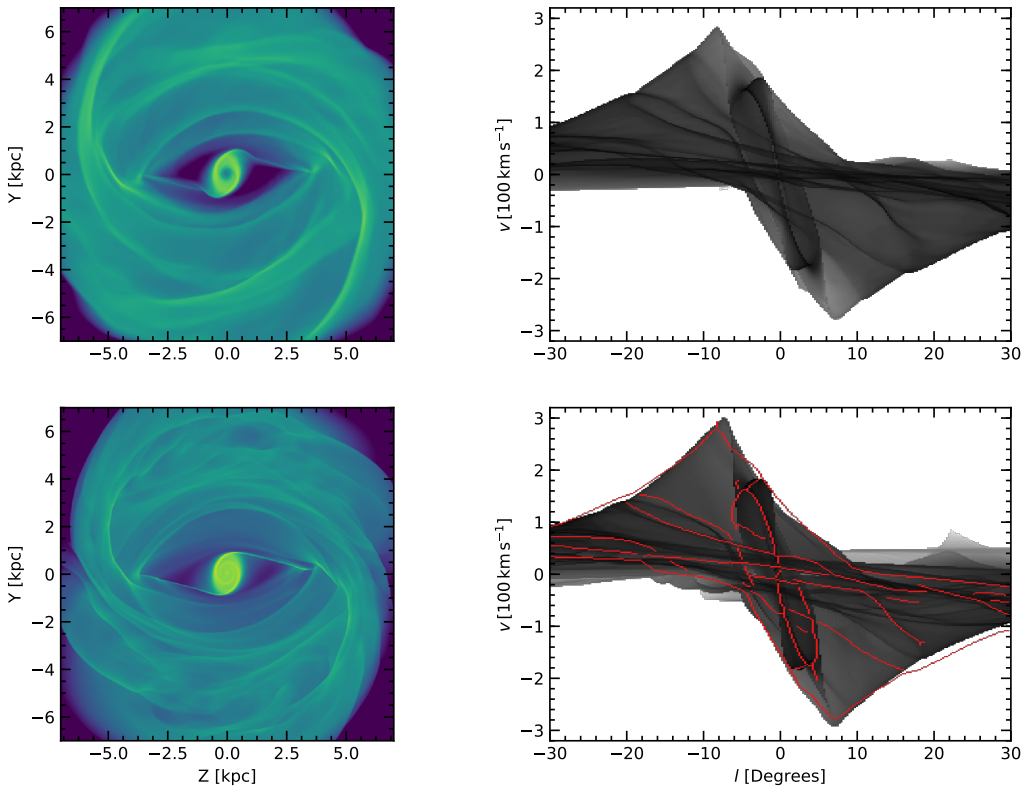

Figure 4.17: A comparison between gas flow in the live N-body simulation and a simulation in a rigidly rotating frozen snapshot of the N-body potential, together with synthetic (l, v) plots created from each model. **Top row:** The live N-body +gas simulation. **Bottom row:** The gas simulation in the frozen snapshot of the N-body potential. The right column shows the final gas density, and the left column shows the corresponding (l, v) plots. Also plotted in red are extracted features from the (l, v) plot of the live model over the (l, v) plot of the rigid model. Overall the two models are a good match, although there are some minor differences, particularly in the outer spiral arms.

no self-gravity, star formation or gas recycling the hydrodynamical equations are left unchanged by a global scaling of ρ.

The models are overall a good match. The gas flow in the centre of the frozen-N-body model is very similar to the central region of the live-N-body model, with the shocks in similar positions and the nuclear disc a similar size. The dust lane shocks of the frozen-N-body model are still slightly asymmetric, both in position and shape. The spiral arms in the central disc are also more clearly visible. Outside the bar region there are more differences in the gas flow. In the live-N-body model the gas density contains several strong coherent spiral arms, spanning a few kpc in radius. While these are arms are present in the frozen-N-body model the gas flow is more turbulent and the arms are broken up.

The (l, v) plots of the two simulations are likewise very similar, with all of the features that present in the gas flow of the full simulation displayed in the N-body model. The envelopes of the two distributions roughly trace each other, as do the locations of the CMZ in each model. The main differences are the slightly more messy internal structure, which is the result of the turbulent gas flow in the outer regions in the frozen case, and the slightly higher terminal velocity peaks in the envelope. In the frozen-N-body model gas on the x_1 orbits reaches further in to the centre of the galaxy before plunging onto the x_2 disc. These orbits have higher line-of-sight velocities as they get closer, so this results in a higher terminal velocity peak on the envelope.

4.4.2 The frozen N-body monopole and quadrupole

The frozen N-body potential, while constant in time and rigidly rotating, is still noisy and asymmetric. As a further test, we compare the live N-body simulation to a model in which the potential consists of the monopole and quadrupole moments of the N-body potential. The other multipoles have been filtered out. In addition to

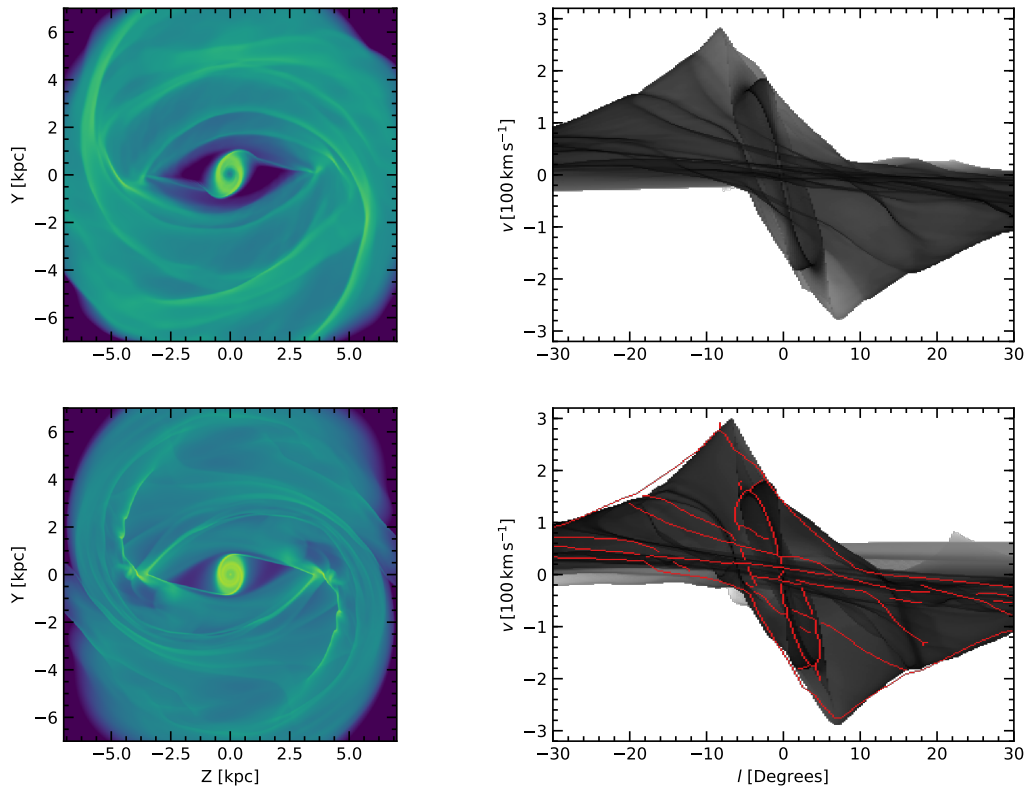

Figure 4.18: A comparison between gas flow in the live N-body simulation and a simulation in a rigidly rotating potential consisting only of the monopole and quadrupole of the N-body potential, together with synthetic (l, v) plots created from each model. **Top row:** The live N-body +gas simulation. **Bottom row:** The gas simulation in a potential consisting of only the monopole and quadrupole components of the N-body potential. The right column shows the final gas density, and the left column shows the corresponding (l, v) plots. Again features from the live model have been plotted in red over the rigid (l, v) plot.

being rigidly rotating, this potential is perfectly bisymmetric.

Overall the gas flow in the simulation appears very similar to the gas flow in the frozen N-body quadrupole, and very close to the live simulation. All of the major aspects of the flow geometry are preserved, including the central disc, dust lane shocks, and outer spiral arms. We would expect this given that the quadrupole is by far the dominant component of the potential (see Figure 4.8). The central x_2 disc is a very similar size, and the dust lane shocks form at a similar place. Given the symmetry of the potential the gas flow is also very symmetric about the centre.

In the (l, v) plane the models are also very similar, with the envelopes reaching a similar height, and internal features in similar positions. Qualitatively at least, any asymmetry in the potential of the live simulation does not seem to have a strong effect on the gas velocity field. The most notable differences again are in the internal features of the (l, v) plot, corresponding to the spiral arms in the outer disc, which do not line up between the two models.

4.4.2.1 The influence of the off-centering

In Section 4.2 we noted that the density centre of the stellar component wanders during the simulation. This produces an off-centering in the potential, resulting in an $m = 1$ mode that is strongest in the inner-most kpc (Figure 4.8). The pure monopole + quadrupole potential does not include this component, so it is interesting to examine the gas flow in the centre of the two models to see if the $m = 1$ component of the potential has any influence on the gas flow.

Figure 4.19 shows a zoomed in view of Figure 4.18. It shows the central 1.5 kpc of the two models, together with (l, v) plots created from gas with $R < 1.5\,\mathrm{kpc}$, highlighting the CMZ. The models are very close; the dust lane shocks in the live simulation have a slight kink in them, but this is a transient feature (Figure 4.14). The CMZ of the live model, which contains a relatively strong dipole term, is very

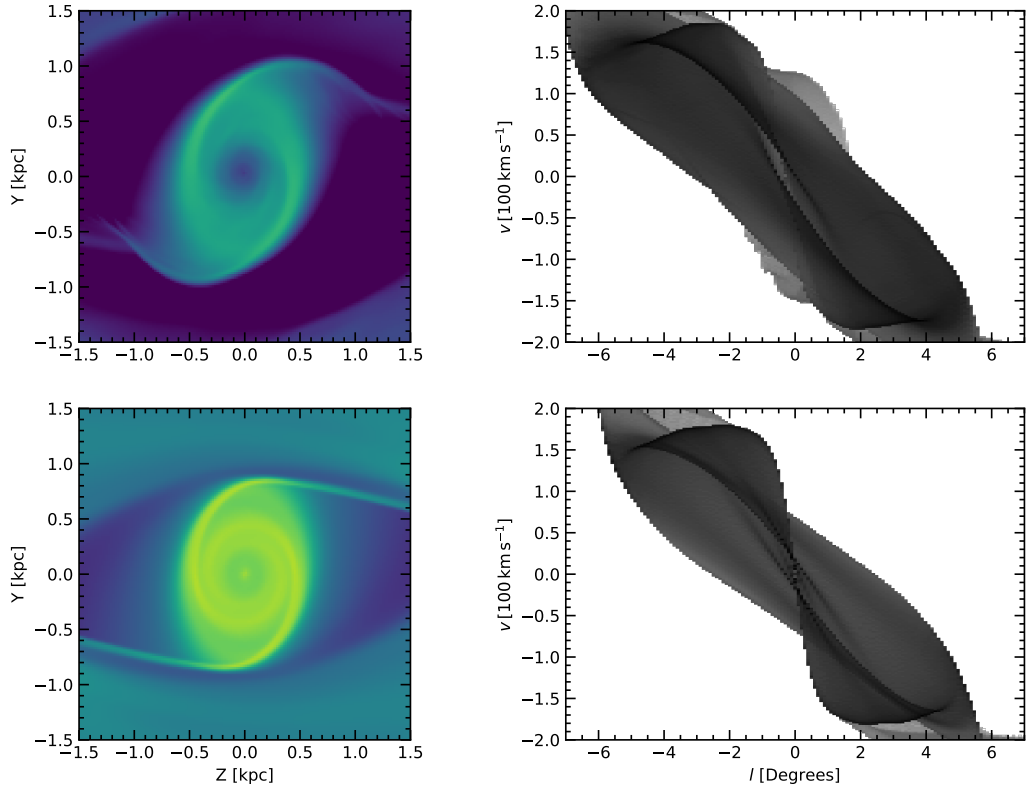

Figure 4.19: A close up view of the gas flow in the centre of the reference model and the N-body monopole + quadrupole simulation. **Top row:** The live N-body +gas simulation. **Bottom row:** The gas simulation in the N-body monopole and quadrupole potential. The left hand panels show the gas density in the simulations, the right hand panels show the corresponding (l, v) projections. The (l, v) plots have been produced from gas within the central 1.5 kpc to highlight the CMZ. Despite the absence of the dipole term in the potential of the rigid simulation, the gas flow in the two models is very similar. It appears that the quadrupole term is by far the most important component of the potential when considering gas flow in the central regions.

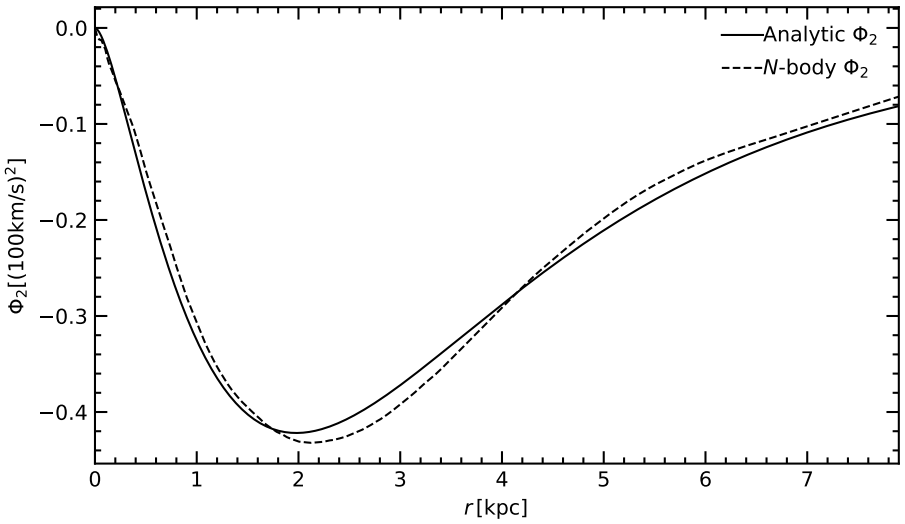

Figure 4.20: A comparison between the quadrupole moment of the N-body potential and the analytic quadrupole model of Equation 4.8.

symmetric, both in the (x, y) plane and in (l, v) space. It appears then that the off-centering has little effect on the central gas dynamics, which are mostly governed by the quadrupole of the potential.

Interestingly, the nuclear spiral reaches further into the center of the nuclear disc and winds up more tightly for the N-body monopole + quadrupole simulation when compared to the live simulation. This may be due to the wandering of the minimum of the potential of the N-body simulation destroying the coherence of the nuclear spiral in the centre, and evacuating the inner-most few pc of gas.

4.4.3 An analytic bar model

We would ideally like to use simple analytic functions to parameterise the density distribution of our models. As a further test, we compare the live N-body simulation to a model in which the potential consists of the N-body monopole together with an analytic quadrupole.. The quadrupole model is that of Sormani et al. (2015c), which

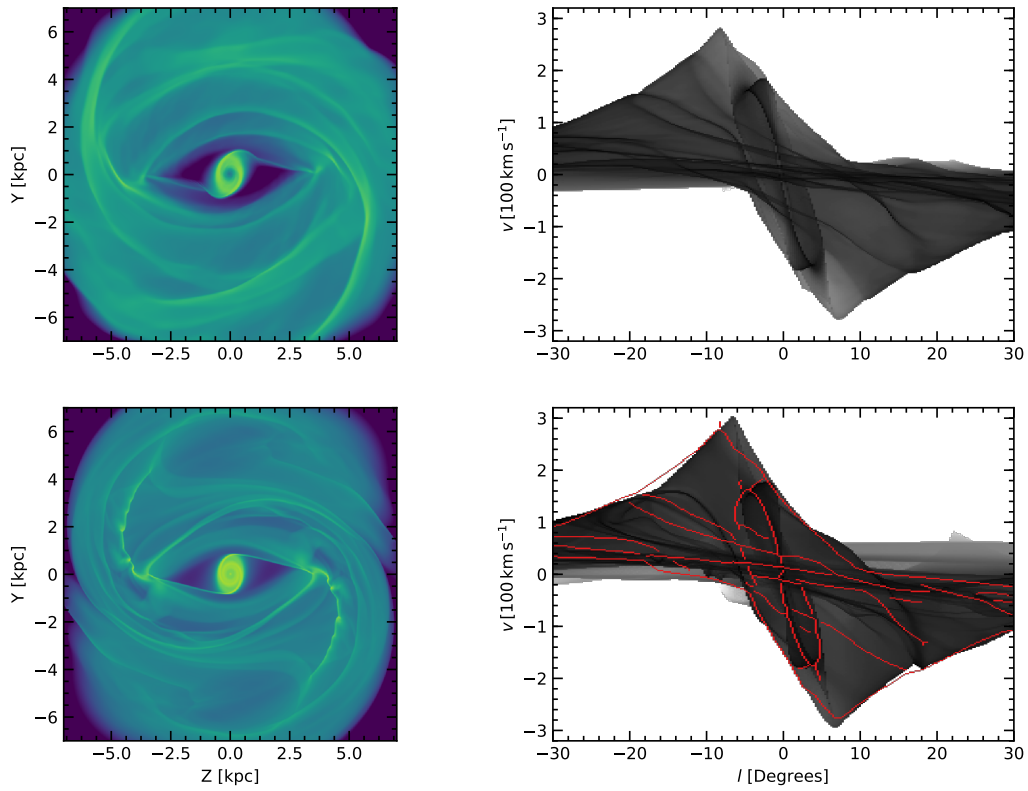

Figure 4.21: A comparison between gas flow in the live N-body simulation and a simulation in a rigidly rotating potential consisting only of the monopole of the N-body potential and an analytic quadrupole, together with synthetic (l, v) plots created from each model. **Top row:** The live N-body +gas simulation. **Bottom row:** The gas simulation in the N-body monopole and analytic quadrupole.

is the quadrupole generated by the following density distribution:

$$\rho_2(r,\phi,\theta) = \frac{A}{4\pi G}\Big(\frac{v_0 e}{r_q}\Big)^2 \exp\Big(-\frac{2r}{r_q}\Big)\sin^2\phi\cos(2\theta) \tag{4.8}$$

where we set $v_0 = 220\,\mathrm{km\,s^{-1}}$ without loss of generality, and G is the gravitational constant. The two main free parameters are A, which controls the strength of the quadrupole, and r_q, which controls the scale length. The quadrupole generated by this density distribution can be conveniently found analytically (Sormani et al., 2017).

We fit this model to the quadrupole of the N-body bar using a simple least-squares method. We find the values of A and r_q that minimise the residual sum of squares between the model quadrupole and the N-body quadrupole sampled linearly in radius between 0 and 8 kpc:

$$\chi^2 = \sum_i \Big|\Phi_2^{N\mathrm{body}}(R_i) - \Phi_2^{\mathrm{model}}(R_i)\Big|^2 \tag{4.9}$$

We find the best fitting parameters are $A = 0.655$ and $r_q = 2.34\,\mathrm{kpc}$, and a comparison between the two quadrupoles is shown in Figure 4.20. It is important to note that this is not the most natural way to fit a model of a potential to the live distribution, but just a convenient method to produce a reasonable analytic model for comparison purposes. Figure 4.21 compares the gas flow in this quadrupole to the live-N-body model.

The gas flow in the analytic-quadrupole model provides a good qualitative fit to the live-N-body model, but quantitative differences become more evident. The shocks form at a similar position, but the nuclear disc of the analytic-quadrupole model is smaller that the live-N-body model. In the outer disc, there is still an $m = 4$ spiral pattern present in the gas, but it is slightly more tenuous and tightly wound. In particular, the spiral shocks emanating from the tip of the bar displays corrugations, a signature of the "wiggle" instability (Sormani et al., 2017).

In the (l, v) plane the picture is very similar. Overall the features are a good match between the two models. The main difference is that the gas reaches higher line of sight velocities. As in the frozen-N-body model, this is because of the smaller size of the x_2 disc in the analytic quadrupole model, that results in the x_1 orbits being occupied closer to the centre. As Sormani et al. (2015c) showed, the size of the /10

x_2 disc is very sensitive to details of the potential, so this difference is unsurprising.

These differences could be down to an inappropriate choice of parameters for the model quadrupole, or it could simply be that our assumed form of ρ_2 is not a close enough model for the potential. We address this question in the next section.

4.5 Observational consequences

We are primarily interested in the gas flow in the centre of the Galaxy because it is a useful dynamical probe of the gravitational potential. The results of the previous section have demonstrated that idealised hydrodynamic simulations in rigid, bisymmetric potentials are qualitatively a good match to simulations with a more realistic live N-body potential. However, there are differences, most notably the size of the x_2 disc and terminal velocity peaks of the (l, v) envelope. This raises the question of whether or not these models can be used to quantitatively constrain parameters of the Galactic potential.

A full search of parameter space would be beyond the scope of this work. We vary only a small subset of the parameters, and investigate only a small subset of the possible model families. We consider the three different models for the potential as presented in Section 4.4: The full frozen snapshot of the N-body potential, the N-body monopole and quadrupole, and the N-body monopole with the analytic quadrupole generated by equation 4.8. With these models we aim to test whether we can reasonably approximate the potential as fixed, if we can safely ignore the

$m \neq 0$, 2 components of the potential, and lastly whether we can approximate the potential with a simple analytic form.

4.5.1 Varying the pattern speed

We first vary the pattern speed for each of the potentials, leaving all other parameters as specified in Section 4.4 unchanged. Ω_p is a key parameter that sets the locations of various resonances in the potential. Increasing the pattern speed moves the resonances inwards, which generally moves the positions of the shocks inwards and shrinks the size of the x_2 disc (Sormani et al., 2015c).

We vary the pattern speed from 25 to 45 $\mathrm{km\,s^{-1}\,kpc^{-1}}$. Our estimate of Ω_p for the live N-body simulation is 36 $\mathrm{km\,s^{-1}\,kpc^{-1}}$. Figure 4.22 shows the gas surface density in each of the three potentials for varying Ω_p. In each of the three potentials the pattern is similar; for increasing pattern speed the positions of the dust lane shocks moves inwards, the x_2 disc becomes smaller, and the gas flow becomes more unsteady as the wiggle instability sets in (Sormani et al., 2017). From a face on view the best match to the reference model (Figure 4.15) in all three potentials is achieved with the correct pattern speed.

Figure 4.23 shows the corresponding (l, v) plots for the simulations in Figure 4.22. As the shocks move further in the velocity of the gas on the inner-most x_1 orbits increases, so the peaks of the envelope rise as Ω_p increases. Likewise as the extent of the x_2 disc shrinks, so does the trace of the gas on the x_2 orbits in the (l, v) plane.

For the full frozen N-body potential, the best fit is clearly produced with the correct pattern speed. The envelope, CMZ, and internal features all line up in the (l, v) plane. However, for the two rigid quadrupole models, while the best fit to the internal features is produced with the correct pattern speed, the envelope actually lines up more closely for the simulations with a smaller pattern speed, at least at negative l. Qualitatively, overall the three (l, v) plots in the central column with the

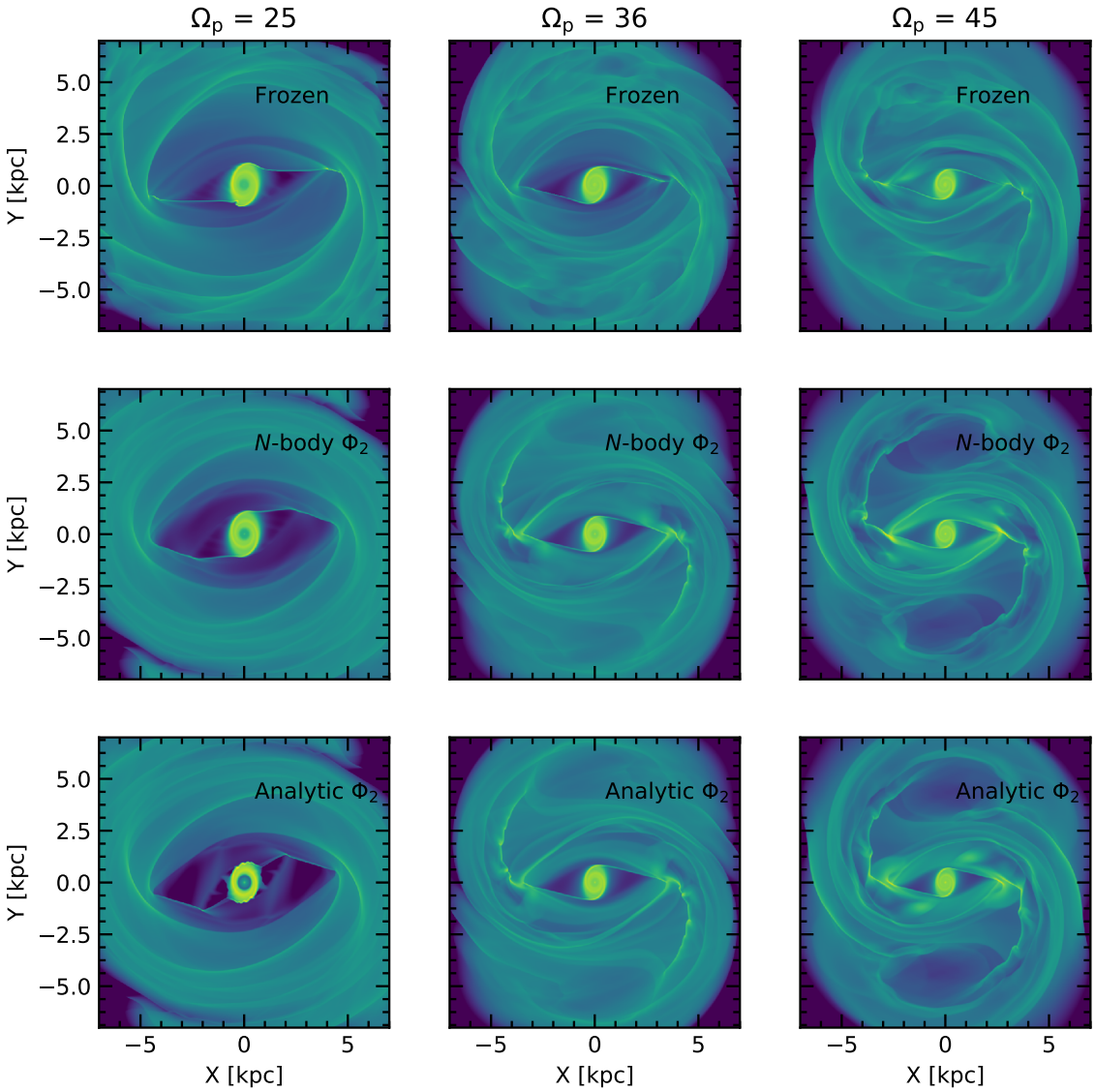

Figure 4.22: The gas surface density in each of the three potentials as the pattern speed of the bar is varied from 25 to 45 $\mathrm{km\,s^{-1}\,kpc^{-1}}$. The top row shows simulations in the full frozen N-body potential, the middle row shows simulations in the monopole and quadrupole components of the N-body potential, and the bottom row shows simulations with the N-body monopole plus a "best fit" analytic quadrupole component.

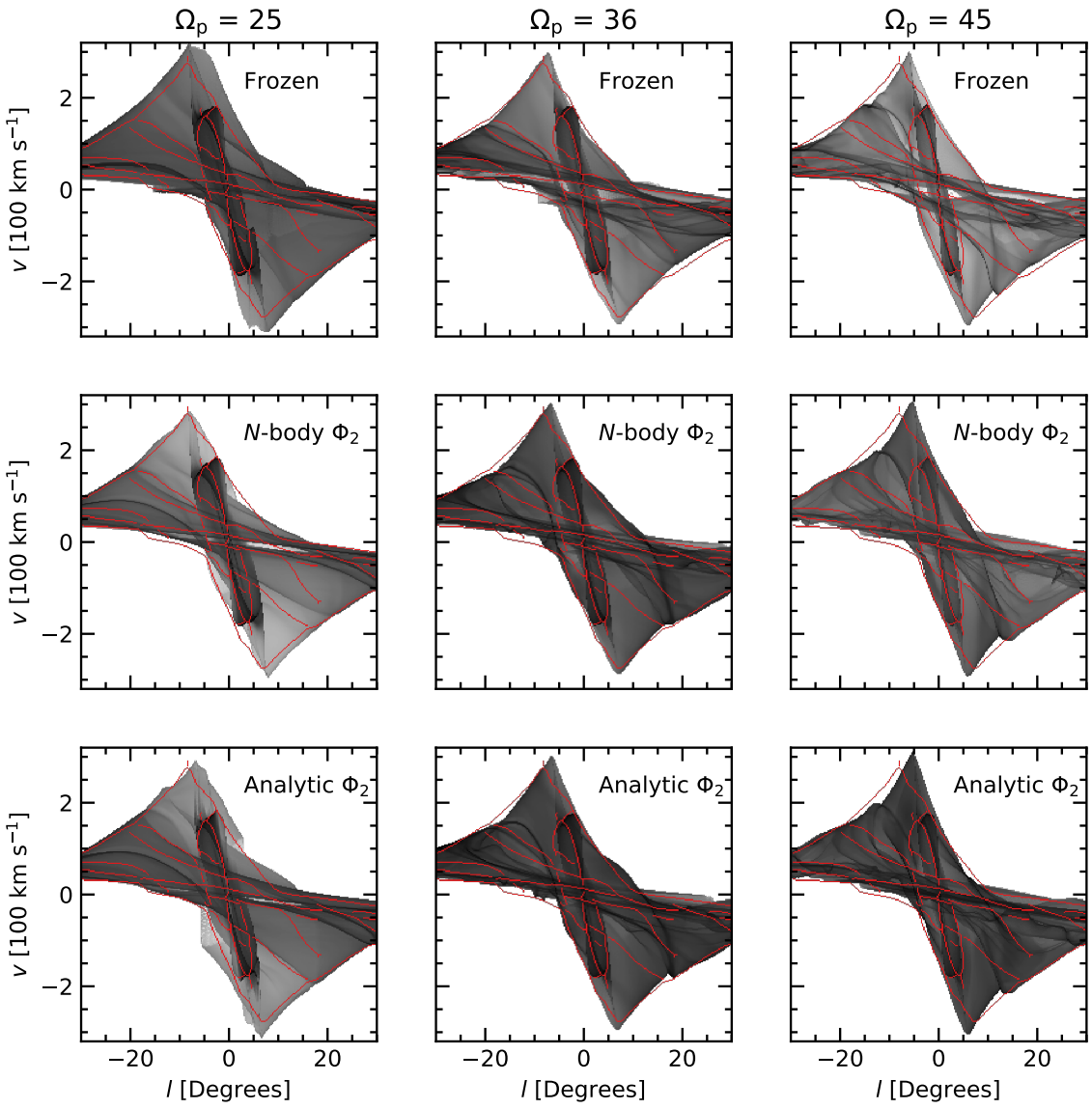

Figure 4.23: Corresponding (l, v) plots for the simulations shows in Figure 4.22. In each the observer is positioned at $R_O = 8\,\mathrm{kpc}$, on a circular orbit with $v_o = 220\,\mathrm{km\,s^{-1}}$, and $\phi_{\mathrm{bar}} = 20°$. Features extracted from the (l, v) plot of the live model are also shown in red in each plot.

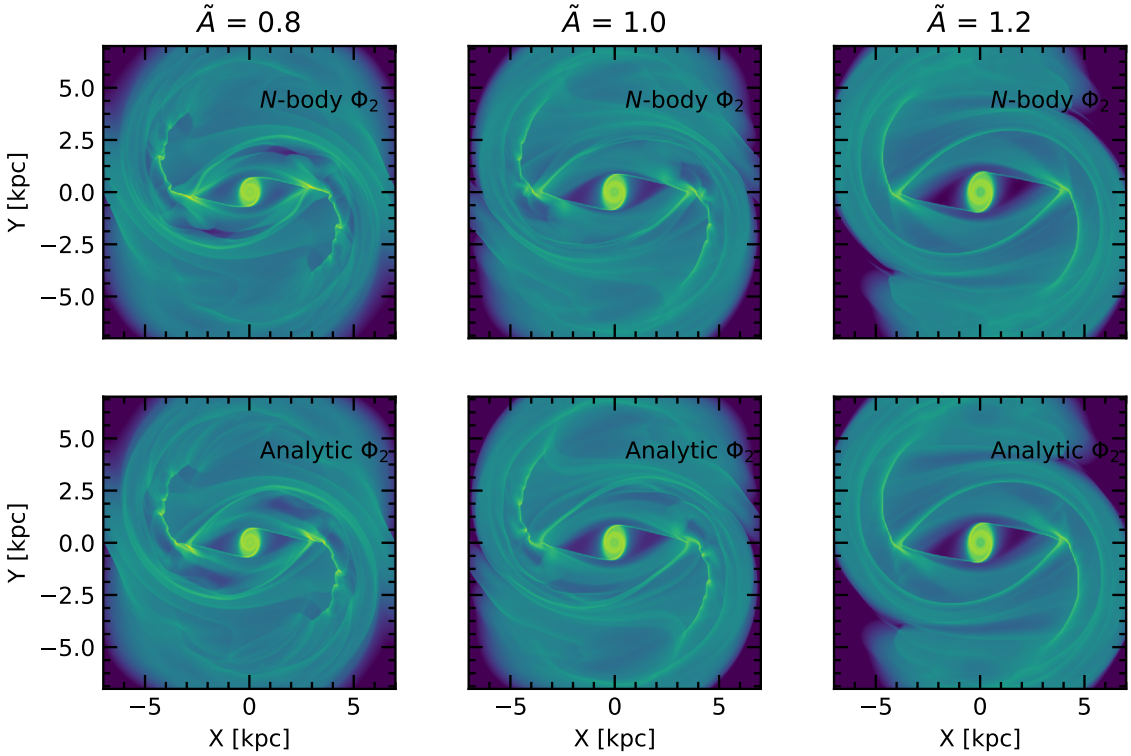

Figure 4.24: The gas surface density in the two monopole + quadrupole potentials as the quadrupole strength is varied from 0.8 to 1.2. The top row shows simulations in the monopole and quadrupole components of the N-body potential, and the bottom row shows simulations with the N-body monopole plus a "best fit" analytic quadrupole component. As the strength of the bar increases the positions at which the gas becomes shocked moves further out, and the size of the x_2 disc increases slightly.

correct Ω_p all appear to be the closest match to the reference model (l, v) diagram.

4.5.2 Varying the quadrupole

Next we vary A and r_q, the strength and scalelength of the quadrupole for the two models with a monopole + quadrupole potential. We scale by two dimensionless factors, $\tilde{A}$ and $\tilde{r}$ respectively, such that

$$\Phi_2(r, \tilde{A}, \tilde{r}) = \tilde{A}\Phi_2(r/\tilde{r}) \tag{4.10}$$

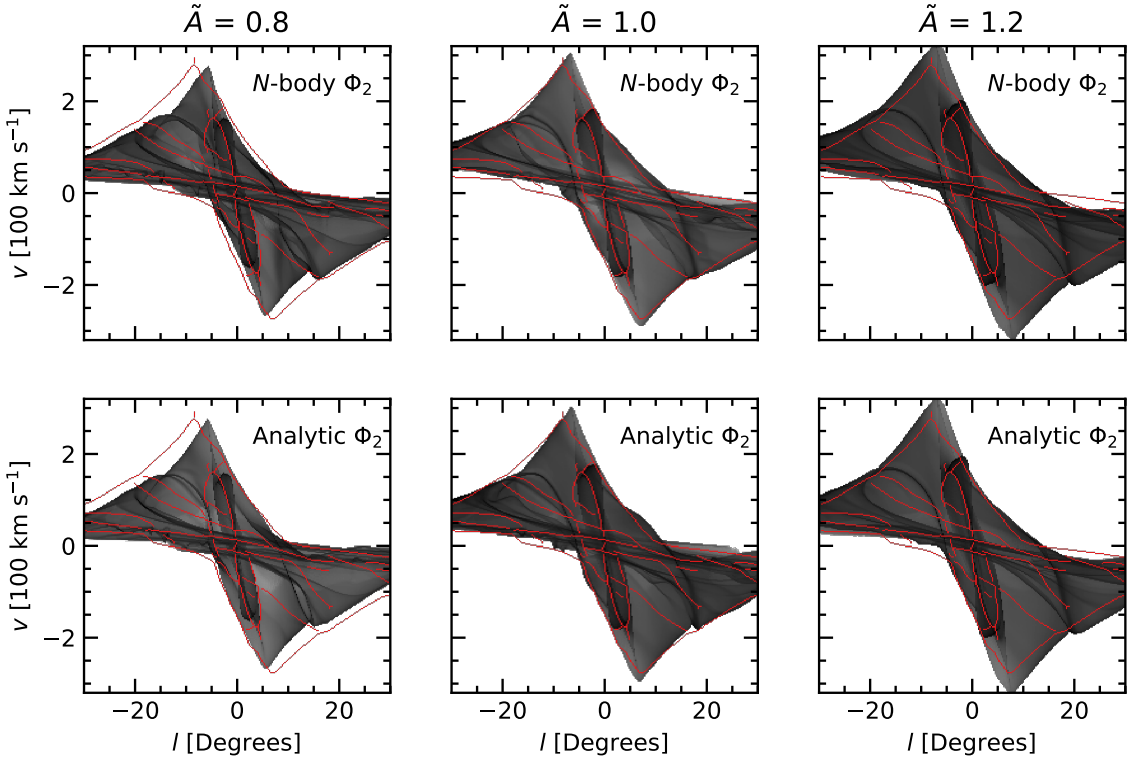

Figure 4.25: Corresponding (l, v) plots for the simulations shows in Figure 4.24. As in Sormani et al. (2015c) the envelope of the (l, v) plots show a strong dependence on $\tilde{A}$, but the internal features are relatively unaffected. As before the red lines trace features from the live model (l, v) plot.

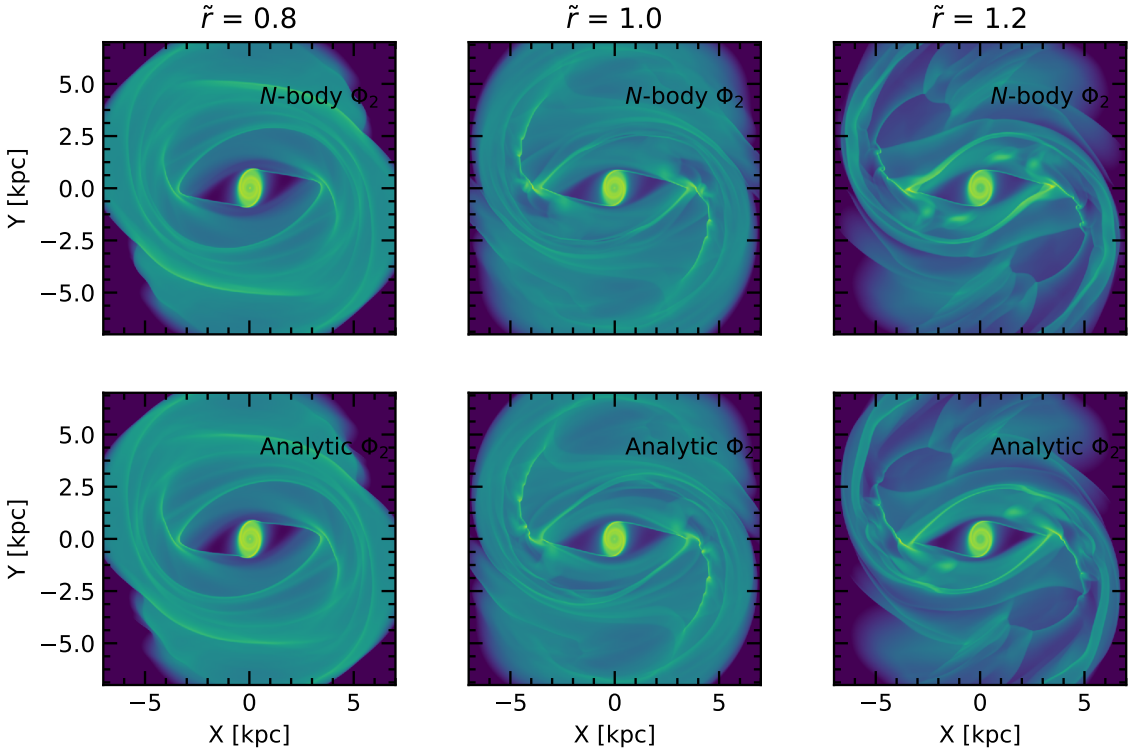

Figure 4.26: The gas surface density in the two monopole + quadrupole potentials as the length of the quadrupole is scaled by 0.8 to 1.2. The top row shows simulations in the monopole and quadrupole components of the N-body potential, and the bottom row shows simulations with the N-body monopole plus a "best fit" analytic quadrupole component. As the scale length increases the strength of the quadrupole decreases less quickly with radius, so the spiral pattern in the gas outside the bar becomes stronger.

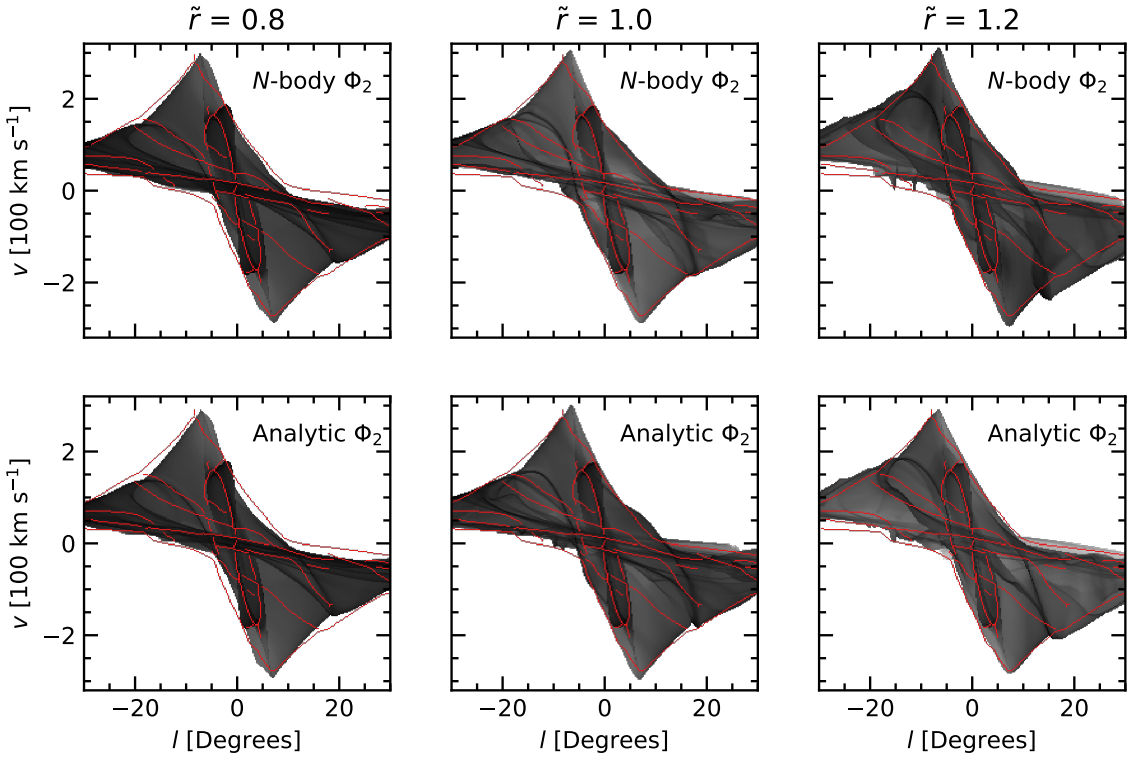

Figure 4.27: Corresponding (l, v) plots for the simulations shows in Figure 4.26. The scale length of the quadrupole has little effect on the envelope of the gas, but more strongly influences the internal features.

where $\Phi_2(r, \tilde{A}, \tilde{r})$ is the scaled quadrupole, and $\Phi_2(r)$ the original. We vary $\tilde{A}$ and $\tilde{r}$ between 0.8 and 1.2 in turn for each of the two models.

Sormani et al. (2015c) studied the effect of the varying these parameters of the quadrupole on the gas flow in barred potential using simulations. They found that the strength of the quadrupole $\tilde{A}$ strongly affects the gas flow in the vicinity of the shocks, and hence the envelope of the (l, v) plot. The scale length $\tilde{r}$ has more of an effect on the spiral arms in the gas, as it sets how quickly or slowly the quadrupole decreased with radius, and hence the strength of the quadrupole in the region outside the bar.

Figures 4.24 and 4.26 show the gas surface density as $\tilde{A}$ and $\tilde{r}$ are scaled respectively. The corresponding (l, v) plots are shown in Figure 4.25 and 4.27. Our results are similar to those found in Sormani et al. (2015c); the envelope of the (l, v) plots is strongly affected by the strength of the quadrupole and only weakly dependent on the scale length, whereas the opposite is true for internal features of the diagrams that are produced by the spiral arms in the gas outside the bar region. This is true for both potential models. Again, by eye features in both the surface density and (l, v) plots seem to line up with the reference model when both $\tilde{A} = \tilde{r} = 1$.

4.5.3 Quantitatively comparing (l, v) diagrams

Making quantitative statements about the fit between models requires defining a measure of similarity. To compare two (l, v) plots it is tempting to use some form of χ_2. However, as Sormani & Magorrian (2015) point out, this is ill suited to the task for the primary reason that (l, v) plots contain a large amount of internal structure and large scale features that the χ^2 measure completely disregards, only measuring similarity on a pixel by pixel basis. If two (l, v) plots are a perfect match, but offset by one pixel, they will have a disproportionately large χ^2 value.

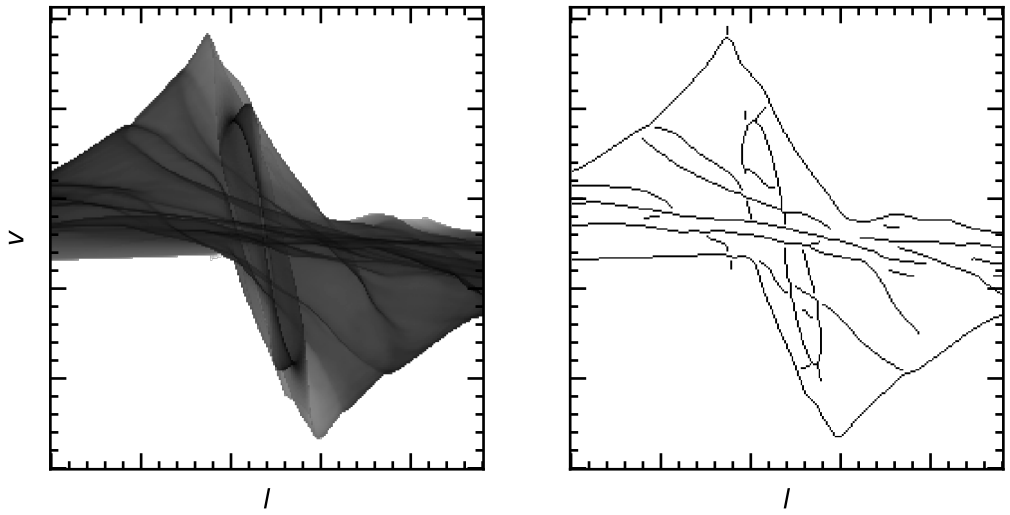

Figure 4.28: The results of applying the automated ridge finding algorithm of Sormani & Magorrian (2015) to the (l, v) plot of the live N-body model. The method automatically extracts the envelope and internal features of the plot. Two binary images created in this way can then be compared using the SMHD, which gives a measure of similarity between two (l, v) plots that takes full advantage of the internal structure of the images.

Sormani & Magorrian (2015) presented an alternative measure based on the Hausforff distance (Hausdorff, 1949), dubbed the Symmetrised Modified Hausdorff distance (SMHD), that they showed to be much more suited to comparing model (l, v) distributions. This method has two parts: Firstly an automated method is used to extract the envelope and features from synthetic (l, v) plots. To summarise, this method is as follows:

1. Firstly the envelope of the (l, v) plot is enhanced by setting all pixels lying on the envelope of emission to the value of the brightest pixel in the image.

2. The image is then convolved with a Gaussian of width 2 pixels to remove any noise.

3. Internal ridges are then extracted from the image by:

   (a) Finding the most negative eigenvalue R and the direction of the associated

eigenvector **p** of the Hessian Matrix (the matrix of second order discrete differences) at each point in the image.

(b) A point is marked as a possible ridge if R is a local maximum along the direction given by **p**.

(c) The possible ridge points are then filtered by hysteresis thresholding, where points are marked as definitely ridges if they are above a high threshold taken as the mean value of R across the entire image, and definitely not ridges if they are below a lower threshold equal to half this value. Points with a value of R in between these two thresholds are only marked as ridges if they are connected to points marked as definitely ridges.

4. Finally, each ridge is thinned to a width of one pixel, and connected components with a total length of four pixels or less are removed.

This procedure extracts from a given (l, v) plot a binary image containing the envelope and internal features. The results of applying this to the (l, v) created from the live N-body simulation is shown in Figure 4.28.

Two binary images A and B produced in this manner can then be compared using the SMHD. This is defined as

$$\mathrm{SMHD}(a, b) = \frac{1}{2N}\mathrm{MHD}(a, b) + \frac{1}{2M}\mathrm{MHD}(b, a), \tag{4.11}$$

where $a = \{a_i\}$ and $b = \{b_i\}$ are the set of non-zero pixels in images A and B respectively, N and M are the total number of non-negative pixels in each image, and MHD is the Modified Hausdorff distance, defined as

$$\mathrm{MHD}(a, b) = \sum_i \min_j \big(d(a_i, b_j)\big), \tag{4.12}$$

where $d(a_i, b_j)$ is a distance metric between pixels a_i and b_j. Effectively this is the

sum of the closest distance to a pixel in image B for each pixel in image A. Sormani & Magorrian (2015) found that the city-block distance,

$$d(a,b) = \frac{|l_a - l_b|}{\delta l} + \frac{|v_a - v_b|}{\delta v}, \tag{4.13}$$

performed the best in their tests. This contains the additional parameter $\zeta = \delta v/\delta l$, approximately the ratio between the typical extension of a feature in velocity and longitude. We adopt $\delta l = 10°$, and $\delta v = 100\,\mathrm{km\,s^{-1}}$ here. As in Sormani & Magorrian (2015) we mask all features with $|v| < 40\,\mathrm{km\,s^{-1}}$, because in real observations low velocity emission is dominated by foreground material. We also generate our (l, v) plots from the gas within $R = 6\,\mathrm{kpc}$, to avoid the edge of the disc influencing the results.

Given the large parameter space of hydrodynamic models of gas flow in the galaxy, quantitative measures of similarity between models such as the SMHD are attractive because they enable automated fitting of models to the data. Here we examine the effectiveness of the SMHD on a small subset of models, to test the sensitivity of the method to the asymmetry and unsteadiness of the live simulation.

To estimate the error of the SMHD, we compared (l, v) plots made from the same simulation with slightly different bar angles ϕ_{bar}. These models should be almost a perfect match, so the SMHD between them will be a lower estimate on the uncertainty in the method. Comparing projections with $\phi_{\mathrm{bar}} = 18 - 22°$ to our reference model with $\phi_{\mathrm{bar}} = 20°$ gives an average SMHD uncertainty of 0.02.

We now turn to quantitatively comparing the models. The SMHD as a function of Ω_p is shown for the three model potentials in Figure 4.29. For the frozen snapshot of the N-body potential (the black line in Figure 4.29) the SMHD behaves very well. There is a clear global minimum at the correct value of the pattern speed, and the SMHD increases reasonably steeply above and below this value. The behaviour for

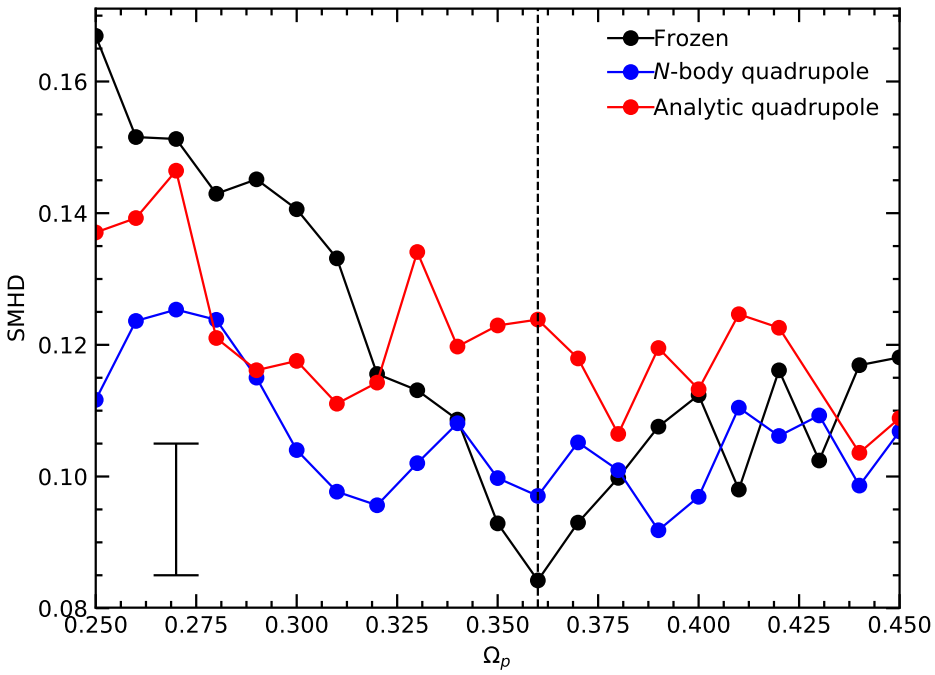

Figure 4.29: The SMHD distance between the live N-body model and simulations in the three model potentials a function of Ω_p, from 25 to 45 $\mathrm{km\,s^{-1}\,kpc^{-1}}$. The SMHD for the frozen N-body potential (black line) shows a clear minimum at the correct pattern speed, $\Omega_p = 36$ $\mathrm{km\,s^{-1}\,kpc^{-1}}$ (dashed vertical line), but the SMHD for the other models (red and blue lines) is more noisy and shows no clear global minimum. A typical error bar is in the bottom left, as estimated from the method described in the text.

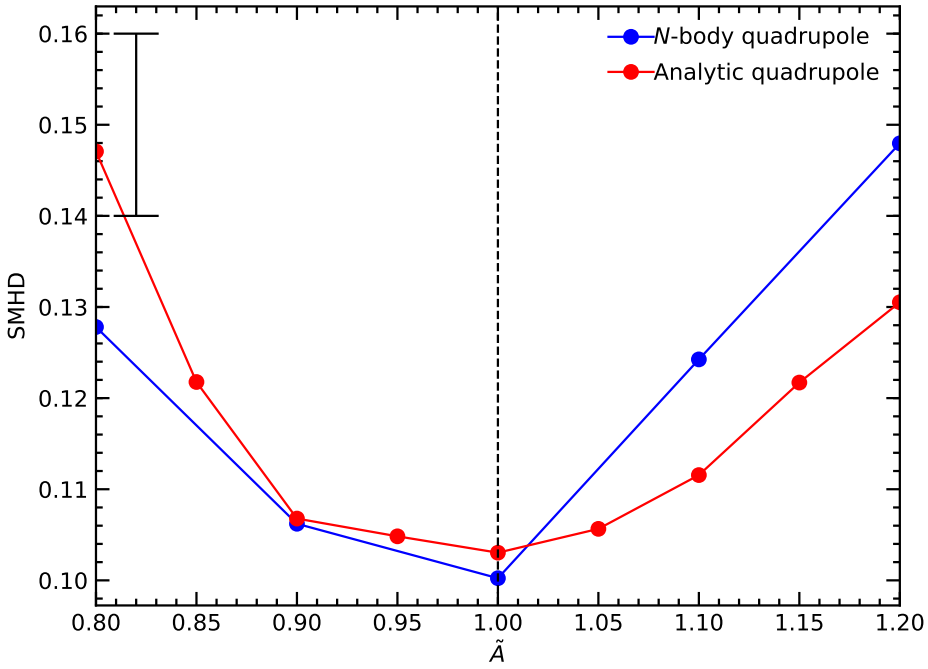

Figure 4.30: The SMHD distance between the live N-body model and rigid simulations as a function of the strength of the quadrupole, $\tilde{A}$, from 0.8 to 1.2. For both the N-body quadrupole (blue line) and the analytic quadrupole (red line) the SMHD shows a clear global minimum at $\tilde{A} = 1$.

the other models is not as good. For the N-body monopole and quadrupole (blue line), there is a hint of a minimum in the region of the correct pattern speed, and a slight increase ruling out models with $\Omega_p < 30\,\mathrm{km\,s^{-1}\,kpc^{-1}}$, but in general most of the points are equal within the uncertainty. For simulations in a potential including an analytic quadrupole, there is no systematic variation of the SMHD with Ω_p.

Figure 4.30 shows the variation of the SMHD to the refence model with $\tilde{A}$ for each of the two monopole + quadrupole potentials. The SMHD does indeed show a strong preference for values of $\tilde{A}$ close to 1. As shown in Figure 4.31 the variation with $\tilde{r}$ is less strong, and shows no clear pattern. The SMHD is most strongly dependent on the strength of the quadrupole because of the effect that scaling $\tilde{A}$ has on the envelope of the (l, v) plot.

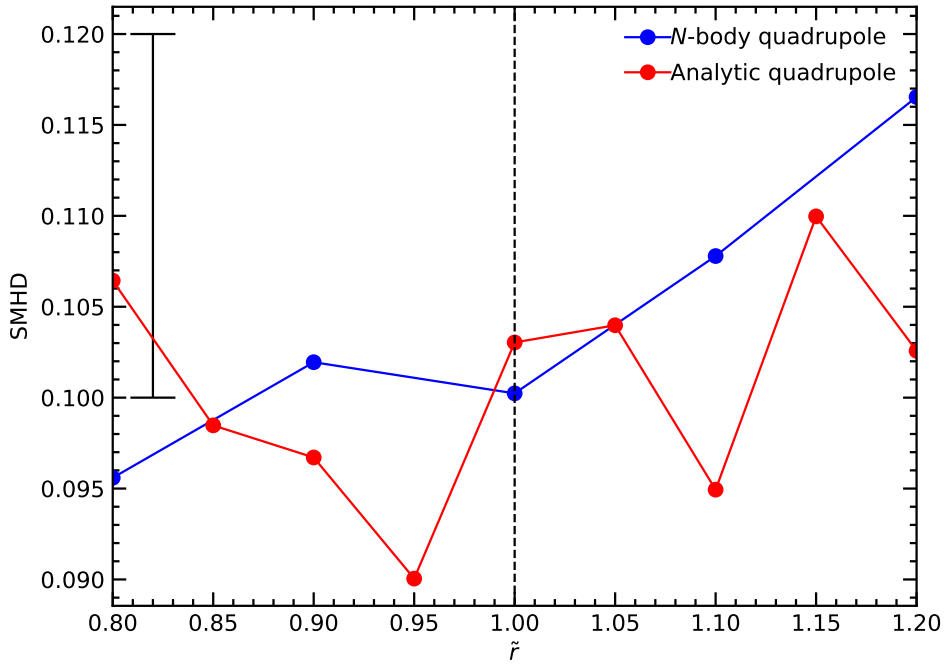

Figure 4.31: The SMHD distance between the live N-body model and rigid simulations as a function of the scale length of the quadrupole, $\tilde{r}$, from 0.8 to 1.2. For the N-body quadrupole (blue line) the SMHD shows a clear bias for lower scale lengths, with a small minimum at $\tilde{r} = 1$, but the best fit is obtained with $\tilde{r} = 0.8$. For the analytic quadrupole, the best fit is obtained with $\tilde{r} = 0.95$, although the SMHD is generally very noisy.

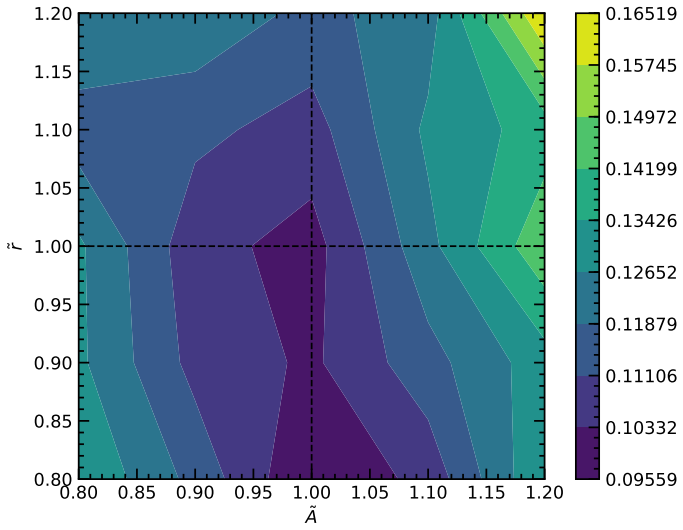

Figure 4.32: Contours of SMHD distance between the live N-body simulation and a grid of simulations with a potential consisting of the N-body monopole and quadrupole, where the strength and scale length of the quadrupole have been varied by two parameters $\tilde{r}$ and $\tilde{A}$. The best fitting models all have $\tilde{A}$ close to 1, but the variation in $\tilde{r}$ is much less strong.

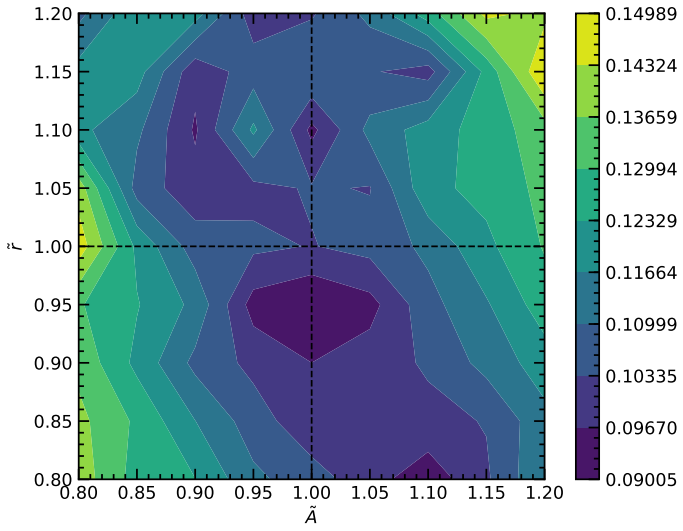

Figure 4.33: As Figure 4.32, but for the N-body monopole + analytic quadrupole potential. The SMHD behaves similarly, models with $\tilde{A}$ close to 1 are a better fit, but the variation is less strong in $\tilde{r}$. There is a strong degeneracy

Next we let both $\tilde{A}$ and $\tilde{r}$ vary simultaneously between 0.8 and 1.2 for each of the monopole + quadrupole potentials. Contours of the SMHD in the $(\tilde{A}, \tilde{r})$ plane are shown in Figures 4.32 and 4.33 for the N-body quadrupole and analytic quadrupole models respectively. In both cases the behaviour is similar, there is a strong preference for models with the correct quadrupole strength, but the measure is far less sensitive to the scale length. There is a significant amount of degeneracy in each figure; for the N-body quadrupole for $\tilde{A} = 1$ all $\tilde{r} \leq 1$ are equivalently well fitting, and for the analytic quadrupole there are multiple different minima all within the range $0.9 \leq \tilde{A} \leq 1.1$, $0.8 \leq \tilde{r} \leq 1.1$.

4.6 Discussion

This chapter aims to answer two questions: Are hydrodynamic simulations in rigidly rotating barred potentials a good match to the gas flow in a realistic live galactic potential, and can we use these models to constrain parameters of the potential by fitting them to observations of the Milky Way? The answer to the first question appears to be yes. We find that generally, despite some time dependence and asymmetry in our live reference N-body simulation, the gas flow appears to remain close to equilibrium at all times, and does not display the kind of unsteadiness observed in the simulations of Fux (1999). Qualitatively simulations in rigid bisymmetric potentials are a good match to the live simulation.

There are two likely reasons for the differences between our conclusions and that of Fux (1999). The first is our use of a Cartesian grid with the momentum-conserving N-body code GROMMET. This avoids any artificial numerical instabilities associated with the polar grid arrangement used by Fux (1999) that could have exaggerated the bar-halo wandering seen in their simulations. The second is our use of a multimass N-body initialisation that increased the particle number resolution in the centre of

our models by several orders of magnitude compared to a single mass N-body model with the same particle number. Whilst we still found that the central regions of our model decoupled from the centre of mass of the simulation as a whole, the timescale of the wandering was slow enough that this did not appear to significantly disturb the gas from equilibrium.

Comparing features in the (l, v) plane by eye, it appears possible to select rigid models that closely match the underlying potential of the live N-body simulation. Successfully fitting these simulations to observations is a different story. We have found that despite promising initial results, the SMHD of Sormani & Magorrian (2015) is not a suitable method for quantitatively comparing our idealised models to the live simulation. This could be due to either a failure in the SMHD to accurately reflect the similarity between models, or a failure in our idealised simulations to capture the gas flow in the live model.

Looking at Figures 4.17, 4.18, 4.21, it is clear that all three models (the frozen N-body potential, the monopole + quadrupole of the N-body potential, and the N-body monopole + analytic quadrupole) accurately capture the gas flow within the bar region, at least from a face on perspective. Outside the bar region the simulations do not line up so well. In our reference model there are large scale coherent spiral arms extending throughout the gas outside the bar, whereas in all of the rigid models these spirals are less coherent, and do not lie in exactly the same place.

The gaseous spiral arms in the live model are influenced by several factors. Barred potentials generate kinematic spiral arms as a result of orbit crowding (Sormani et al., 2015b). The live N-body potential also contains spiral modes in the potential outside the bar region. The phase of the $m = 2$ component of the potential is mostly constant inside 4 kpc, where the bar dominates, but varies outside this region. In both of our monopole + quadrupole potential models we approximate the phase as constant (and equal to zero, so the bar axis lies along the x-axis). It is perhaps unsurprising then

that our models fail to capture the dynamics of the gas flow outside the bar region.

The spiral arm features are responsible for producing the internal ridges across the (l, v) plot, as seen in Figure 4.16. By definition the SMHD weights all pixels in the skeletonised plots equally, whether they are part of the envelope, the trace of the x_2 disc, or the internal ridges. It is clear then why the SMHD does not perform well for the parametrised form of the potentials we have used in our rigid tests. The quadrupole strength, which mostly affects the (l, v) envelope while leaving internal features unchanged, is most successfully constrained by the SMHD. The other parameters we investigated, the pattern speed and quadrupole length, both strongly affect the internal features of the plots. For these parameters the SMHD is attempting to match features that are generated by different mechanisms in the rigid and live models, and so fails to accurately recover the correct parameter values.

In principle one could add a rotating spiral potential to the rigid models, as Li et al. (2016) used in their low pattern speed model of gas flow in the Milky Way. Our results here suggest that such a component is indeed important for accurately reproducing certain features in the data, which they also found. Such a component adds a further set of parameters to the model however, and investigating this is beyond the scope of the current work.

It may also be feasible to alter the SMHD method such that it matches like-for-like features. For example, one could compute the SMHD between the envelopes of the two plots, the traces of the x_2 discs, and the spiral arm features individually, and sum them together. However this then adds the step of correctly identifying and tagging the features in the model (l, v) plots, which due to the large parameter space must be automated, and it is not immediately clear how this would be achieved.

4.7 Conclusions

Simulations of gas flow in barred potentials are commonly used tools to study the ISM of the inner galaxy. Gas is also a useful dynamical probe of the gravitational potential of the Milky Way due to the transparency of gas emission to dust extinction. In such studies the potential of the galaxy is commonly modelled as bisymmetric and rigidly rotating. Previously, Fux (1999) performed hydrodynamic simulations in a live N-body Milky Way analogue. The gas flow in these simulations never reached a steady state, as the potential in the centre of the model fluctuated with time due to the centre of mass of the stellar bar decoupling from the rest of the galaxy. This result suggests that equilibrium gas flow models in rigid potentials have limited applicability to the real galaxy.

In this chapter we have revisited this topic. We have performed three dimensional, symmetry-free hydrodynamic simulations in a self-consistent barred N-body model. The N-body component was carefully constructed to be close to equilibrium, and evolved using GROMMET, a momentum-conserving particle mesh code. After the stellar bar was well formed, an isothermal gaseous component was released in the live potential, and allowed to settle into an approximately steady state.

The potential in the centre of the model did indeed wander around the centre of mass of the system during the simulation. However, the amplitude and time scale of this variation where low and slow enough such that the gas remained approximately in equilibrium. We compared the gas flow in the live models to three examples of simulations in rigid potentials, firstly a frozen snapshot of the N-body potential, secondly a filtered N-body potential consisting of the monopole and quadrupole components, and lastly a potential with an analytic bar model. Despite some differences, all models were qualitatively a good match to the live simulation.

We examined whether these differences were large enough to prevent rigid models from being a good enough match to constrain parameters of the potential. We varied

several parameters of the potential of the rigid simulations, and compared the results to the live N-body model using the SMHD measure defined by Sormani & Magorrian (2015). We have found that when using a simple rigid potential model consisting of a monopole and bar-like quadrupole that the SMHD is unable to meaningfully constrain parameters of the potential, while by-eye fitting methods are still useful. This situation may be improved by adding more components to the potential, or using a more flexible parametrisation, but this has the disadvantage of adding yet more dimensions to an already intractably large parameter space. For example, a simple parametrisation of a realistic potential would require a monopole with an inner and outer slope, break radius and overall normalisation (four parameters), a quadrupole with a strength and scalelength (two parameters) and a pattern speed for a total of seven parameters. Even a coarse grid search with $N = 5$ would require ~ 17000 total simulations to be performed.

Finally we examined the dependence of our results on the resolution of our N-body simulations, and found that the results do not change when applied to a model with twice the number of disc particles.

Our results suggest that while rigid potential models remain a useful tool for qualitatively understanding gas flow in the inner Milky Way, and any time dependence and asymmetry in the gravitational potential should not be strong enough to perturb the gas far from equilibrium, there is still work required to enable automated fitting of gas flow simulations to observational data.

Chapter 5

The Tilted Inner Gas Disc

5.1 Introduction

The gas that lies between $R \sim 3\,\mathrm{kpc}$ and the Solar circle is remarkably flat (Binney & Merrifield, 1998), but observational evidence suggests that gas in the inner-most few kpc of the Galaxy is tilted out of the plane of the disc, although the exact magnitude and orientation of this tilt is somewhat unclear (Burton & Liszt, 1978; Liszt & Burton, 1978; Heiligman, 1987; Ferrière et al., 2007). Given the lack of any large scale vertical asymmetry in the stellar distribution of the Galaxy, one would not expect the inner gas disc to be offset from the $b = 0$ plane, so the magnitude of the observed tilt raises an interesting question as to its origin. Despite several decades of observational study, there has been little work on any dynamical explanations for the vertical arrangement of the inner gas.

In addition to the observed large scale tilt of the gas, there has been recent interest in the vertical dynamics of gas in the CMZ of the Milky Way. Molinari et al. (2011) analysed *Herschel* observations of the CMZ and concluded that they could be well fit by a twisted elliptical ring, corresponding to the 2:1 vertical resonance of gas on x_2 orbits. Kruijssen et al. (2015) alternatively suggested that an open orbital stream,

also oscillating vertically, better fit the observed gas kinematics. In Ridley et al. (2017) we suggested that modelling the CMZ as a tilted disc containing two spiral arm density waves could also fit the data well. More recently Shin et al. (2017) performed SPH simulations in a potential generated by fitting a multipole expansion to an N-body realisation of a Milky Way-like compound galaxy. They found that initially the CMZ in their simulations behaved as a twisted ring, but later settled down into a planar disc, tilted with respect to the plane of the potential.

In this chapter we examine the vertical dynamics of gas in the central disc of a realistic symmetry-free barred N-body simulation. We will show that in this simulation the CMZ indeed behaves as a tilted disc, rather than a twisted ring or open stream. The gas in the central region closely follows ballistic orbits, and the disc tilts as a solid body, with the normal to the gas disc precessing around the normal to the stellar disc in the opposite direction to the circulation of the gas.

This chapter is organised as follows. Section 5.2 discusses the vertical distribution of the inner gas disc of the Milky Way in more detail. In Section 5.3 we examine the vertical behaviour of the nuclear gas disc in live N-body simulations. In Section 5.4 we discuss the relevance of our results and relate features of the simulations to observations of the Milky Way. Finally Section 5.5 sums up.

5.2 The vertical distribution of gas in the inner Galaxy

In a series of papers Burton & Liszt (1978); Liszt & Burton (1978) and Liszt & Burton (1980) presented an early study of the three dimensional distribution of the ISM in the centre of the Galaxy. They argued that the large scale distribution and kinematics of both atomic and molecular gas in the galactic centre could be well fit by a tilted elliptical disc of radius 1.5 kpc. Their model was tilted such that emission

at $l \geq 0$ was mostly at $b \leq 0$ and vice versa, and inclined to the line of sight by $< 90°$ so the near side of the disc appeared below the far side from our position.

Heiligman (1987) studied ^{13}CO emission from the central 2° of the Galaxy and also found that the high velocity gas was tilted anticlockwise out of the plane by around 7°. He also noted that the nuclear disc was more planar, but inclined to the line of sight by $\sim 85°$, such that negative velocity gas on the near side was at negative latitudes, and positive velocity gas on the far side was at high latitudes.

More recently Ferrière et al. (2007) presented a comprehensive review of the gas distribution in the central 3 kpc of the Galaxy. They found that the spatial distribution of emission from the galactic centre was well fit by a two component model. This consisted of a "holed Galactic Bulge disc", an elliptical ring with major axis 1.2 kpc, aligned with the bar, tilted by 13.5° out of the galactic plane, and inclined by 70° to the line of sight. The second component, the CMZ, was represented by a smaller, less elongated elliptical disc tilted by $5 - 7°$ to the galactic plane, and inclined by 85° to the line of sight. As noted by Ferrière et al. (2007), these two components clearly correspond to gas on x_1 and x_2 orbits respectively.

In Molinari et al. (2011), the authors analysed near-IR *Herschel* observations of the inner-most few hundred parsecs of the Galaxy and concluded that gas in the CMZ lay on a twisted elliptical ring corresponding to the stable x_2 orbits of the barred Galactic potential, oscillating with a vertical frequency of twice the orbital frequency, such that the ring formed a twisted figure-of-eight shape when viewed edge on.

Kruijssen et al. (2015) revisited this geometry with NH_3 observations and fit a ballistic orbit in an axisymmetric potential to the data, finding an open orbit that seemed to match the data well. This orbit oscillated vertically, producing a similar edge on view to the twisted elliptical ring of Molinari et al. (2011) when viewed in projection.

Henshaw et al. (2016b) reviewed these interpretations, together with a kinematic

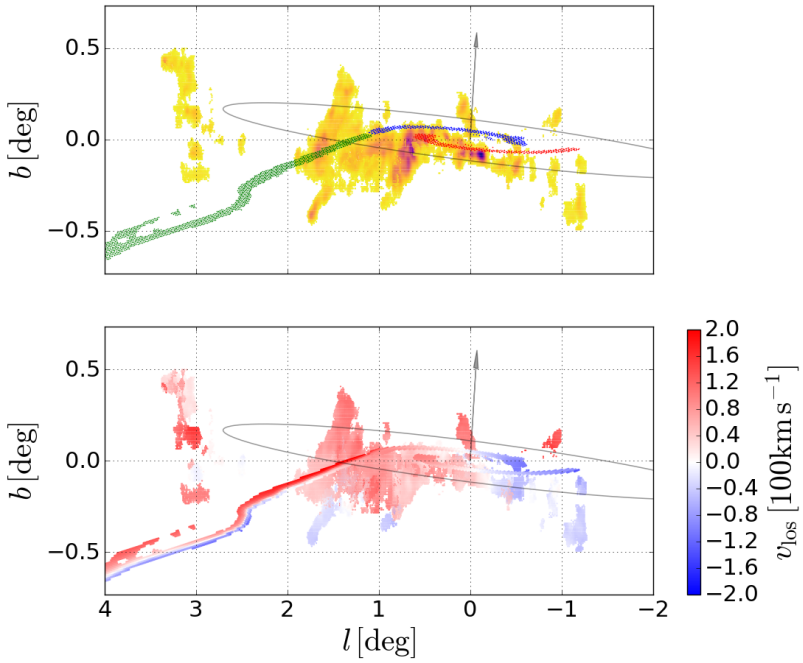

Figure 5.1: A crude 3D model of the CMZ produced by inclining and tilting the simulation as a razor thin disc. The top panel shows the same features highlighted in Fig. 3.7. The bottom panel shows the same, but with both data and model coloured by line-of-sight velocity. The grey arrow shows the normal to the disc $\hat{\mathbf{n}}$, while the grey full line shows the projection of an ellipse elongated perpendicularly to the bar of size 200×400 pc tilted in the same manner as the simulation.

spiral arm model based on the work of Sofue (1995). They concluded that the open stream of Kruijssen et al. (2015) was the most likely. In Ridley et al. (2017) we presented an alternative model of the CMZ as a nuclear gas disc containing two spiral arms. As previously noted in Chapter 3, our dynamical model results in a notably different deprojected geometry than the purely kinematic model of Sofue (1995).

5.2.1 A tilted disc model of the CMZ

This section has been published as part of Ridley et al. (2017).

Here we briefly revisit the observational data and our dynamical model of the CMZ from Chapter 3, and show how constructing a crude three dimensional model from our two dimensional simulations can reproduce the main vertical features of the

observations. Our CMZ model is the nuclear gas disc of a two dimensional hydrodynamic simulation in a rigidly rotating barred potential. Gas in the model forms shocks at the tips of the bar, falling down two opposing dust lane shocks onto the nuclear disc of gas on x_2 orbits in the center of the potential. This too contains two kinematic spiral density waves, that appear in projection as streams crossing the CMZ.

Figure 5.1 shows an (l, v) plot of NH_3 emission from the CMZ (Purcell et al., 2012; Henshaw et al., 2016a) as discussed in Section 3.2. Overlaid on the data are the two spiral arms and the near dust lane shock of our model, as in Figure 3.7. The model has been tilted as a solid body with respect to the Galactic plane.

We can specify the orientation of the normal to the disc $\hat{\mathbf{n}}$ with respect to a coordinate system centred on the GC, with the x axis lying along the major axis of the bar and the z axis lying along the Galactic north pole by two angles θ and ϕ, the usual polar angles in this coordinate system. θ specifies the angle to between $\hat{\mathbf{n}}$ and $\hat{\mathbf{z}}$, and ϕ gives the angle between $\hat{\mathbf{x}}$ and the projection of $\hat{\mathbf{n}}$ into the (x, y) plane:

$$\hat{\mathbf{n}} = \sin\theta\cos\phi\hat{\mathbf{x}} + \sin\theta\sin\phi\hat{\mathbf{y}} + \cos\theta\hat{\mathbf{z}}. \tag{5.1}$$

In this case the angles θ and ϕ correspond to the Euler angles β and α between the Galactic coordinate system and the orientation of the CMZ respectively.

For historical comparison to previous observational work we can also use two angles (i, α), which are usual polar angles of a spherical coordinate system whose zenith lies along the GC-Sun line and correspond to the angles with the same names in Burton & Liszt (1978). If XYZ are cartesian right-handed coordinates centred at the GC with the Sun lying on the positive Z axis and X pointing towards the north Galactic pole, then

$$\hat{\mathbf{n}} = \sin i\cos\alpha\hat{\mathbf{X}} + \sin i\sin\alpha\hat{\mathbf{Y}} + \cos i\hat{\mathbf{Z}} \tag{5.2}$$

i corresponds to the usual inclination angle such that $i = 0$ and $i = 90°$ respectively represent face-on and edge-on discs, while α is the angle that the normal to the disc makes with the line $l = 0$ in the plane of the Sky, measured counterclockwise. In this case α and i correspond to α and $90 - \beta$ respectively, where α and β are the first two Euler angles.

Figure 5.1 shows the results of this procedure for $(i, \alpha) = (85.7, -2.5)°$, which corresponds to $(\theta, \phi) = (5, 38)°$. The top panel shows the regions discussed in Section 3.5.1 and shown in Fig. 3.7, using the same color code. The bottom panel shows the same, but coloured by line-of-sight velocity. The angle between the GC-Sun line and the major axis of the bar is $\phi = 20°$ as before.

Within the region $-1° \leq l \leq 1°$ the majority of the emission lines up well along our spiral arms (blue and red). The tilted model captures the (l, b) structure of the streams. Outside the inner degree the gas has a far larger vertical extent than would be expected from our simple model. As discussed in Section 3.5.1, we interpret this region (i.e., the Sgr B2 and 1.3° cloud, green and purple in Fig. 3.7) as the site of cloud-cloud collisions between material at the inner-most tip of the shock and the nuclear disc. These may result in material being thrown out of the plane, producing the kind of structure seen in Fig. 3.1.

In our model, $i < 90°$, which means that the near arm (red) lies at $b < 0$, while the far arm (blue) lies at $b > 0$. Our value of i is in agreement with previous estimates given in Burton & Liszt (1978); Liszt & Burton (1978) and Liszt & Burton (1980).

We have found that models with small negative α give a qualitatively better fit to the streams, while previous works favoured $\alpha > 0$. Indeed, the first observational evidence mentioned above, i.e. the fact that material at positive (negative) latitude is observed at positive (negative) longitudes, seems to naively imply that $\alpha > 0$. However, Fig. 5.1 shows that there is another possibility: if most of the emission comes from material in and around the green shock then one could still obtain the

observed apparent tilt even with a small $\alpha < 0$. Moreover, the transition point where gas transits from x_1 to x_2 orbits, which is likely to be a locus of bright emission, also lies in the quadrants that give the correct observed tilt in the (l, b) plane. This reconciles our model with previous estimates. Of course, this is not the only possible explanation. We have assumed that the whole inner region lies on the same plane, but it is also entirely possible that the orientation of the disc changes with radius.

5.3 Nuclear discs in N-body potentials

5.3.1 Quantifying the orientation of the central gas disc

In Chapter 4 we presented fully three dimensional symmetry free hydrodynamic simulations in live N-body potentials. We can measure the three dimensional orientation of the nuclear disc in these models in two different ways, by looking at either the density or velocity distributions of the inner gas. We first select the CMZ of the models by only considering gas within the central kiloparsec with $\rho > \rho_{\rm min}$, where $\rho_{\rm min}$ is a density threshold to ensure we select the high density region of the CMZ. Here we use $\rho_{\rm min} = \bar{\rho} = 1 {\rm M}_{\odot} pc^{-2}$, but our results are not particularly sensitive to this value.

We can determine the orientation of the central disc by diagonalising the moment of inertia tensor $\mathbf{I}$ of the inner gas distribution, where

$$I_{ij} = \sum_c \rho_c x_c^i x_c^j \tag{5.3}$$

where the sum is over grid cells in the CMZ. If $\hat{\mathbf{n}}$ is a principal axis, then

$$\mathbf{I}\hat{\mathbf{n}} = \lambda \hat{\mathbf{n}} \tag{5.4}$$

The normal vector to the plane of the gas will be the eigenvector of $\mathbf{I}$ associated with the smallest eigenvalue.

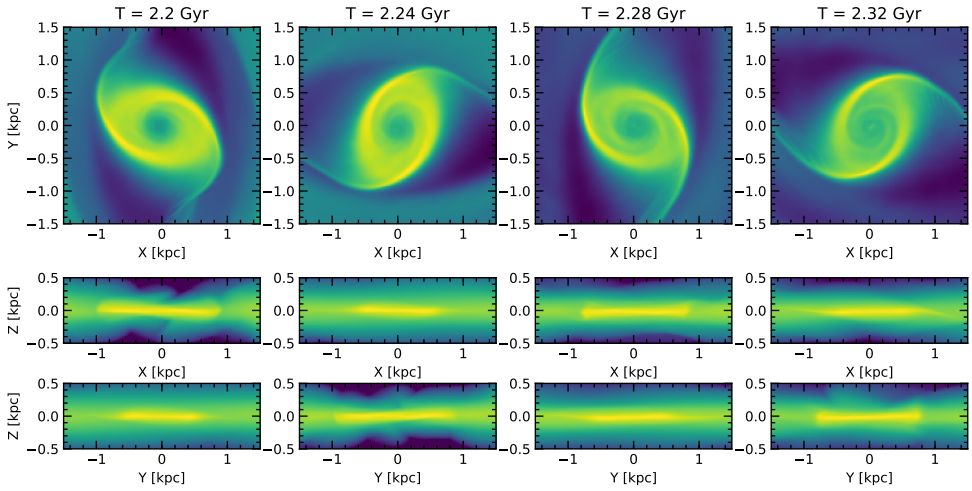

Figure 5.2: A zoom in view of the x_2 disc in the reference model of Chapter 4 during the simulation. The snapshots are separated by 40 Myr. The gas remains confined to a thin disc at all times in the simulation, and this disc tilts slightly with respect to the galactic plane. The gas never forms a twisted ring, or breaks apart into an open stream.

Alternatively, if the gas is generally circulating in a plane, we can find the normal vector to that plane by finding $\hat{\mathbf{n}}$ that minimises

$$\sum_c |\hat{\mathbf{n}} \cdot (\rho_c \mathbf{v}_c)|^2 \tag{5.5}$$

where again the sum is over grid cells in the CMZ.

The gas flow in live N-body potentials is slightly noisy and unsteady. The central gas disc at any instant in time could appear inclined out of the plane due to small fluctuations in the vertical distribution. If the results of these two methods agree, and the magnitude and orientation of the measured tilting is consistent through time, then we can be confident that the gas disc does indeed display a persistent and definite tilt.

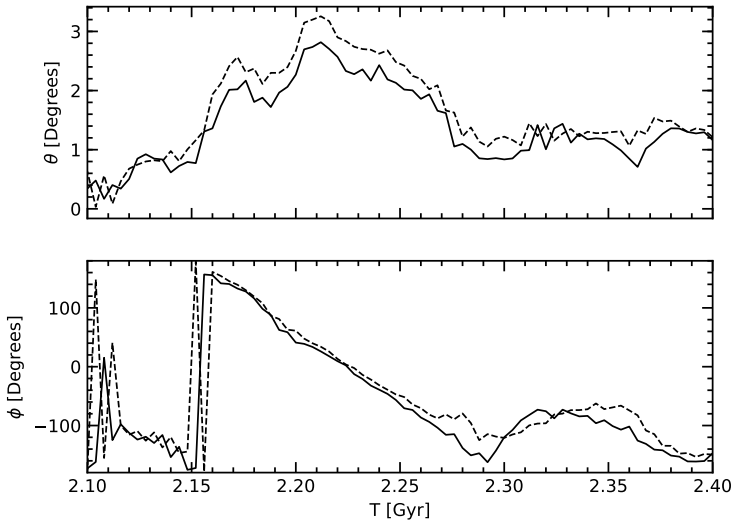

Figure 5.3: The angles defining the orientation of $\hat{\mathbf{n}}$ of the CMZ during the evolution of the simulation, starting from 100 Myr into the gas evolution once the CMZ has formed. *Black solid line:* calculated from from Equation 5.4. *Black dotted line:* calculated from Equation 5.5. The tilt reaches a maximum of $\sim 3°$, and precesses in the opposite sense to the circulation of the gas.

5.3.2 The central disc in our reference model

The N-body model presented here is the same as discussed in Chapter 4. For a full description see Section 4.2.

The model is a multicomponent galaxy, consisting of an initially spherical bulge and halo, both modelled with Hernquist profiles, and a double exponential stellar disc. Structural parameters of the model are given in Table 4.1. We evolve the pure N-body component for 2 Gyr, during which time a strong rotating stellar bar forms in the centre of the disc. After 2 Gyr we release the gaseous component, which is initially axisymmetric and perfectly flat. The gas evolves for several bar rotations, during which time it reaches an approximately steady state.

The gas distribution in the (x, y) plane has been extensively discussed in Section 4.3; due to the non-axisymmetric potential of the bar gas in the outer disc settles onto x_1 orbits, elongated parallel to the bar major axis. Close to the centre these

orbits become self intersecting, this causes shocks to form in the gas at the tips of the bar. Gas plunges down these shocks and settles onto the central x_2 orbits, forming a nuclear disc.

Contrary to the models of Molinari et al. (2011) and Kruijssen et al. (2015), in these simulations we do not observe the CMZ of the models forming either a twisted ring or an open stream. Through the evolution of the simulation, the surface density of the model shows the familiar pattern of gas flow in a barred potential; the outer gas following x_1 orbits, the inner gas following x_2 orbits, and two dust-lane shocks connecting the two regions.

Figure 5.2 shows a three dimensional view of the central disc of gas in the simulation for four snapshots, seperated in time by 40 Myr, starting 200 Myr after the gaseous component of the model was released. Gas in the centre forms a high density thin elliptical disc of gas, that is constantly fed by the dust lane shocks. The orientation of the disc in the (x, y) plane rotates with the bar. Vertically the gas is confined to a thin layer at all times in the simulation, but this disc does tilt slightly with respect to the galactic plane.

The orientation of the normal $\hat{\mathbf{n}}$ to the CMZ in the simulation is shown in Figure 5.3. We specify the orientation of $\hat{\mathbf{n}}$ by θ, the angle between $\hat{\mathbf{n}}$ the z-axis, and ϕ, the angle between the x-axis and $\hat{\mathbf{n}}$ projected into the (x, y) plane. The black solid line shows these angles calculated from the density, by diagonalising the moment of inertia tensor, and the dashed line shows the orientation of the normal to the plane of the circulation of the gas. The results of both methods are well in agreement in terms of the magnitude and orientation of the tilt.

The gas is initially well confined to the plane, but over the course of the simulation θ grows initially to a maximum value $\sim 3^\circ$, and then decreases slightly. Gas and stars in the model are circulating anticlockwise when viewed from above, so $\dot{\phi} > 0$, but interestingly the tilt of the gas disc precesses in the opposite direction, with $\dot{\phi} < 0$.

At $T \sim 2.3\,\mathrm{Gyr}$, after approximately one full period, this precession quite suddenly seems to stop. This is most likely a limitation of resolution of the model. As one grid cell in the model is 20 pc on a side, and the CMZ is $\sim 1\,\mathrm{kpc}$, the minimum resolvable tilt is $\delta\theta \sim 0.02\,\mathrm{rad} \simeq 1°$. As is shown in Figure 5.3, the point at which the precession stops being measurable is precisely when the tilt of the CMZ reaches this minimum resolvable magnitude.

5.3.3 The gas disc in a noisy N-body potential

The tilt we observe in the real CMZ is larger than what we measure in our reference model. There could be many reasons for this discrepancy; we could be lacking some important physical ingredient, our potential could be too quiet, or our initial conditions could be too symmetric. Disregarding the source of the tilt for now, we can examine the response of the gas disc when subjected to a stronger vertical perturbation using a lower resolution N-body model, in which the potential will be noisier and the gas subjected to greater vertical forces.

Parameter	Value	Description
M_t	$1.43 \times 10^{12}\mathrm{M}_\odot$	Total mass
$M_\star$	$5.43 \times 10^{10}\mathrm{M}_\odot$	Total baryonic mass
M_h	$1.37 \times 10^{12}\mathrm{M}_\odot$	Halo mass
a_h	$37.8\,\mathrm{kpc}$	Halo scale length
M_b	$1.5 \times 10^{10}\mathrm{M}_\odot$	Bulge mass
a_b	$500\,\mathrm{pc}$	Bulge scale length
M_d	$4.93 \times 10^{10}\mathrm{M}_\odot$	Disc mass
Σ_d	$0.0995 \times 10^{10}\mathrm{M}_\odot\,\mathrm{kpc}^{-2}$	Central disc surface density
R_d	$2.5\,\mathrm{kpc}$	Disc scale length
z_d	$300\,\mathrm{pc}$	Disc scale height
N_t	5×10^5	Total number of particles
N_h	2×10^5	Number of halo particles
N_b	1×10^5	Number of bulge particles
N_d	2×10^5	Number of disc particles

Table 5.1: Parameters of the low resolution toy model.

The model is constructed using the method described in Section 2.5. The struc-

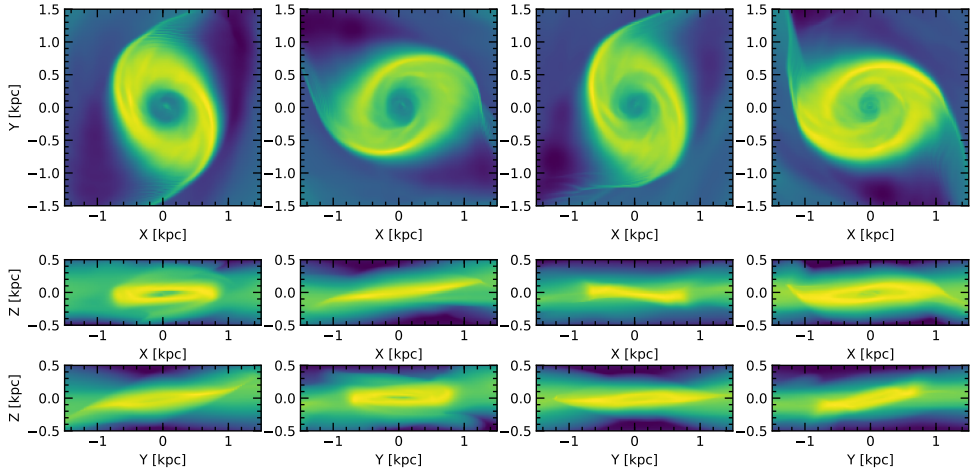

Figure 5.4: A zoom in view of the x_2 disc at various stages during the low resolution N-body simulation. The snapshots are seperated by 40 Myr as in Figure 5.2. Despite the noisier potential, the gas remains confined to a planar disc, but as expected the disc tilts out of the plane by a greater angle than in the higher resolution N-body potential.

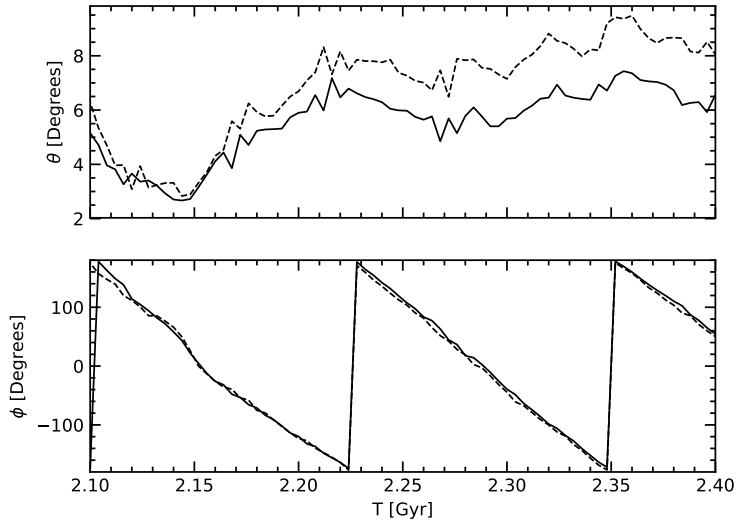

Figure 5.5: The angles defining the orientation of $\hat{\mathbf{n}}$ of the CMZ in the low resolution N-body potential during the evolution of the simulation. *Black solid line:* calculated from from Equation 5.4. *Black dotted line:* calculated from Equation 5.5. The results still agree closely, although towards the end of the simulation the estimation of θ differs by a degree or so. The magnitude of the tilt is larger than in the smoother potential, but the direction and rate of precession is similar.

tural parameters of the model are again based on the best fitting model of McMillan (2017), as is the reference model, but with with a factor of 4 less particles in each component, so the halo and disc are represented by 2×10^5 particles, and the bulge by 1×10^5 particles. The structural parameters are summarised in Table 5.1. We again evolve the N-body components for 2 Gyr, so that a strong stellar bar forms in the initially axisymmetric disc, and then release the gaseous component and evolve it for a further 400 Myr to allow it to reach equilibrium. Other parameters of the model remain the same as in Chapter 4.

The CMZ in this model is shown in Figure 5.4. Overall the gas flow in the centre is similar to the previous model. The gas still forms an ellipitcal central disc where the gas follows the x_2 orbits in the barred potential. The orientation of this disc rotates with the bar. From a side on view it is clear that the gas becomes more tilted in this noisy potential, but this tilting angle remains constant over the radius of the CMZ. Even in a noisier potential the gas still does not form a twisted ring.

Figure 5.5 shows the orientation of the normal to the nuclear disc $\hat{\mathbf{n}}$ relative to the galactic plane during the evolution of the simulation. Again the two methods for finding $\hat{\mathbf{n}}$ closely agree. The magnitude of the tilt in the noisier potential is larger than in the reference model. As the vertical fluctuations in the potential are responsible for disturbing gas out of the galactic plane this is unsurprising. The orientation of the tilt precesses extremely regularly in the opposite direction to the circulation of the gas, with $\dot{\phi} < 0$, and a period of $T_z = 125$ Myr. For reference the bar period of the model is $\sim 175\,\mathrm{Myr}$.

5.3.4 Is the gas following ballistic trajectories?

We would not expect the inner gravitational potential of the model or the Galaxy to be perfectly symmetric about $z = 0$, therefore it seems likely that the CMZ would be tilted slightly out of the plane by gravitational torques. However it is not immediately

clear why the tilt of the central disc of gas should precess. In our simulations there could be two mechanisms, either the tilt is due to some hydrodynamical effect, or the influence of the gravitational potential. The x_2 disc is constantly accreting gas from the dust lane shocks, and if the angular momentum of the accreted gas is misaligned with that of the central gas then it would reorientate the total angular momentum of the CMZ. Alternatively, the gas in the x_2 disc could be closely following ballistic trajectories, with the precession of the gas purely a feature of the local potential.

As the excursions in the vertical direction are small, we can treat them using the first order expansion of epicyclic theory. The vertical oscillation frequency is

$$\nu^2 = \left(\frac{\partial^2 \Phi}{\partial z^2}\right)_{R_g,\, z=0} \tag{5.6}$$

where Φ is the gravitational potential and the derivative is evaluated at the guiding centre radius of the orbit at $z = 0$ (Binney & Tremaine, 2008). If the particle has an orbital frequency $\Omega = \sqrt{R\partial_R \Phi}$, the orbit will be in an inclined plane that rotates with a vertical precession rate $\Omega_n = \Omega - \nu$. In the potential of a flattened density distribution such as the galactic bulge $\nu > \Omega$, so $\Omega_n < 0$, and the normal to the plane of the orbit rotates in the opposite direction to the orbital motion.

Figure 5.5 shows the orbital and vertical frequencies in the $z = 0$ plane in the potential of the simulation. The frequencies have been calculated from an azimuthally averaged snapshot of the N-body potential taken from the start of the gas evolution. As expected $\nu > \Omega$ due to the flattening of the potential. The time period of the precession rate of an inclined orbit in the potential, $T_n = 2\pi/\Omega_n$ is shown in Figure 5.7. The period of rotation in the region of the CMZ is almost exactly equal to the time period of precession of the CMZ in the simulation, so it seems extremely likely that this precession is purely the result of the gas closely following ballistic orbits. T_n is relatively independent of radius, as a result the vertical orientation of the CMZ

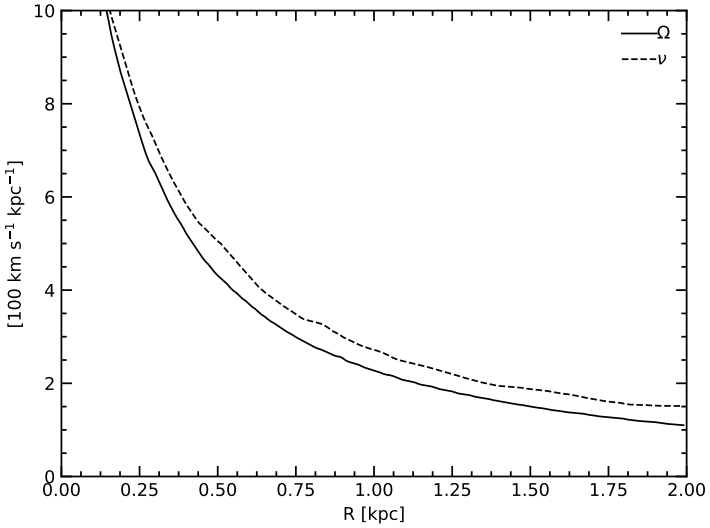

Figure 5.6: The orbit frequency Ω (solid line) and the vertical epicyclic frequency ν (black line) calculated from the azimuthally averaged potential in the inner regions of the low resolution model. Due to the flattened profile of the bulge, $\nu > \Omega$. As a result, the plane of orbits with small vertical excursions will precess with $\Omega_n = \Omega - \nu < 0$.

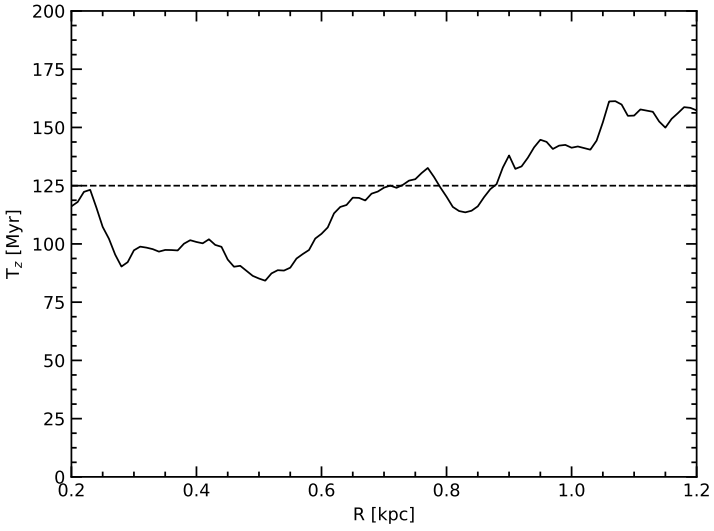

Figure 5.7: The time period of precession $T_n = 2\pi/\Omega_n$ of the plane of an inclined orbit in the central regions of the potential. The horizontal dashed line shows the precession period of the CMZ of the hydrodynamical simulation in the potential, 125 Myr. It is almost exactly equal to the period predicted by epicyclic theory in this region.

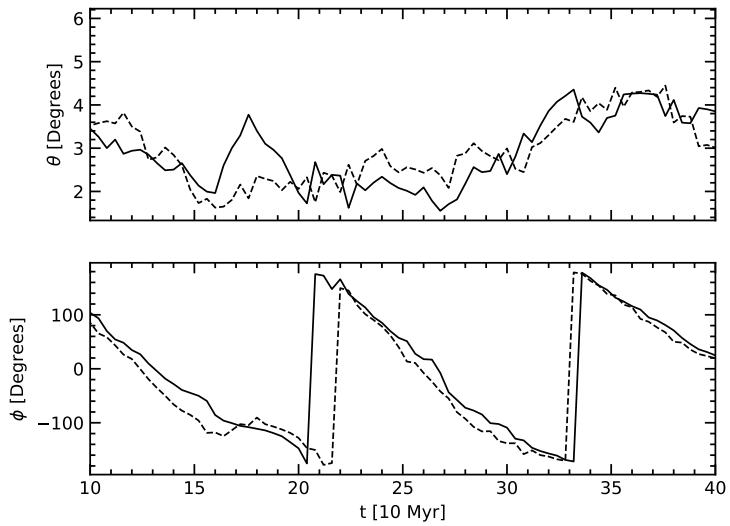

Figure 5.8: The angles defining the orientation of $\hat{\mathbf{n}}$ of the disc of test particles during the evolution of the simulation. *Black solid line:* calculated from diagonalising $\mathbf{I}$. *Black dotted line:* calculated by minimising $\sum_i \hat{\mathbf{n}} \cdot (\rho_i \mathbf{v}_i)$.

does not become smeared out due to a large differential rate of precession between the inner and outer gas.

To confirm this hypothesis we can examine the behaviour of ballistic test particles in the full potential. The test particles are initially in a small circular disc, with a radius of 1 kpc, initially on circular orbits. The disc is razor thin and aligned with $z = 0$. We then allow the test particles to evolve in the live N-body potential, as used in the hydrodynamic simulation. We evolve the test particles for the same period of time as the gas, 400 Myr.

Figure 5.8 shows the orientation of the test particles as given by θ and ϕ which define the normal to the disc, as previously described. The disc of test particles also tilts, in almost exactly the same manner as the CMZ in the full hydrodynamic simulation. This confirms that the tilting and precession that we observe in the gas is purely a gravitational effect. Flow of gas down the dust lane shocks and onto the CMZ seems to have negligible effect on the orientation of the gas, as do vertical

pressure forces.

5.4 Discussion

Our results suggest a simple explanation for the currently observed configuration of the gas in the galactic centre. The gas is closely following the x_2 orbits, and due to the flattening of the central gravitational potential the frequency of vertical oscillations ν about the guiding centre of the orbits is higher than the orbital frequency Ω, so the point on the orbit at which the gas reaches a maximum height rotates around the galactic centre in the opposite direction of the rotation of the gas. As a result, at any particular instant in time the central gas is unlikely to be aligned with the outer gas, as is the case in the galactic centre. In fact, in our models we find that the inner gas is never aligned to within more than a few degrees, so it would be more surprising to find that the CMZ was perfectly in the plane of the Galaxy.

It may seem surprising that the bar has no effect on the precession rate of the gas, but the bar of the model is close to vertically symmetric, so it exerts no large scale out-of-plane torque on the gas. The extent and velocity structure of the x_2 orbits of the potential are a function of the large scale distribution of the bar, but the vertical dynamics of the gas are affected by only the local potential.

Are the results of these simulations applicable to the CMZ of the real Galaxy? Our simulations lack many physical ingredients such as chemistry, star formation and magnetic fields, that may affect the vertical distribution of the galactic centre gas. Our results are only applicable if it is indeed the gravitational potential of the inner Galaxy that has the dominant effect on the dynamics of the gas on the scales we consider here.

We have entirely neglected self gravity in these simulations, however this is a reasonable approximation given the ISM only comprises some 1% of the total mass

within the central kiloparsec of the Milky Way (Launhardt et al., 2002; Ferrière et al., 2007). The most likely effect of self gravity would be to confine the gas in the CMZ to a thinner disc, but the stellar mass distribution would still dominate the dynamics of the gas at scales greater than a few parsecs.

Sormani et al. (2018b) presented three dimensional hydrodynamic simulations in a barred model of the Milky Way's potential, using the moving mesh code AREPO. Their model included a time dependent chemical network that tracked the chemistry of the ISM, with a realistic heating and cooling function. The potential was the same as used in the isothermal simulations of Ridley et al. (2017). The surface density of the gas in the two models on scales larger than $\sim 10\,\mathrm{pc}$ are broadly similar, indicating that the chemistry of the ISM predominantly affects the small scale structure of the gas.

Star formation will likely have a similar effect on the gas, altering the small scale structure of the ISM significantly, and possibly throwing material out of the plane. Seo & Kim (2013) presented a study of star formation in nuclear rings using hydrodynamic simulations in a barred potential with a realistic model of star formation feedback. In their simulation the stellar feedback does indeed produce a patchy and clumpy ISM, but overall the gas remains well confined to the x_2 orbits in the galactic centre. Supernova feedback may indeed provide a source of off-axis angular momentum that could initially tilt the CMZ, but once tilted the gas will still follow ballistic orbits, and precess in the manner we have described here.

The magnetic field in the galactic centre is poorly understood. Kruijssen et al. (2015) argued on the basis of equipartition that magnetic forces are likely not strong enough to significantly affect the dynamics of the gas. Our results suggest that they are not needed to explain the behaviour of the CMZ, but further work is needed to fully understand this topic.

Overall it seems that the dynamics of gas in the centre of the galaxy on 100 pc

scales will be dominated by gravity, hence we would expect the tilted CMZ to behave in a similar manner to our simulations.

The bulge in our N-body models is the main contributor to mass in the central kiloparsec. While it is strongly flattened in the disc-growth stage of setting up the initial conditions (Section 2.5), the inner mass distribution will not be as flattened as the inner stellar density of the Milky Way, which contains a several hundred parsec nuclear stellar disc (Launhardt et al., 2002) that has no counterpart in our simulations. Therefore in the real Milky Way it is likely that the precession rate $\Omega_n = \Omega - \nu$ would be greater, as ν would be larger in a more flattened potential.

5.5 Conclusions

In recent years there has been increased interest in the vertical structure of gas in the CMZ of the Milky Way. Proposed explanations include a twisted elliptical orbit oscillating twice vertically during every orbital period, an open stream, or a tilted disc. In this chapter we have shown that in realistic three dimensional simulations of gas in a live N-body potential the central disc of gas tilts almost as a solid body. Once tilted out of the plane, the normal to the disc precesses around the z-axis in the opposite direction to the circulation of the gas.

We have shown that the gas is behaving almost exactly as ballistic test particles. The precession of the tilt is simply a consequence of the difference between the orbital frequency and the vertical epicyclic frequency. The vertical response of the gas is purely a function of the local gravitational potential. Surprisingly it appears that pressure forces and the rotation of the bar have little effect on the vertical dynamics of the gas.

In our reference model we do not observe tilting of the CMZ on the scale that we see in the Milky Way. We can reproduce this using a lower resolution N-body

potential, but our simulations may also be lacking some key ingredient that initially drives gas out of the plane, such as stellar feedback or magnetic fields.

Our results suggest that a configuration of the inner gas such as that currently observed in the Milky Way is relatively likely. However we do not offer an explanation for the large scale tilt of the gas outside the CMZ. There are currently no convincing proposed explanations for this phenomenon, which remains an important avenue for future work.

Chapter 6

Conclusions and Future Work

This thesis is a study of several aspects of gas flow in barred potentials using a variety of models. In Chapter 3 we presented a simple two dimensional hydrodynamic simulation of gas flow in a rigid model of the potential of the Milky Way, and showed that many features of observations of the CMZ of the Galaxy could be explained as a natural consequence of the barred potential of the inner Milky Way. In the model a small nuclear disc of high density gas formed from material driven inwards by shocks at the tips of the bar. This disc contained two nuclear spiral arms; kinematic density waves produced by the crowding of streamlines in the gas. In projection, these two arms appeared as "streams" of high density gas crossing the width of the CMZ. We also related other features, such as the asymmetry, molecular gas complexes, and high velocity features, to aspects of our model.

In Chapter 4 we examined the behaviour of gas in a more realistic model of the Galactic potential using a three dimensional hydrodynamical simulation in a live N-body potential. We investigated if, as previous authors have found, the fluctuations in a time dependent potential would be strong enough to disturb the gas from equilibrium. We found that in our carefully constructed models this was not the case, but also found that the gas flow was extremely sensitive to the exact form of the

components of the potential, and not just the approximate strength and scale lengths of each component. We found that two dimensional rigid bar models could reproduce most of the features of the live simulation, but that slight differences in the shape and position of the dust lane shocks, and mismatches between gas flow in the out disc limited the usefulness of automated fitting methods.

Finally, we turned to the vertical dynamics of gas in the Galactic center. We reviewed our current knowledge of the three dimensional distribution of the CMZ, and the current theoretical explanations. In our realistic simulations we found that the gas closely follows the ballistic orbits, and when disturbed vertically the central gas disc tilts as a solid body, with the orientation of the tilt precessing as a natural consequence of epicycle theory. However our models did not suggest an explanation for the observed magnitude of the tilt of gas in the inner region.

6.1 Future Work

There are two main avenues for future work. The first lies in improving the realism of the simulations. The simulations presented in this thesis are comparatively simple. We model the gas as single phase, isothermal, and have no star formation, self-gravity, or magnetic fields. We slightly improve upon the rigid potential of Chapter 3 with a more realistic live N-body potential in Chapters 4 and 5. The dynamical effects of the barred potential of the Milky Way on the gas flow are by now well understood. To understand the importance of the missing ingredients it is necessary to include them in the model. By slowly turning on each separate piece of physics in turn one can examine the effect on the gas flow, and relate the effects to observations.

The other avenue is to attempt to use the simulations as they are to learn as much as possible about the inner Galaxy within the limitations of the models. The parameters of the bar are not well tied down, and gas flow models are useful tools to

probe the inner potential of the Milky Way. With current technology, two dimensional hydrodynamic models in rigid potentials can be run for relatively low cost. Despite this, the almost intractable parameter space of such models requires either searching a limited subset of parameters or the use of automated fitting methods. We have shown that the SMHD of Sormani & Magorrian (2015), while still a promising candidate for automated exploration of these parameter spaces, requires some improvement before it can be properly used.

Appendix A

A Resolution Test

This appendix presents a resolution test of the results of Chapter 4.

A.1 A higher resolution N-body model

Parameter	Value	Description
M_t	$1.43 \times 10^{12}\mathrm{M}_\odot$	Total mass
$M_\star$	$5.43 \times 10^{10}\mathrm{M}_\odot$	Total baryonic mass
M_h	$1.37 \times 10^{12}\mathrm{M}_\odot$	Halo mass
a_h	$37.8\,\mathrm{kpc}$	Halo scale length
M_b	$5 \times 10^{9}\mathrm{M}_\odot$	Bulge mass
a_b	$200\,\mathrm{pc}$	Bulge scale length
M_d	$4.93 \times 10^{10}\mathrm{M}_\odot$	Disc mass
Σ_d	$1.25 \times 10^{10}\mathrm{M}_\odot\,\mathrm{kpc}^{-2}$	Central disc surface density
R_d	$2.5\,\mathrm{kpc}$	Disc scale length
z_d	$300\,\mathrm{pc}$	Disc scale height
N_t	2×10^6	Total number of particles
N_h	8×10^5	Number of halo particles
N_b	4×10^5	Number of bulge particles
N_d	1.6×10^6	Number of disc particles

Table A.1: Parameters of the higher resolution model.

There are two sources of time dependence in an N-body potential, the time variation of macroscopic properties of the model, and Poisson noise as a result of low particle numbers. In this appendix we present a higher resolution N-body simulation

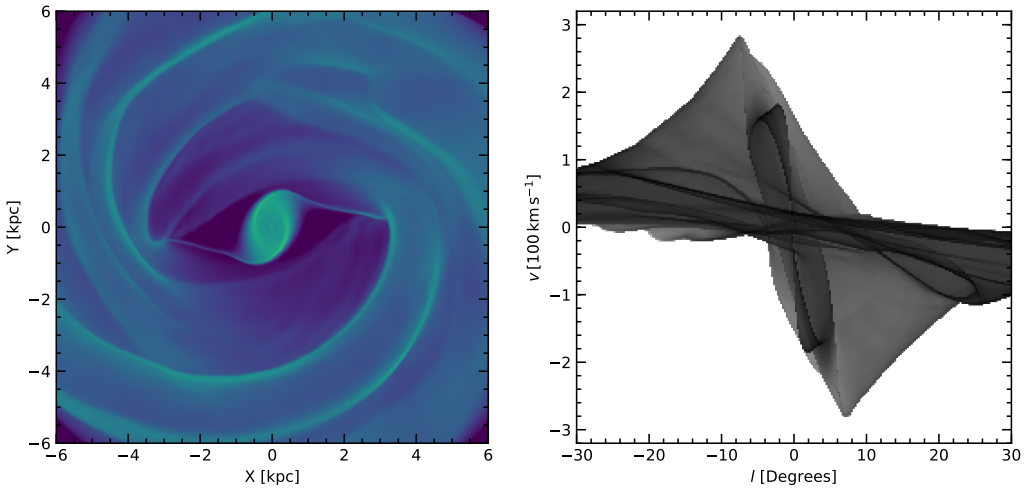

Figure A.1: The final state of the gas in the higher resolution N-body model, and a mock (l, v) plot created from the model.

that we use to test that the results of Chapter 4 are not limited by the latter.

Noise in the central regions of the model is produced mostly by the disc particles, which are more massive than the particles that represent the inner bulge. We constructed an additional model, with identical realisations of the bulge and halo, but twice the number of disc particles. The structural parameters of this model are summarised in Table A.1, and are identical to the reference model. Nonetheless, due to the stochastic nature of N-body simulations, the final state of the model could vary significantly to the reference model, despite their similar initial conditions.

We follow the exactly same procedure as in Sections 4.2 and 4.3. After constructing the initial conditions we evolve the pure N-body components using GROMMET, for a total of 2 Gyr. During this time a strong rotating bar forms in the centre of the galaxy. The gas is evolved from 2 Gyr to 2.4 Gyr. The final state of the gas, and a mock (l, v) plot created from the simulation, is shown in Figure A.1.

We then proceed to repeat the same fitting test as in Section 4.5. We construct three types of rigid models, the first in which the potential is a frozen snapshot of the N-body potential, the second in which the potential is a filtered N-body potential consisting of just the monopole and quadrupole moments, and the third in which the po-

tential consists of the monopole of the N-body potential plus an analytic quadrupole of the form of Equation 4.8, fit to the N-body quadrupole. For these three potential models, we vary Ω_p, the pattern speed, and for the two monopole + quadrupole potentials we also vary the strength $\tilde{A}$ and scale length $\tilde{r}$ of the quadrupole.

Qualitatively the results are the same as for the reference model; Adjusting the pattern speed affects the gas flow globally as it changes the positions of the major resonances with the bar, varying the amplitude of the quadrupole most strongly effects the envelope of emission the (l, v) plane, and varying the scalelength of the quadrupole influences gas flow in the region outside the bar (see Section 4.5, Sormani et al. (2015c) for a full discussion). We then compare the rigid models to the live high resolution simulation using the SMHD.

The results of these comparisons are shown in Figures A.2, A.3, A.4, A.5 and A.6. We observe that the behaviour of the SMHD is broadly similar to in our reference model. It behaves well when the potential of the rigid simulation is a perfect match, but less successfully for both our monopole + quadrupole potentials. We find that the SMHD is still broadly degenerate, and more strongly able to constrain $\tilde{A}$ than $\tilde{r}$. Thus we can be confident that the results of our reference model are not limited by Poisson fluctuations in the potential.

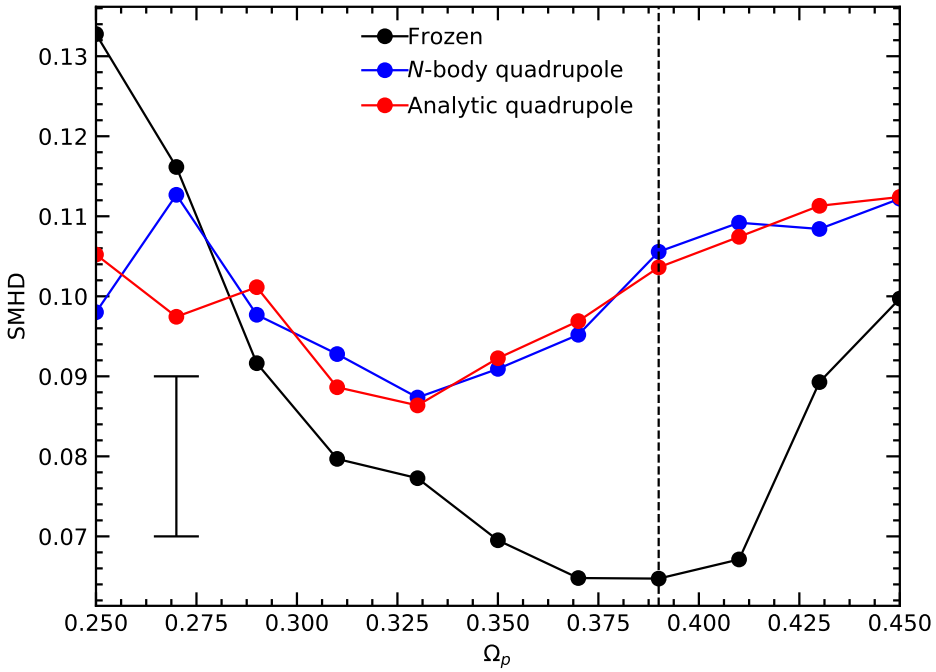

Figure A.2: The SMHD distance between the live high resolution N-body model and simulations in the three model potentials a function of Ω_p, from 25 to 45 $\mathrm{km\,s^{-1}\,kpc^{-1}}$. The SMHD for the frozen N-body potential (black line) shows a clear minimum at the correct pattern speed, $\Omega_p = 39\ \mathrm{km\,s^{-1}\,kpc^{-1}}$ (dashed vertical line), but the SMHD for the other models (red and blue lines) is more noisy and shows more of a minimum around $32\,\mathrm{km\,s^{-1}}$. A typical error bar is in the bottom left.

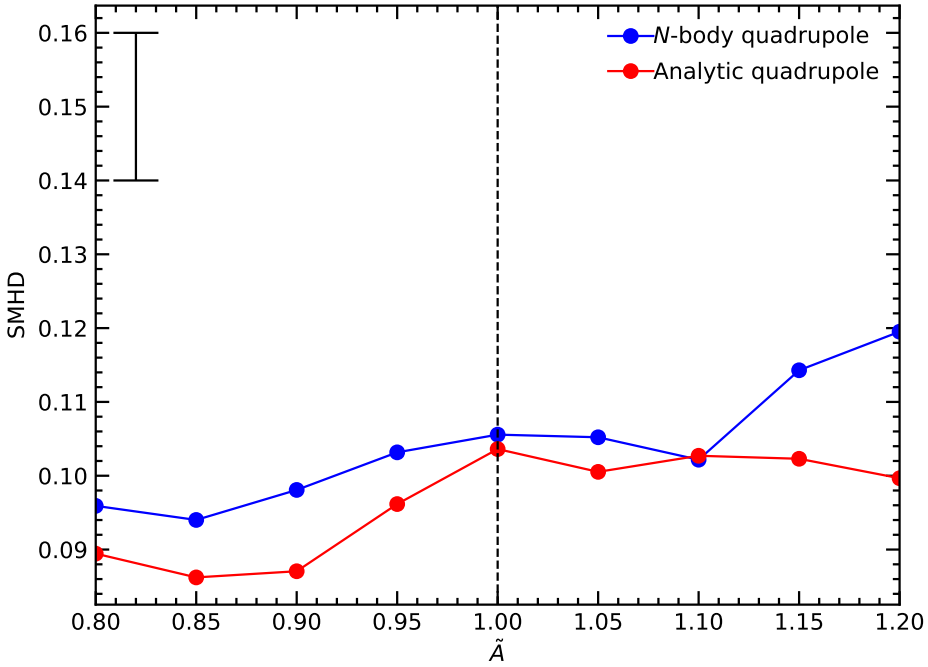

Figure A.3: The SMHD distance between the live N-body model and rigid simulations as a function of the strength of the quadrupole, $\tilde{A}$, from 0.8 to 1.2. The variation of the SMHD with $\tilde{A}$ is less strong than in our reference model.

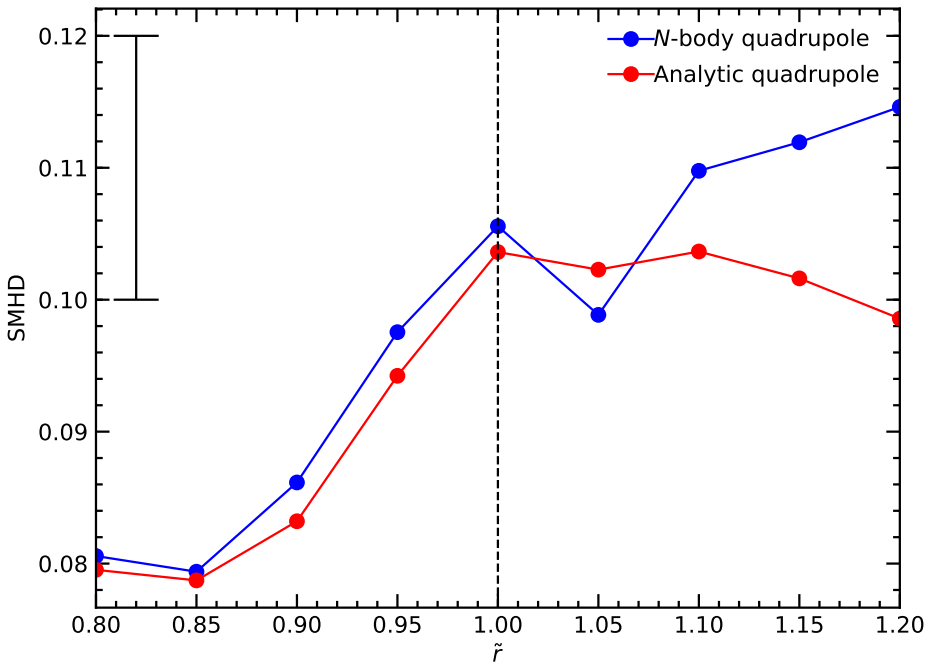

Figure A.4: The SMHD distance between the live N-body model and rigid simulations as a function of the scale length of the quadrupole, $\tilde{r}$, from 0.8 to 1.2. For both models the SMHD shows a clear bias for lower scale lengths.

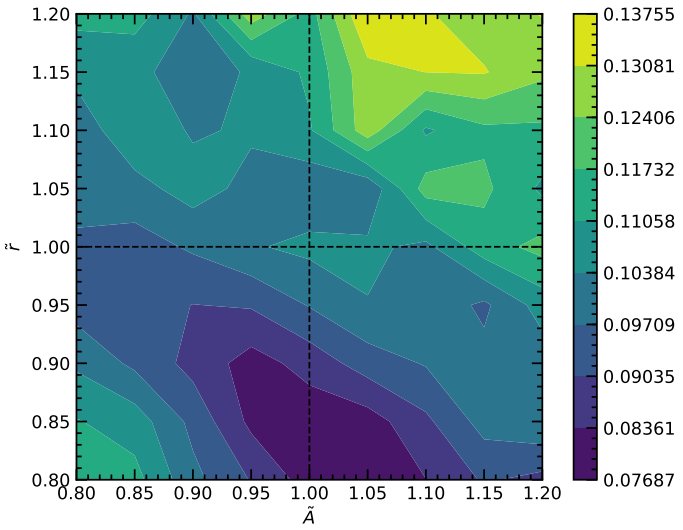

Figure A.5: Contours of SMHD distance between the live N-body simulation and a grid of simulations with a potential consisting of the N-body monopole and quadrupole, where the strength and scale length of the quadrupole have been varied by two parameters $\tilde{r}$ and $\tilde{A}$. There is a strong bias for low $\tilde{r}$, and some degeneracy between the two parameters.

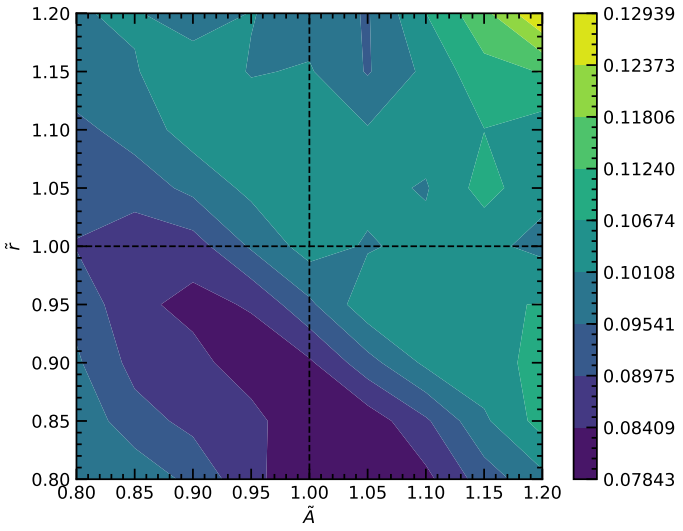

Figure A.6: As Figure 4.32, but for the N-body monopole + analytic quadrupole potential. The SMHD behaves similarly as for the filtered N-body potential.

Bibliography

Ann, H. B. & Thakur, P., 2005. Formation of Nuclear Spirals in Barred Galaxies. *ApJ*, **620**, 197–209.

Athanassoula, E., 1992. The existence and shapes of dust lanes in galactic bars. *MNRAS*, **259**, 345–364.

Bally, J., Aguirre, J., Battersby, C., Bradley, E. T., Cyganowski, C. et al., 2010. The Bolocam Galactic Plane Survey: $\lambda = 1.1$ and 0.35 mm Dust Continuum Emission in the Galactic Center Region. *ApJ*, **721**, 137–163.

Bally, J., Stark, A. A., Wilson, R. W. & Henkel, C., 1988. Galactic center molecular clouds. II - Distribution and kinematics. *ApJ*, **324**, 223–247.

Battersby, C., Keto, E., Zhang, Q., Longmore, S. N., Kruijssen, J. M. D. et al., 2016. A Brief Update on the CMZoom Survey. *ArXiv e-prints: 1610.05805*.

Bertram, E., Glover, S. C. O., Clark, P. C. & Klessen, R. S., 2015. Star formation efficiencies of molecular clouds in a galactic centre environment. *MNRAS*, **451**, 3679–3692.

Binney, J., Gerhard, O. & Spergel, D., 1997. The photometric structure of the inner Galaxy. *MNRAS*, **288**, 365–374.

Binney, J., Gerhard, O. E., Stark, A. A., Bally, J. & Uchida, K. I., 1991. Understanding the kinematics of Galactic centre gas. *MNRAS*, **252**, 210–218.

Binney, J. & Merrifield, M., 1998. *Galactic Astronomy*. Princeton University Press.

Binney, J. & Tremaine, S., 2008. *Galactic Dynamics: Second Edition*. Princeton University Press.

Bissantz, N. & Gerhard, O., 2002. Spiral arms, bar shape and bulge microlensing in the Milky Way. *MNRAS*, **330**, 591–608.

Bland-Hawthorn, J. & Gerhard, O., 2016. The Galaxy in Context: Structural, Kinematic, and Integrated Properties. *ARA&A*, **54**, 529–596.

Blitz, L. & Spergel, D. N., 1991. Direct evidence for a bar at the Galactic center. *ApJ*, **379**, 631–638.

Burton, W. B., Elmegreen, B. G. & Genzel, R., eds., 1992. *The galactic interstellar medium*. Springer-Verlag.

Burton, W. B. & Liszt, H. S., 1978. The gas distribution in the central region of the Galaxy. I - Atomic hydrogen. *ApJ*, **225**, 815–842.

Contopoulos, G. & Papayannopoulos, T., 1980. Orbits in weak and strong bars. *A&A*, **92**, 33–46.

Courant, R., Friedrichs, K. & Lewy, H., 1928. Über die partiellen Differenzengleichungen der mathematischen Physik. *Mathematische Annalen*, **100**, 32–74.

Cowie, L. L., 1980. On the dynamics of agglomerating ensembles of clouds. *ApJ*, **236**, 868–879.

Crocker, R. M., Jones, D. I., Melia, F., Ott, J. & Protheroe, R. J., 2010. A lower limit of 50 microgauss for the magnetic field near the Galactic Centre. *Nature*, **463**, 65–67.

Dame, T. M., Hartmann, D. & Thaddeus, P., 2001. The Milky Way in Molecular Clouds: A New Complete CO Survey. *ApJ*, **547**, 792–813.

de Vaucouleurs, G., 1964. Interpretation of velocity distribution of the inner regions of the Galaxy. In F. J. Kerr, ed., *The Galaxy and the Magellanic Clouds*, vol. 20 of *IAU Symposium*, 195.

Dehnen, W., 1999a. Approximating Stellar Orbits: Improving on Epicycle Theory. *AJ*, **118**, 1190–1200.

Dehnen, W., 1999b. Simple Distribution Functions for Stellar Disks. *AJ*, **118**, 1201–1208.

Dobbs, C. L., Glover, S. C. O., Clark, P. C. & Klessen, R. S., 2008. The ISM in spiral galaxies: can cooling in spiral shocks produce molecular clouds? *MNRAS*, **389**, 1097–1110.

Eddington, A. S., 1916. The distribution of stars in globular clusters. *MNRAS*, **76**, 572–585.

ESA, ed., 1997. *The HIPPARCOS and TYCHO catalogues. Astrometric and photometric star catalogues derived from the ESA HIPPARCOS Space Astrometry Mission*, vol. 1200 of *ESA Special Publication*.

Ferrière, K., Gillard, W. & Jean, P., 2007. Spatial distribution of interstellar gas in the innermost 3 kpc of our galaxy. *A&A*, **467**, 611–627.

Field, G. B., 1965. Thermal Instability. *ApJ*, **142**, 531.

Fragkoudi, F., Athanassoula, E. & Bosma, A., 2016. Constraining the dark matter content of NGC 1291 using hydrodynamic gas response simulations. *ArXiv e-prints 1611.09386*.

Fux, R., 1999. 3D self-consistent N-body barred models of the Milky Way. II. Gas dynamics. *A&A*, **345**, 787–812.

Gaia Collaboration, Prusti, T., de Bruijne, J. H. J., Brown, A. G. A., Vallenari, A., Babusiaux, C., Bailer-Jones, C. A. L., Bastian, U., Biermann, M., Evans, D. W. & et al., 2016. The Gaia mission. *A&A*, **595**, A1.

Gilmore, G. & Reid, N., 1983. New light on faint stars. III - Galactic structure towards the South Pole and the Galactic thick disc. *MNRAS*, **202**, 1025–1047.

Gottlieb, S. & Shu, C. W., 1998. Total variation diminishing Runge-Kutta schemes. *Mathematics of Computation*, **67**, 73–85.

Hausdorff, F., 1949. *Grundzüge der Mengenlehre*. Chelsea. URL `https://books.google.co.uk/books?id=tw8RnQAACAAJ`.

Heiligman, G. M., 1987. Molecular gas within 2 deg of the Galactic center. I - Survey of (C-13)O emission. *ApJ*, **314**, 747–765.

Henshaw, J. D., Longmore, S. N. & Kruijssen, J. M. D., 2016a. Seeding the Galactic Centre gas stream: gravitational instabilities set the initial conditions for the formation of protocluster clouds. *MNRAS*, **463**, L122–L126.

Henshaw, J. D., Longmore, S. N., Kruijssen, J. M. D., Davies, B., Bally, J. et al., 2016b. Molecular gas kinematics within the central 250 pc of the Milky Way. *MNRAS*, **457**, 2675–2702.

Hernquist, L., 1990. An analytical model for spherical galaxies and bulges. *ApJ*, **356**, 359–364.

Hernquist, L., 1993. N-body realizations of compound galaxies. *ApJS*, **86**, 389–400.

Hockney, R. W. & Eastwood, J. W., 1988. *Computer simulation using particles*.

James, R. A., 1977. The Solution of Poisson's Equation for Isolated Source Distributions. *Journal of Computational Physics*, **25**, 71–93.

Jenkins, A. & Binney, J., 1994. Dynamics of Gas Near the Galactic Centre. *MNRAS*, **270**, 703.

Kalberla, P. M. W., Burton, W. B., Hartmann, D., Arnal, E. M., Bajaja, E., Morras, R. & Pöppel, W. G. L., 2005. The Leiden/Argentine/Bonn (LAB) Survey of Galactic HI. Final data release of the combined LDS and IAR surveys with improved stray-radiation corrections. *A&A*, **440**, 775–782.

Kennicutt, Jr., R. C., 1998. Star Formation in Galaxies Along the Hubble Sequence. *ARA&A*, **36**, 189–232.

Kim, W.-T., Kim, Y. & Kim, J.-G., 2014. Nature of the Wiggle Instability of Galactic Spiral Shocks. *ApJ*, **789**, 68.

Kim, W.-T., Seo, W.-Y., Stone, J. M., Yoon, D. & Teuben, P. J., 2012. Central Regions of Barred Galaxies: Two-dimensional Non-self-gravitating Hydrodynamic Simulations. *ApJ*, **747**, 60.

Kruijssen, J. M. D., Dale, J. E. & Longmore, S. N., 2015. The dynamical evolution of molecular clouds near the Galactic Centre - I. Orbital structure and evolutionary timeline. *MNRAS*, **447**, 1059–1079.

Kruijssen, J. M. D., Longmore, S. N., Elmegreen, B. G., Murray, N., Bally, J., Testi, L. & Kennicutt, R. C., 2014. What controls star formation in the central 500 pc of the Galaxy? *MNRAS*, **440**, 3370–3391.

Kuijken, K. & Dubinski, J., 1995. Nearly Self-Consistent Disc / Bulge / Halo Models for Galaxies. *MNRAS*, **277**, 1341.

Kunder, A., Kordopatis, G., Steinmetz, M., Zwitter, T., McMillan, P. J. et al., 2017. The Radial Velocity Experiment (RAVE): Fifth Data Release. *AJ*, **153**, 75.

Kuno, N., Nakanishi, K., Sorai, K. & Shibatsuka, T., 2008. Central Spiral Structure of Molecular Gas in Maffei 2. *Publications of the Astronomical Society of Japan*, **60**, 475–485.

Langer, W. D., Velusamy, T., Morris, M. R., Goldsmith, P. F. & Pineda, J. L., 2017. Kinematics and properties of the Central Molecular Zone as probed with [C II]. *ArXiv e-prints*.

Launhardt, R., Zylka, R. & Mezger, P. G., 2002. The nuclear bulge of the Galaxy. III. Large-scale physical characteristics of stars and interstellar matter. *A&A*, **384**, 112–139.

Lax, P. D., 1954. Weak solutions of nonlinear hyperbolic equations and their numerical computation. *Communications on Pure and Applied Mathematics*, **7**(1), 159–193. URL `https://onlinelibrary.wiley.com/doi/abs/10.1002/cpa.3160070112`.

Li, Z., Gerhard, O., Shen, J., Portail, M. & Wegg, C., 2016. Gas Dynamics in the Milky Way: A Low Pattern Speed Model. *ApJ*, **824**, 13.

Li, Z., Shen, J. & Kim, W.-T., 2015. Hydrodynamical Simulations of Nuclear Rings in Barred Galaxies. *ApJ*, **806**, 150.

Lindqvist, M., Habing, H. J. & Winnberg, A., 1992. OH/IR stars close to the Galactic Centre. II - Their spatial and kinematic properties and the mass distribution within 5-100 PC from the galactic centre. *A&A*, **259**, 118–127.

Lis, D. C. & Menten, K. M., 1998. Infrared Space Observatory Long Wavelength Spectrometer Observations of a Cold Giant Molecular Cloud Core near the Galactic Center. *ApJ*, **507**, 794–804.

Liszt, H. S. & Burton, W. B., 1978. The gas distribution in the central region of the Galaxy. II - Carbon monoxide. *ApJ*, **226**, 790–816.

Liszt, H. S. & Burton, W. B., 1980. The gas distribution in the central region of the Galaxy. III - A barlike model of the inner-Galaxy gas based on improved H I data. *ApJ*, **236**, 779–797.

Longmore, S. N., Bally, J., Testi, L., Purcell, C. R., Walsh, A. J., Bressert, E., Pestalozzi, M., Molinari, S., Ott, J., Cortese, L., Battersby, C., Murray, N., Lee, E., Kruijssen, J. M. D., Schisano, E. & Elia, D., 2013a. Variations in the Galactic star formation rate and density thresholds for star formation. *MNRAS*, **429**, 987–1000.

Longmore, S. N., Kruijssen, J. M. D., Bally, J., Ott, J., Testi, L., Rathborne, J., Bastian, N., Bressert, E., Molinari, S., Battersby, C. & Walsh, A. J., 2013b. Candidate super star cluster progenitor gas clouds possibly triggered by close passage to Sgr A*. *MNRAS*, **433**, L15–L19.

Longmore, S. N., Rathborne, J., Bastian, N., Alves, J., Ascenso, J. et al., 2012. G0.253 + 0.016: A Molecular Cloud Progenitor of an Arches-like Cluster. *ApJ*, **746**, 117.

Longmore, S. N., Walsh, A. J., Purcell, C. R., Burke, D. J., Henshaw, J. et al., 2017. H2O Southern Galactic Plane Survey (HOPS): Paper III - Properties of Dense Molecular Gas across the Inner Milky Way. *ArXiv e-prints*.

Magorrian, J., 2007. GROMMET: an N-body code for high-resolution simulations of individual galaxies. *MNRAS*, **381**, 1663–1671.

Majewski, S. R., Schiavon, R. P., Frinchaboy, P. M., Allende Prieto, C., Barkhouser, R. et al., 2017. The Apache Point Observatory Galactic Evolution Experiment (APOGEE). *AJ*, **154**, 94.

Martini, P., Regan, M. W., Mulchaey, J. S. & Pogge, R. W., 2003a. Circumnuclear Dust in Nearby Active and Inactive Galaxies. I. Data. *ApJS*, **146**, 353–406.

Martini, P., Regan, M. W., Mulchaey, J. S. & Pogge, R. W., 2003b. Circumnuclear Dust in Nearby Active and Inactive Galaxies. II. Bars, Nuclear Spirals, and the Fueling of Active Galactic Nuclei. *ApJ*, **589**, 774–782.

McGinn, M. T., Sellgren, K., Becklin, E. E. & Hall, D. N. B., 1989. Stellar kinematics in the Galactic center. *ApJ*, **338**, 824–840.

McMillan, P. J., 2017. The mass distribution and gravitational potential of the Milky Way. *MNRAS*, **465**, 76–94.

McMillan, P. J. & Dehnen, W., 2007. Initial conditions for disc galaxies. *MNRAS*, **378**, 541–550.

Mignone, A., Bodo, G., Massaglia, S., Matsakos, T., Tesileanu, O., Zanni, C. & Ferrari, A., 2007. PLUTO: A Numerical Code for Computational Astrophysics. *ApJS*, **170**, 228–242.

Molinari, S., Bally, J., Noriega-Crespo, A., Compiègne, M., Bernard, J. P. et al., 2011. A 100 pc Elliptical and Twisted Ring of Cold and Dense Molecular Clouds Revealed by Herschel Around the Galactic Center. *ApJ*, **735**, L33.

Nagayama, T., Omodaka, T., Handa, T., Iahak, H. B. H., Sawada, T., Miyaji, T. & Koyama, Y., 2007. A Complete Survey of the Central Molecular Zone in NH_3. *Publications of the Astronomical Society of Japan*, **59**, 869–887.

Navarro, J. F., Frenk, C. S. & White, S. D. M., 1996. The Structure of Cold Dark Matter

Halos. *ApJ*, **462**, 563.

Oka, T., Nagai, M., Kamegai, K., Tanaka, K. & Kuboi, N., 2007. A CO J = 3-2 Survey of the Galactic Center. *Publications of the Astronomical Society of Japan*, **59**, 15–23.

Oort, J. H., 1977. The galactic center. *ARA&A*, **15**, 295–362.

Oort, J. H., Kerr, F. J. & Westerhout, G., 1958. The galactic system as a spiral nebula (Council Note). *MNRAS*, **118**, 379.

Pfenniger, D. & Friedli, D., 1993. Computational issues connected with 3D N-body simulations. *A&A*, **270**, 561–572.

Purcell, C. R., Longmore, S. N., Walsh, A. J., Whiting, M. T., Breen, S. L. et al., 2012. The H_2O Southern Galactic Plane Survey: NH_3 (1,1) and (2,2) catalogues. *MNRAS*, **426**, 1972–1991.

Rathborne, J. M., Longmore, S. N., Jackson, J. M., Alves, J. F., Bally, J., Bastian, N., Contreras, Y., Foster, J. B., Garay, G., Kruijssen, J. M. D., Testi, L. & Walsh, A. J., 2015. A Cluster in the Making: ALMA Reveals the Initial Conditions for High-mass Cluster Formation. *ApJ*, **802**, 125.

Reid, M. J. & Brunthaler, A., 2004. The Proper Motion of Sagittarius A*. II. The Mass of Sagittarius A*. *ApJ*, **616**, 872–884.

Reid, M. J., Menten, K. M., Zheng, X. W., Brunthaler, A. & Xu, Y., 2009. A Trigonometric Parallax of Sgr B2. *ApJ*, **705**, 1548–1553.

Ridley, M. G. L., Sormani, M. C., Tress, R. G., Magorrian, J. & Klessen, R. S., 2017. Nuclear spirals in the inner Milky Way. *MNRAS*, **469**, 2251–2262.

Roberts, W. W., 1969. Large-Scale Shock Formation in Spiral Galaxies and its Implications on Star Formation. *ApJ*, **158**, 123.

Rodriguez-Fernandez, N. J. & Combes, F., 2008. Gas flow models in the Milky Way embedded bars. *A&A*, **489**, 115–133.

Rodriguez-Fernandez, N. J., Combes, F., Martin-Pintado, J., Wilson, T. L. & Apponi, A., 2006. Coupling the dynamics and the molecular chemistry in the Galactic center. *A&A*, **455**, 963–969.

Rougoor, G. W. & Oort, J. H., 1959. Neutral hydrogen in the central part of the galactic system. In R. N. Bracewell, ed., *URSI Symp. 1: Paris Symposium on Radio Astronomy*, vol. 9 of *IAU Symposium*, 416.

Sawada, T., Hasegawa, T., Handa, T. & Cohen, R. J., 2004. A molecular face-on view of the Galactic Centre region. *MNRAS*, **349**, 1167–1178.

Schinnerer, E., Maciejewski, W., Scoville, N. & Moustakas, L. A., 2002. Toward the Secondary Bar: Gas Morphology and Dynamics in NGC 4303. *ApJ*, **575**, 826–844.

Schmidt, M., 1959. The Rate of Star Formation. *ApJ*, **129**, 243.

Sellwood, J. A. & Athanassoula, E., 1986. Unstable modes from galaxy simulations. *MNRAS*, **221**, 195–212.

Sellwood, J. A. & Debattista, V. P., 2009. Stochasticity in N-body simulations of disc galaxies. *MNRAS*, **398**, 1279–1297.

Seo, W.-Y. & Kim, W.-T., 2013. Star Formation in Nuclear Rings of Barred Galaxies. *ApJ*, **769**, 100.

Shapley, H., 1918a. Studies based on the colors and magnitudes in stellar clusters. VI. On the

determination of the distances of globular clusters. *ApJ*, **48**.

Shapley, H., 1918b. Studies based on the colors and magnitudes in stellar clusters. VII. The distances, distribution in space, and dimensions of 69 globular clusters. *ApJ*, **48**.

Shapley, H., 1919. Studies based on the colors and magnitudes in stellar clusters. XII. Remarks on the arrangement of the sidereal universe. *ApJ*, **49**.

Shin, J., Kim, S. S., Baba, J., Saitoh, T. R., Hwang, J.-S., Chun, K. & Hozumi, S., 2017. Hydrodynamic Simulations of the Central Molecular Zone with a Realistic Galactic Potential. *ApJ*, **841**, 74.

Sigurdsson, S., Hernquist, L. & Quinlan, G. D., 1995. Models of Galaxies with Central Black Holes: Simulation Methods. *ApJ*, **446**, 75.

Smith, R. J., Glover, S. C. O., Clark, P. C., Klessen, R. S. & Springel, V., 2014. CO-dark gas and molecular filaments in Milky Way-type galaxies. *MNRAS*, **441**, 1628–1645.

Sofue, Y., 1995. Galactic-Center Molecular Arms, Ring, and Expanding Shell. I. Kinematical Structures in Longitude–Velocity Diagrams. *Publications of the Astronomical Society of Japan*, **47**, 527–549.

Sormani, M. C., Binney, J. & Magorrian, J., 2015a. Gas flow in barred potentials. *MNRAS*, **449**, 2421–2435.

Sormani, M. C., Binney, J. & Magorrian, J., 2015b. Gas flow in barred potentials - II. Bar-driven spiral arms. *MNRAS*, **451**, 3437–3452.

Sormani, M. C., Binney, J. & Magorrian, J., 2015c. Gas flow in barred potentials - III. Effects of varying the quadrupole. *MNRAS*, **454**, 1818–1839.

Sormani, M. C. & Magorrian, J., 2015. Recognizing the fingerprints of the Galactic bar: a quantitative approach to comparing model (l, v) distributions to observations. *MNRAS*, **446**, 4186–4204.

Sormani, M. C., Sobacchi, E., Fragkoudi, F., Ridley, M., Tress, R. G., Glover, S. C. O. & Klessen, R. S., 2018a. A dynamical mechanism for the origin of nuclear rings. *MNRAS*, **481**, 2–19.

Sormani, M. C., Sobacchi, E., Shore, S. N., Tress, R. G. & Klessen, R. S., 2017. Periodicity makes galactic shocks unstable - I. Linear analysis. *MNRAS*, **471**, 2932–2951.

Sormani, M. C., Tress, R. G., Ridley, M., Glover, S. C. O., Klessen, R. S., Binney, J., Magorrian, J. & Smith, R., 2018b. A theoretical explanation for the Central Molecular Zone asymmetry. *MNRAS*, **475**, 2383–2402.

Stark, A. A. & Bania, T. M., 1986. Clump 2 - an inner spiral arm? *ApJ*, **306**, L17–L20.

Su, M., Slatyer, T. R. & Finkbeiner, D. P., 2010. Giant Gamma-ray Bubbles from Fermi-LAT: Active Galactic Nucleus Activity or Bipolar Galactic Wind? *ApJ*, **724**, 1044–1082.

Toomre, A., 1964. On the gravitational stability of a disk of stars. *ApJ*, **139**, 1217–1238.

van Albada, G. D., van Leer, B. & Roberts, Jr., W. W., 1982. A comparative study of computational methods in cosmic gas dynamics. *A&A*, **108**, 76–84.

van Albada, T. S. & Sanders, R. H., 1982. Periodic orbits and gas flow in barred spirals. *MNRAS*, **201**, 303–316.

van de Ven, G. & Fathi, K., 2010. Kinematic Analysis of Nuclear Spirals: Feeding the Black Hole in NGC 1097. *ApJ*, **723**, 767–780.

Wada, K., 1994. Gaseous orbits in a weak bar potential: Bar-driven spirals and the effects of

resonances. *Publications of the Astronomical Society of Japan*, **46**, 165–172.

Wada, K. & Koda, J., 2004. Instabilities of spiral shocks - I. Onset of wiggle instability and its mechanism. *MNRAS*, **349**, 270–280.

Walsh, A. J., Breen, S. L., Britton, T., Brooks, K. J., Burton, M. G. et al., 2011. The H_2O Southern Galactic Plane Survey (HOPS) - I. Techniques and H_2O maser data. *MNRAS*, **416**, 1764–1821.

Wegg, C. & Gerhard, O., 2013. Mapping the three-dimensional density of the Galactic bulge with VVV red clump stars. *MNRAS*, **435**, 1874–1887.

Weiland, J. L., Arendt, R. G., Berriman, G. B., Dwek, E., Freudenreich, H. T., Hauser, M. G., Kelsall, T., Lisse, C. M., Mitra, M., Moseley, S. H., Odegard, N. P., Silverberg, R. F., Sodroski, T. J., Spiesman, W. J. & Stemwedel, S. W., 1994. COBE diffuse infrared background experiment observations of the galactic bulge. *ApJ*, **425**, L81–L84.

Weiner, B. J. & Sellwood, J. A., 1999. The Properties of the Galactic Bar Implied by Gas Kinematics in the Inner Milky Way. *ApJ*, **524**, 112–128.

Yurin, D. & Springel, V., 2014. An iterative method for the construction of N-body galaxy models in collisionless equilibrium. *MNRAS*, **444**, 62–79.